INVESTIGATION OF STIFFNESS AS A BIOMARKER IN OVARIAN CANCER CELLS

A Dissertation
Presented to
The Academic Faculty

By

Wenwei Xu

In Partial Fulfillment
Of the Requirements for the Degree
Doctor of Philosophy in the
George W. Woodruff School of Mechanical Engineering

Georgia Institute of Technology

December 2013

INVESTIGATION OF STIFFNESS AS A BIOMARKER IN OVARIAN CANCER CELLS

Approved by:

Dr. Todd Sulchek
George W. Woodruff School of
Mechanical Engineering
Georgia Institute of Technology

Dr. Alexander Alexeev
George W. Woodruff School of
Mechanical Engineering
Georgia Institute of Technology

Dr. Cheng Zhu
Wallace H. Coutler Department of
Biomedical Engineering
Georgia Institute of Technology

Dr. Wilbur Lam
Wallace H. Coulter Department of
Biomedical Engineering
*Georgia Institute of Technology and
Emory University*

Dr. John McDonald
School of Biology
Georgia Institute of Technology

Date Approved: November 13,2013

ACKNOWLEDGEMENTS

I would like to express my deepest appreciation to my advisor, Dr. Todd Sulchek, who has continuously guided me through the time at Georgia Tech, and provided me with an excellent atmosphere for research and study. What I learned from him not only inspires me academically in graduate school but also helps me for my career in the future. I am also grateful to other committee members, Dr. Alexander Alexeev, Dr. Cheng Zhu, Dr. Wilbur Lam, and Dr. John McDonald, for providing me with valuable advice and suggestions on my research, without which the completion of the dissertation is impossible.

I would like to thank Dr. Roman Mezencev and Dr. Lijuan Wang, they not only collaborated with me on research, but also helped me on subjects I am not familiar with, they are always kind and helpful when I got questions. Joseph BK Kim was an undergraduate student worked with me on cell mechanics, his contribution to this research is also highly appreciated.

Vince Fiore and Dr. Julia Henkels are two fellow students who also helped me a lot in my research, their taught me on various techniques, which would difficult to obtain in short time without their kind help and patience.

Our lab is a warm place characterized by friendly lab mates and atmosphere, Kipp Schoenwald, Billy Wang, Daniel Potter, Patricia Pacheco, Tom Bongiorno, Ahmad M Haider, Bushra Tasadduq. These lab mates and friends are making my life easier and the lab a more enjoyable place.

Finally, I want to thank my family for unconditional support and believing in me.

TABLE OF CONTENTS

LIST OF TABLES

LIST OF FIGURES

LIST OF SYMBOLS AND ABBREVIATIONS

˚C   Degree Celsius

µL   Micro liter

mL   Milliliter

BSA   Bovine serum albumin

DAPI   4',6-Diamidino-2-Phenylindole

FITC   Fluorescein isothiocyanate

TRITC   Tetramethylrhodamine isothiocyanate

FBS   Fetal bovine serum

PBS   Phosphate buffered saline

FACS   Fluorescence activated cell sorting

M   Molar

PCR   Polymerase chain reaction

UV   Ultraviolet

Vis   Visible wavelengths

FUCCI   Fluorescence ubiquitination cell cycle indicator

CDK   Cyclin-dependent kinase

GTP   Guanosine triphosphate

TGF   Transforming growth factor

SUMMARY

In this dissertation, we developed cell stiffness as a biomarker in ovarian cancer for the purpose of grading metastatic potential. By measuring single cell stiffness with atomic force microscopy and quantifying *in vitro* invasiveness of healthy and cancerous ovarian cells, we demonstrated that cancerous ovarian cells have reduced stiffness compared to the healthy ones and invasive ovarian cancer cells are more deformable than noninvasive ovarian cancer cells. The difference in cell stiffness between two genetically similar cell lines was attributed to actin-mediated cytoskeletal remodeling as revealed by comparative gene expression profile analysis, and was further confirmed by fluorescent visualization of actin cytoskeletal structures. The actin cytoskeletons were innovatively quantified and correlates with cell stiffness distributions, further implicating actin-mediated cytoskeletal remodeling in stiffness alteration from the perspective of structure-property relationship. The correlation between stiffness and metastatic potential was also demonstrated in pancreatic cancer cell line AsPC-1, which shows reduced invasivess and increased stiffness upon treatment with N-acetyl-L-cysteine (NAC), a well known antioxidant, reactive oxygen species (ROS), scavenger and glutathione precursor. The correlation between cell stiffness and metastatic potential as demonstrated in ovarian and pancreatic cancer cells indicated that mechanical stiffness may be a useful biomarker to evaluate the relative metastatic potential of ovarian and perhaps other types of cancer cells, and might be useful clinically with the development of rapid biomechanical assaying techniques.

We have also investigated the stiffness evolution through progression of the cell cycle for the healthy ovarian phenotype and the invasive cancer ovarian phenotype, and found that

the healthy phenotype at G1 phase are significantly stiffer than other single cells except the invasive phenotype at late mitosis; other groups are not significantly different from each other.

We have also investigated intracellular heterogeneity and mechanical nonlinearity in single cells. To this end, we developed a methodology to analyze the deformation-dependent mechanical nonlinearity using a pointwise Hertzian method, and tested the method on ultrathin polydimethylsiloxane (PDMS) films which underwent extremely large strains (greater than 50%). Mechanical stiffening due to large strain and geometrical confinement were observed. The onset of nonlinearity or mechanical stiffening occurs at 45% of the film thickness, the geometry induced stiffening causes an increase in stiffness which shows a strong power law dependence on film thickness. By applying the pointwise Hertzian method on stiffness measurements with AFM that were collected on living cells, we also investigated the nonlinear and heterogeneous mechanics of single cells, since attachment of cells to stiff substrate during indentation may impact their mechanical responses. Even under natural biological conditions, cells confined in narrow spaces may experience heightened mechanical stiffness. Through indentation-dependent force mapping, analysis of the local cell stiffness demonstrated spatial variation. The results indicated that the mechanical properties of single cells are highly nonlinear and are dependent upon the subcellular features under the applied force as well as the dimensions of the cellular material.

We identified single cell stiffness as a potential biomarker of the metastatic potential in ovarian cancer, and quantified the effect of geometrical confinement on cell mechanics. The results presented in this dissertation not only made contributions to the development

of accurate, non-invasive clinical methods to estimate metastatic potential of ovarian and perhaps other types of cancer, but also shed light on the intracellular mechanical information by developing new techniques to quantify the effect of geometry on cell mechanics.

CHAPTER 1

INTRODUCTION

1.1　Abstract

Cell mechanics is an interdisciplinary subject studying the interplay of mechanical forces with cellular functions. The mechanical properties of cells and their relevance to cellular function have been investigated using a variety of techniques. In our study of cell mechanics, we focus on the correlation between malignancy and the mechanical properties of single cells. Efforts by other researchers have investigated the mechanics in many aspects of cancer, including the process of tumorigenesis and cancer progression. The goal in of this research is to investigate the correlation between cell stiffness and the metastatic potential, including understanding of the biological underpinnings of mechanical changes, in order to potentially utilize the mechanical properties of cells as a biomarker for diagnosis and grading the metastatic potentials of ovarian cancer.

This chapter summarizes the relevant knowledge of cell mechanics as it pertains to cancer; including the relationship between mechanics and cell biology and pathology, theories of contact mechanics, common techniques for measuring cell mechanics, and a discussion of the motivation of the research project.

1.2　Overview of cell mechanics

1.2.1　Intracellular structures mediate many functions as well as the mechanical properties of cells

Living cells, as the basic unit of life, are dynamic biological systems capable of modulating their structure and properties in response to environment and intra- and extracellular signals. Cellular structures play a pivotal role in many processes, such as

1

adhesion, locomotion, mitosis, and mechanotransduction. For example, cell adhesion to and move on the substrate requires the formation of actin in lamellipodia and myosin activity [1-4]. Invasive tumor cells improve their capacity to escape from the primary tumor [5-11] through modification of their cytoskeletal structures and associated adhesion sites. Moreover, alterations in gene expression patterns within the cell [12-14] through signal transduction pathways are activated by mechanical interactions which requires the involvement of coordination between different cytoplasmic components. Understanding how cellular structures and their appropriate interactions mediate cellular functions requires the understanding of the mechanical properties of these cellular structures.

The mechanical integrity of cells is regulated by a dynamic network of structural, cross-linking, and signaling molecules [15]. Among the various cellular components, both the cytoskeleton and nucleus play crucial roles in a variety of cellular functions affecting biomechanics [14, 16, 17]. These two structures also are primary contributors to the mechanical properties of individual cells [18, 19]. Mechanical measurements of single cells can reveal important information about these dynamic structures, and alterations of these networks change both mechanical properties and functionalities of cells.

1.2.2   Diseases are related to abnormalities in cell stiffness through cytoskeleton
Many diseases are associated with abnormalities in cell stiffness. Studies of a variety of diseases utilizing different experimental techniques have shown that abnormalities in the elastic properties of cells are associated with disease pathogenesis and progression [5, 20-33]. Human red blood cells become stiffer in the case of infection of the parasites of malaria [5, 34, 35]. Nuclear abnormalities are observed in the case of laminopathy, in

which alerted nuclear structure and stiffness [14, 36, 37] resulting in increased deformability.

Cellular dysfunction is usually accompanied by alterations in cellular structures, which subsequently introduces abnormalities in mechanical properties of cells. Actin cytoskeleton is a determinant factor in single cell stiffness [24, 38, 39] and signal transduction, and therefore abnormalities in actin cytoskeleton upon disease result in changes in mechanical properties. In the case of cancer, when cells transform from healthy states to cancerous states, the cytoskeletal structure change from an organized state to an irregular state, and this change subsequently reduces the stiffness of single cells [22, 40-42]. Modification of cytoskeletal structure and relevant protein activities through chemical methods also changes the mechanical properties of single cells [25, 43-47].

Cell mechanics studies on different types of cancer have shown that single cell elasticity is altered upon malignance [23, 27, 48-55], as well as for primary cells for some types of cancer [56, 57]. Abnormal single cell elasticity resulting from cancer points to a potential new biomarker to detect cancer [20, 23, 57]. Metastasis is the primary factor leading to death of cancer patients and it is important to identify metastatic cancer during diagnosis for proper treatment. In general, metastasis is a multi-step process in which malignant cancer cells from the primary tumor develop into secondary tumor. Actin cytoskeleton is known to play a vital role in metastasis by formation of protrusive structure [2, 58-60] interacting with the extracellular matrix (ECM) [61-64] during migration and invasion [8, 65-67]. Stiffness and cancer metastasis as two properties dictated by cytoskeleton are therefore related. There are some reports suggesting the cancer cells that are more

migratory are also higher in deformability [56, 68], further implies the role of cytoskeleton in cancer malignancy and progression.

1.2.3   Gene expression and cancer cell mechanics

Cellular structure and mechanics are ultimately regulated by the underlying gene expression profile. The abnormalities in cellular mechanical properties can therefore be examined at the molecular level in which the gene expression pattern goes awry. When cancer develops, genetic mutations and gene expression alterations drive cells to undergo a neoplastic transformation as well as altered cellular interactions with other cells and with the ECM. The profiling of gene expression for a variety of common cancers [69-80] displayed distinctive patterns for different cancer stages, indicating a genetic signature of malignancy and metastasis [73, 81-85]. This knowledge opens up a promising search for diagnosis biomarkers and therapeutic targets [86-88]. Despite extensive studies on gene expression profile in cancer [89-93], little effort has been made to resolve the role of gene expression in the mechanics of single cells. Since mechanics figures prominently in cancer pathogenesis, a study which definitively identifies the impact of genes on cell mechanics is needed.

1.2.4   Need of new biomarkers in metastatic ovarian cancer

Current diagnosis of cancer mainly relies on the measurement of biomarker levels in patient's serum or morphology examination of normal and tumor cell types within biopsies. However, these techniques are not easily used in diagnosis of ovarian carcinoma at an early stage. The need for effective biomarkers for diseases is particularly important in the case of ovarian cancer, which was ranked fifth among leading causes of cancer-related deaths of U.S. women in 2007 and its 5 year survival rate was 46% for all cases

4

diagnosed within 1999-2005[94]. Due to the unavailability of reliable screening in clinical practice and the asymptomatic course through early stages of the disease, the majority of ovarian cancer cases (68%) are diagnosed as metastatic disease with poor survival [95]. To enable early detection of ovarian cancer, a creative method is needed.

Cancer antigen CA-125 is the most frequently used biomarker of ovarian cancer. Measurement of this protein level in blood stream is used as an indicator of ovarian cancer, however, CA-125 as an ovarian cancer biomarker is not reliable, sensitive [96-98] or specific [99, 100]. Morphological assessment is also used to identify tumors using exfoliated, aspirated or surgically removed tissue samples[101]. However, the morphological overlap between the benign and tumor phenotypes makes cancer diagnosis difficult and cytomorphogical analysis alone has only about a 50-70% accuracy for diagnosing cancer in body fluid sample [101-103].

1.2.5 *Methods in cell mechanics*

Several different techniques have been used to study cellular mechanics, including micropipette aspiration [104-106], magnetic twisting cytometry [107], optical tweezers [108, 109], shear flow [110], substrate stretching [4, 111] and atomic force microscopy [48, 101, 112], to name a few. Measurements are conducted either at single cells level or on cell populations. Figure 1.1 summarizes some common methods in cell mechanics.
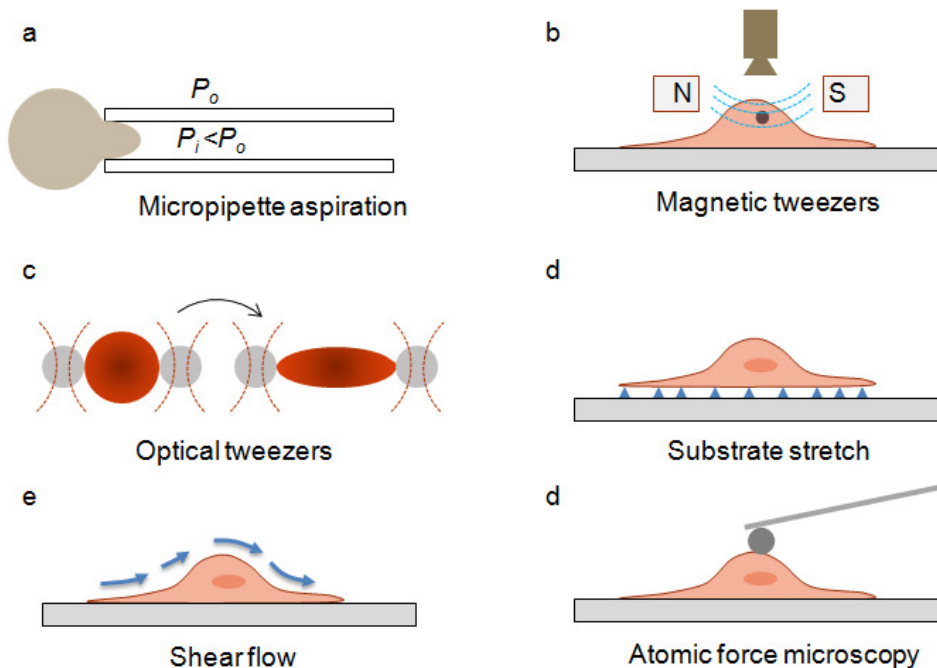
Figure 1.1: Common techniques in cell mechanics measurement, a) micropipette aspiration, b) magnetic tweezers, c) optical tweezers, d) substrate stretch, cells adhered to soft substrate through adhesion complexes, e) shear flow, and f) atomic force microscopy.

Among the methods summarized above, atomic force microscopy (AFM) uses a sensitive cantilever to probe forces down to the picoNewton scale, which makes it an appropriate tool to in the study of cellular biomechanics. The central component of AFM is the flexible cantilever spring, which bends proportionally to the force applied to its free end, and as such can record the force and compressions simultaneously. From these measurements, a variety of information about samples is extracted. In cell biology, AFM has been used widely to study cell and tissue mechanics [101, 112-120]. In single cell mechanics measurements, the AFM compresses the single cell resting on a hard or soft substrate and the force response of the cell is recorded. From the measurement of the force required for cell indentation, the material properties can be obtained. Figure 1.2

sketches the principle components and typical experimental setup of AFM in single cell

mechanics measurements.
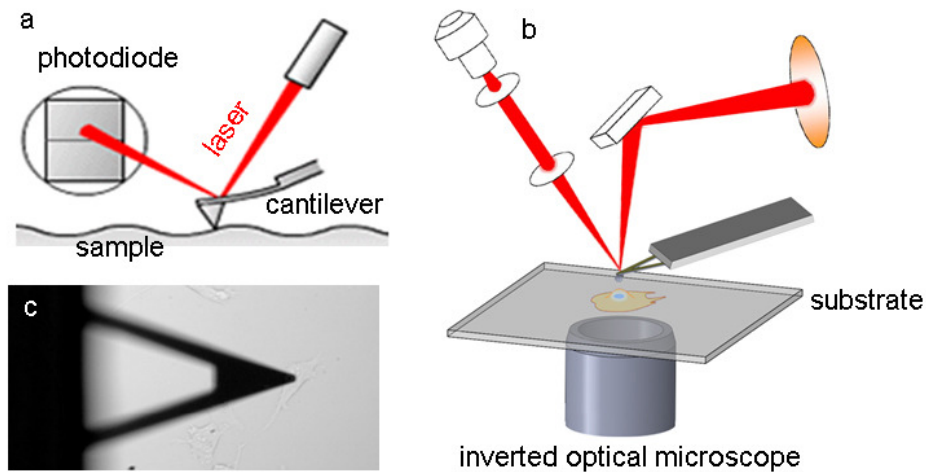
Figure 1.2: Applications of AFM in single cell mechanics measurements, a) principles of AFM, the sample information is translated into the output of photodiode, b) a typical experimental setup in cell mechanics measurements with AFM, and c) optical image of AFM cantilever indenting on a single cell (top view), the width of the cantilever leg is about 20 µm.

In our experiments, AFM will be used to compress soft cells immobilized on glass

substrates. The displacement of the cantilever and indentation of the cell will be recorded

and the Young's modulus will be determined by fitting the experimental force-

indentation curve with the appropriate contact model. A Hertzian contact model is

frequently used to quantitatively extract the stiffness information in the study of single

cells involving AFM [119, 121]. It was first developed to describe the contact between

two deformable spheres and later adopted for other contact geometries. The sketch of the

Hertz model is displayed in Figure 1.3.

7
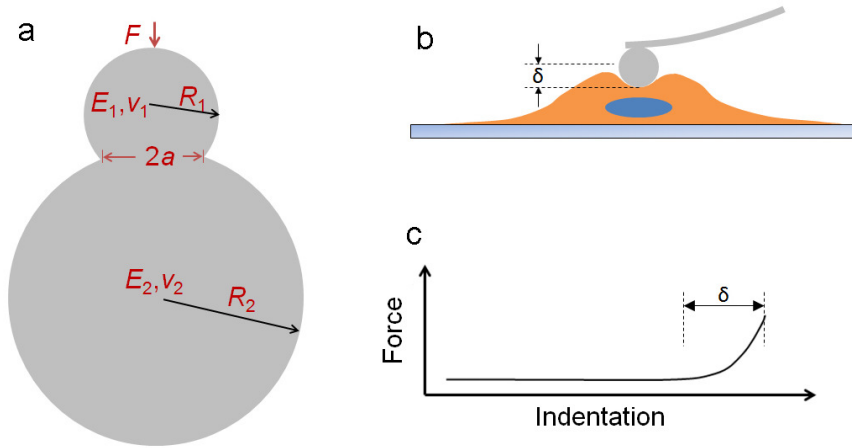
Figure 1.3: Sketch of Hertz model in cell mechanics, a) Hertz model describes the contact behavior of two deformable spheres, b) AFM indentation on single cell, and c) force-indentation curve generated in AFM indentation

The mathematical formulas of Hertz model for two deformable spheres are of the form described in Equation 1.1 and 1.2.

$$a^3 = \frac{3PR}{4E^*} \qquad \text{(Eqn.1.1)}$$

$$\delta = \left(\frac{9P^2}{16RE^{*2}}\right)^{1/3} \qquad \text{(Eqn.1.2)}$$

Where a is the radius of the contact region between the indenter and the sample, δ is the indentation into the material, P is the loading force, and R is the effective radius of curvature defined as $1/R = 1/R_1 + 1/R_2$, E^* is the apparent Young's modulus defined as $\frac{1}{E^*} = \frac{1-v_1^2}{E_1} + \frac{1-v_2^2}{E_2}$, where v_1 and v_2 are the Poisson's ratio for the material and the subscripts denote the two contacting bodies.

The Hertz model is widely used in interpret the result of stiffness measurement with AFM on single cells, however cells are highly complex and heterogeneous in structure

and material properties [122-126], and a systematic approach will be needed to incorporate mechanical nonlinearity and heterogeneity in our cell mechanics studies.

1.3   Motivations and significance of the research project

With this research project, we seek to:

1. Test the hypothesis that cell stiffness and metastatic potential are correlated in ovarian cancer and to show that stiffness can be used as a biomarker to grade metastatic potential in ovarian cancer and perhaps other types of cancer;

2. Resolve the effects of nonlinearity and heterogeneity in stiffness measurement on single ovarian cells with AFM, and to quantify the modulus distribution throughout the cellular region.

3. Identify the molecular factors that influence cell stiffness, including variations in cell mechanics as a result of the cellular growth cycle.

1.4   Thesis overview

This dissertation focuses on single cell mechanics of ovarian cancer, and the development of new methods to investigate heterogeneity and nonlinearity in single cell mechanics measurement with AFM.

In the first half of the thesis, single cell mechanics of healthy and cancerous ovarian cells will be investigated and correlated with metastatic potential, the difference in mechanics and metastatic potential is the caused by abnormalities in gene expression profile. Cell stiffness can potentially be used as an effective biomarker of metastatic potential in ovarian cancer and probably be extendable to other types of cancer. Stiffness distribution also shows a dependence on cell cycle in healthy phenotype, which may be due to the

cytoskeletal organization. In the second half of the thesis, the effects of nonlinearity and heterogeneity in stiffness measurement were addressed. A method calculating indentation-dependent Young's modulus was tested on a geometrically confined polymer thin film and a significant strain-dependent stiffening was observed. The method is then combined with a force mapping technique to investigate the nonlinearity and heterogeneity in single cell mechanics, with the results showing consistence with the structural heterogeneity of the single cells.

Chapter 1 - This chapter summarizes the cell mechanics, including background and methods being used, and state the motivation of the research.

Chapter 2 - This chapter focused on the investigation of single cell mechanics of ovarian cancer, developed stiffness as a new biomarker to grade metastatic potential, and found that the cytoskeletal remodeling caused by differential gene expression profile is the molecular factor contributing to alteration in stiffness.

Chapter 3 - This chapter presents the detailed investigation of single cell stiffness through the cell cycle, and found that cell cycle dependence of stiffness in the healthy cell type.

Chapter 4 - This chapter addresses the effects of nonlinearity on stiffness measurements with AFM, investigated a geometrically confined polymer thin film and found significant stiffening by determining the indentation-dependent Young's modulus.

Chapter 5 - This chapter combines the method used in chapter 4 and force mapping to describe the heterogeneity of single cells, which is usually ignored in cell stiffness measurements, with the resultant mechanical heterogeneity showing consistence with the structural heterogeneity.

Chapter 6 - This chapter summarizes the research and describes the future development

and extension of research presented here.

1.5   References

1.   Giannone, G., et al., *Lamellipodial Actin Mechanically Links Myosin Activity with Adhesion-Site Formation.* Cell, 2007. **128**(3): p. 561-575.

2.   Mitchison, T.J. and L.P. Cramer, *Actin Based Cell Motility and Cell Locomotion.* Cell, 1996. **84**(3): p. 371-379.

3.   Stossel, T., *On the crawling of animal cells.* Science, 1993. **260**(5111): p. 1086-1094.

4.   Dembo, M. and Y.-L. Wang, *Stresses at the Cell-to-Substrate Interface during Locomotion of Fibroblasts.* Biophysical Journal, 1999. **76**: p. 2307-2316.

5.   Suresh, S., et al., *Connections between single-cell biomechanics and human disease states: gastrointestinal cancer and malaria.* Acta Biomaterialia, 2005. **1**(1): p. 15-30.

6.   Yilmaz, M. and G. Christofori, *EMT, the cytoskeleton, and cancer cell invasion.* Cancer and Metastasis Reviews, 2009. **28**(1-2): p. 15-33.

7.   Kumar, S. and V. Weaver, *Mechanics, malignancy, and metastasis: The force journey of a tumor cell.* Cancer and Metastasis Reviews, 2009. **28**(1): p. 113-127.

8.   Kedrin, D., et al., *Cell Motility and Cytoskeletal Regulation in Invasion and Metastasis.* Journal of Mammary Gland Biology and Neoplasia, 2007. **12**(2): p. 143-152.

9.   Thiery, J.P., et al., *Epithelial-Mesenchymal Transitions in Development and Disease.* Cell, 2009. **139**(5): p. 871-890.

10.   Guarino, M., *Epithelial–mesenchymal transition and tumour invasion.* The International Journal of Biochemistry & Cell Biology, 2007. **39**(12): p. 2153-2160.

11. Vergara, D., et al., *Epithelial–mesenchymal transition in ovarian cancer.* Cancer Letters, 2010. **291**(1): p. 59-66.

12. Lehoux, S. and A. Tedgui, *Cellular mechanics and gene expression in blood vessels.* Journal of biomechanics, 2003. **36**(5): p. 631-643.

13. Zhang, F., et al., *Compressive force stimulates the gene expression of IL-17s and their receptors in MC3T3-E1 cells.* Connective Tissue Research, 2010. **51**(5): p. 359-369.

14. Dahl, K.N., A.J.S. Ribeiro, and J. Lammerding, *Nuclear Shape, Mechanics, and Mechanotransduction.* Circulation Research, 2008. **102**(11): p. 1307-1318.

15. Fletcher, D.A. and R.D. Mullins, *Cell mechanics and the cytoskeleton.* Nature, 2010. **463**(7280): p. 485-492.

16. Shimi, T., et al., *The role of nuclear lamin B1 in cell proliferation and senescence.* Genes & Development, 2011. **25**(24): p. 2579-2593.

17. Cremer, T., et al., *Higher order chromatin architecture in the cell nucleus: on the way from structure to function.* Biol. Cell, 2004. **96**(8): p. 555-567.

18. Lombardi, M.L. and J. Lammerding, *Chapter 6 - Altered Mechanical Properties of the Nucleus in Disease*, in *Methods in Cell Biology*, G.V. Shivashankar, Editor. 2010, Academic Press. p. 121-141.

19. Caille, N., et al., *Contribution of the nucleus to the mechanical properties of endothelial cells.* Journal of biomechanics, 2002. **35**(2): p. 177-187.

20. Cross, S.E., et al., *Nanomechanical analysis of cells from cancer patients.* Nat Nano, 2007. **2**(12): p. 780-783.

21. Yamazaki, D., S. Kurisu, and T. Takenawa, *Regulation of cancer cell motility through actin reorganization.* Cancer Science, 2005. **96**(7): p. 379-386.

22. Guck, J., et al., *Optical Deformability as an Inherent Cell Marker for Testing Malignant Transformation and Metastatic Competence.* Biophysical Journal, 2005. **88**(5): p. 3689-3698.

23.   Suresh, S., *Nanomedicine: Elastic clues in cancer detection.* Nat Nano, 2007. **2**(12): p. 748-749.

24.   Suresh, S., *Biomechanics and biophysics of cancer cells.* Acta Materialia, 2007. **55**(12): p. 3989-4014.

25.   Rotsch, C. and M. Radmacher, *Drug-Induced Changes of Cytoskeletal Structure and Mechanics in Fibroblasts: An Atomic Force Microscopy Study.* Biophysical Journal, 2000. **78**(1): p. 520-535.

26.   Elson, E.L., *Cellular Mechanics as an Indicator of Cytoskeletal Structure and Function.* Annual Review of Biophysics and Biophysical Chemistry, 1988. **17**(1): p. 397-430.

27.   Lekka, M., et al., *Elasticity of normal and cancerous human bladder cells studied by scanning force microscopy.* European Biophysics Journal, 1999. **28**(4): p. 312-316.

28.   Rao, J.Y. and N. Li, *Microfilament Actin Remodeling as a Potential Target for Cancer Drug Development.* Current Cancer Drug Targets, 2004. **4**(4): p. 345-354.

29.   Worthen, G., et al., *Mechanics of stimulated neutrophils: cell stiffening induces retention in capillaries.* Science, 1989. **245**(4914): p. 183-186.

30.   Bosch, F.H., et al., *Determinants of red blood cell deformability in relation to cell age.* European Journal of Haematology, 1994. **52**(1): p. 35-41.

31.   Williamson, J., et al., *Microrheologic investigation of erythrocyte deformability in diabetes mellitus.* Blood, 1985. **65**(2): p. 283-288.

32.   Lekka, M. and P. Laidler, *Applicability of AFM in cancer detection.* Nat Nano, 2009. **4**(2): p. 72-72.

33.   Lee, G.Y.H. and C.T. Lim, *Biomechanics approaches to studying human diseases.* Trends in Biotechnology, 2007. **25**(3): p. 111-118.

34.   Cooke, B.M., N. Mohandas, and R.L. Coppel, *The malaria-infected red blood cell: Structural and functional changes*, in *Advances in Parasitology*. 2001, Academic Press. p. 1-86.

35.   Suresh, S., *Mechanical resposne of human red blood cells in health and disease some struture property function relationships.* Journal of Materials Research, 2011. **21**(8): p. 1871-1877.

36.   Broers, J.L.V., et al., *Nuclear Lamins: Laminopathies and Their Role in Premature Ageing.* Physiological Reviews, 2006. **86**(3): p. 967-1008.

37.   Burke, B. and C.L. Stewart, *The Laminopathies: The Functional Architecture of the Nucleus and Its Contribution to Disease*.* Annual Review of Genomics and Human Genetics, 2006. **7**(1): p. 369-405.

38.   O'Callaghan, R., et al., *Stiffness and heterogeneity of the pulmonary endothelial glycocalyx measured by atomic force microscopy.* American Journal of Physiology - Lung Cellular and Molecular Physiology, 2011. **301**(3): p. L353-L360.

39.   Pourati, J., et al., *Is cytoskeletal tension a major determinant of cell deformability in adherent endothelial cells?* American Journal of Physiology - Cell Physiology, 1998. **274**(5): p. C1283-C1289.

40.   Moustakas, A. and C. Stournaras, *Regulation of actin organisation by TGF-beta in H-ras-transformed fibroblasts.* Journal of Cell Science, 1999. **112**(8): p. 1169-1179.

41.   Katsantonis, J., et al., *Differences in the G/total actin ratio and microfilament stability between normal and malignant human keratinocytes.* Cell Biochemistry and Function, 1994. **12**(4): p. 267-274.

42.   Friedman, E., et al., *Actin Cytoskeletal Organization Loss in the Benign-to-Malignant Tumor Transition in Cultured Human Colonic Epithelial Cells.* Cancer Research, 1984. **44**(7): p. 3040-3050.

43.   Lekka, M., et al., *The effect of chitosan on stiffness and glycolytic activity of human bladder cells.* Biochimica et Biophysica Acta (BBA) - Molecular Cell Research, 2001. **1540**(2): p. 127-136.

44.   Wakatsuki, T., et al., *Effects of cytochalasin D and latrunculin B on mechanical properties of cells.* Journal of Cell Science, 2001. **114**(5): p. 1025-1036.

45.   Pelling, A.E., et al., *Distinct contributions of microtubule subtypes to cell membrane shape and stability.* Nanomedicine: Nanotechnology, Biology and Medicine, 2007. **3**(1): p. 43-52.

46.   Pogoda, K., et al., *Depth-sensing analysis of cytoskeleton organization based on AFM data.* European Biophysics Journal, 2012. **41**(1): p. 79-87.

47.   Cai, X., et al., *Connection between biomechanics and cytoskeleton structure of lymphocyte and Jurkat cells: An AFM study.* Micron, 2010. **41**(3): p. 257-262.

48.   Fuhrmann, A., et al., *AFM stiffness nanotomography of normal, metaplastic and dysplastic human esophageal cells.* Physical Biology, 2011. **8**(1): p. 015007.

49.   Yu, Z., et al. *Normal and cancer breast epithelial cells endocytosis study of nanoparticles by combined AFM and NSOM microscopy.* in *Nanotechnology, 2007. IEEE-NANO 2007. 7th IEEE Conference on.* 2007.

50.   Lekka, M., et al., *Cancer cell detection in tissue sections using AFM.* Archives of Biochemistry and Biophysics, 2012. **518**(2): p. 151-156.

51.   Reich, A., et al., *Surface morphology and mechanical properties of fibroblasts from scleroderma patients.* Journal of Cellular and Molecular Medicine, 2009. **13**(8b): p. 1644-1652.

52.   Faria, E.C., et al., *Measurement of elastic properties of prostate cancer cells using AFM.* Analyst, 2008. **133**(11): p. 1498-1500.

53.   Prabhune, M., et al., *Comparison of mechanical properties of normal and malignant thyroid cells.* Micron, 2012. **43**(12): p. 1267-1272.

54.   Plodinec, M., et al., *The nanomechanical signature of breast cancer.* Nat Nano, 2012. **7**(11): p. 757-765.

55.   Di Carlo, D., *A Mechanical Biomarker of Cell State in Medicine.* Journal of Laboratory Automation, 2012. **17**(1): p. 32-42.

56. Swaminathan, V., et al., *Mechanical Stiffness Grades Metastatic Potential in Patient Tumor Cells and in Cancer Cell Lines.* Cancer Research, 2011. **71**(15): p. 5075-5080.

57. Remmerbach, T.W., et al., *Oral Cancer Diagnosis by Mechanical Phenotyping.* Cancer Research, 2009. **69**(5): p. 1728-1732.

58. Ridley, A.J., et al., *Cell Migration: Integrating Signals from Front to Back.* Science, 2003. **302**(5651): p. 1704-1709.

59. Mogilner, A. and G. Oster, *Cell motility driven by actin polymerization.* Biophysical Journal, 1996. **71**(6): p. 3030-3045.

60. Yamaguchi, H. and J. Condeelis, *Regulation of the actin cytoskeleton in cancer cell migration and invasion.* Biochimica et Biophysica Acta (BBA) - Molecular Cell Research, 2007. **1773**(5): p. 642-652.

61. Burridge, K., et al., *Focal Adhesions: Transmembrane Junctions Between the Extracellular Matrix and the Cytoskeleton.* Annual Review of Cell Biology, 1988. **4**(1): p. 487-525.

62. Buccione, R., J.D. Orth, and M.A. McNiven, *Foot and mouth: podosomes, invadopodia and circular dorsal ruffles.* Nat Rev Mol Cell Biol, 2004. **5**(8): p. 647-657.

63. Weaver, A., *Invadopodia: Specialized Cell Structures for Cancer Invasion.* Clinical and Experimental Metastasis, 2006. **23**(2): p. 97-105.

64. Aznavoorian, S., et al., *Molecular aspects of tumor cell invasion and metastasis.* Cancer, 1993. **71**(4): p. 1368-1383.

65. Chambers, A.F., A.C. Groom, and I.C. MacDonald, *Metastasis: Dissemination and growth of cancer cells in metastatic sites.* Nat Rev Cancer, 2002. **2**(8): p. 563-572.

66. Geho, D.H., et al., *Physiological Mechanisms of Tumor-Cell Invasion and Migration.* Physiology, 2005. **20**(3): p. 194-200.

67.   Vignjevic, D. and G. Montagnac, *Reorganisation of the dendritic actin network during cancer cell migration and invasion.* Seminars in Cancer Biology, 2008. **18**(1): p. 12-22.

68.   Ochalek, T., et al., *Correlation between Cell Deformability and Metastatic Potential in B16-F1 Melanoma Cell Variants.* Cancer Research, 1988. **48**(18): p. 5124-5128.

69.   Sørlie, T., et al., *Gene expression patterns of breast carcinomas distinguish tumor subclasses with clinical implications.* Proceedings of the National Academy of Sciences, 2001. **98**(19): p. 10869-10874.

70.   Chen, X., et al., *Gene Expression Patterns in Human Liver Cancers.* Molecular Biology of the Cell, 2002. **13**(6): p. 1929-1939.

71.   Singh, D., et al., *Gene expression correlates of clinical prostate cancer behavior.* Cancer Cell, 2002. **1**(2): p. 203-209.

72.   Onken, M.D., et al., *Gene Expression Profiling in Uveal Melanoma Reveals Two Molecular Classes and Predicts Metastatic Death.* Cancer Research, 2004. **64**(20): p. 7205-7209.

73.   Lee, Y.-F., et al., *A Gene Expression Signature Associated with Metastatic Outcome in Human Leiomyosarcomas.* Cancer Research, 2004. **64**(20): p. 7201-7204.

74.   Nannini, M., et al., *Gene expression profiling in colorectal cancer using microarray technologies: Results and perspectives.* Cancer Treatment Reviews, 2009. **35**(3): p. 201-209.

75.   Oue, N., et al., *Genes Involved in Invasion and Metastasis of Gastric Cancer Identified by Array-Based Hybridization and Serial Analysis of Gene Expression.* Oncology, 2005. **69**(Suppl. 1): p. 17-22.

76.   Garnis, C., T.P. Buys, and W.L. Lam, *Genetic alteration and gene expression modulation during cancer progression.* Molecular Cancer, 2004. **3**: p. 9.

77.   Khan, J., et al., *Gene Expression Profiling of Alveolar Rhabdomyosarcoma with cDNA Microarrays.* Cancer Research, 1998. **58**(22): p. 5009-5013.

78.   Lapointe, J., et al., *Gene expression profiling identifies clinically relevant subtypes of prostate cancer.* Proceedings of the National Academy of Sciences of the United States of America, 2004. **101**(3): p. 811-816.

79.   Creekmore, A.L., et al., *Changes in Gene Expression and Cellular Architecture in an Ovarian Cancer Progression Model.* PLoS ONE, 2011. **6**(3): p. e17676.

80.   Cardoso, J., et al., *Expression and genomic profiling of colorectal cancer.* Biochimica et Biophysica Acta (BBA) - Reviews on Cancer, 2007. **1775**(1): p. 103-137.

81.   Cui, J., et al., *Gene-Expression Signatures Can Distinguish Gastric Cancer Grades and Stages.* PLoS ONE, 2011. **6**(3): p. e17819.

82.   van de Vijver, M.J., et al., *A Gene-Expression Signature as a Predictor of Survival in Breast Cancer.* New England Journal of Medicine, 2002. **347**(25): p. 1999-2009.

83.   Ramaswamy, S., et al., *Multiclass cancer diagnosis using tumor gene expression signatures.* Proceedings of the National Academy of Sciences, 2001. **98**(26): p. 15149-15154.

84.   Su, A.I., et al., *Molecular Classification of Human Carcinomas by Use of Gene Expression Signatures.* Cancer Research, 2001. **61**(20): p. 7388-7393.

85.   Khanna, C., et al., *Metastasis-associated Differences in Gene Expression in a Murine Model of Osteosarcoma.* Cancer Research, 2001. **61**(9): p. 3750-3759.

86.   Yamabuki, T., et al., *Genome-wide gene expression profile analysis of esophageal squamous cell carcinomas.* International Journal of Oncology, 2006. **28**(6): p. 1375-1384.

87.   Bertucci, F., et al., *Gene expression profiling of primary breast carcinomas using arrays of candidate genes.* Human Molecular Genetics, 2000. **9**(20): p. 2981-2991.

88.   Martin, K.J., et al., *Linking Gene Expression Patterns to Therapeutic Groups in Breast Cancer.* Cancer Research, 2000. **60**(8): p. 2232-2238.

89.   Chien, S., S. Li, and J.Y.-J. Shyy, *Effects of mechanical forces on signal transduction and gene expression in endothelial cells.* Hypertension, 1998. **31**: p. 162-169.

90.   Darling, E., et al., *Mechanical Properties and Gene Expression of Chondrocytes on Micropatterned Substrates Following Dedifferentiation in Monolayer.* Cellular and Molecular Bioengineering, 2009. **2**(3): p. 395-404.

91.   Hunter, C.J., et al., *Mechanical compression alters gene expression and extracellular matrix synthesis by chondrocytes cultured in collagen I gels.* Biomaterials, 2002. **23**(4): p. 1249-1259.

92.   Avvisato, C.L., et al., *Mechanical force modulates global gene expression and β-catenin signaling in colon cancer cells.* Journal of Cell Science, 2007. **120**(15): p. 2672-2682.

93.   Brooks, A.R., P.I. Lelkes, and G.M. Rubanyi, *Gene Expression Profiling of Vascular Endothelial Cells Exposed to Fluid Mechanical Forces: Relevance for Focal Susceptibility to Atherosclerosis.* Endothelium, 2004. **11**(1): p. 45-57.

94.   Jemal, A., et al., *Cancer Statistics, 2010.* CA: A Cancer Journal for Clinicians, 2010. **60**(5): p. 277-300.

95.   Bhoola, S. and W.J. Hoskins, *Diagnosis and Management of Epithelial Ovarian Cancer.* Obstetrics & Gynecology, 2006. **107**(6): p. 1399-1410.

96.   Gupta, D. and C. Lis, *Role of CA125 in predicting ovarian cancer survival - a review of the epidemiological literature.* Journal of Ovarian Research, 2009. **2**(1): p. 13.

97.   Skates, S.J., et al., *Calculation of the Risk of Ovarian Cancer From Serial CA-125 Values for Preclinical Detection in Postmenopausal Women.* Journal of Clinical Oncology, 2003. **21**(10 suppl): p. 206-210.

98.   Nossov, V., et al., *The early detection of ovarian cancer: from traditional methods to proteomics. Can we really do better than serum CA-125?* American Journal of Obstetrics and Gynecology, 2008. **199**(3): p. 215-223.

99. Bast, R.C., et al., *CA 125: the past and the future.* The International journal of biological markers, 1998. **13**(4): p. 179-187.

100. Bagan, P., et al., *Value of cancer antigen 125 for diagnosis of pleural endometriosis in females with recurrent pneumothorax.* European Respiratory Journal, 2008. **31**(1): p. 140-142.

101. E Cross, S., et al., *AFM-based analysis of human metastatic cancer cells.* Nanotechnology, 2008. **19**: p. 384003.

102. Politi, E., et al., *Immunocytochemical panel for distinguishing between carcinoma and reactive mesothelial cells in body cavity fluids.* Diagnostic Cytopathology, 2005. **32**(3): p. 151-155.

103. Osterheld, M.-C., C. Liette, and M. Anca, *Image cytometry: An aid for cytological diagnosis of pleural effusions.* Diagnostic Cytopathology, 2005. **32**(3): p. 173-176.

104. Evans, E. and A. Yeung, *Apparent viscosity and cortical tension of blood granulocytes determined by micropipet aspiration.* Biophysical Journal, 1989. **56**(1): p. 151-160.

105. Bao, G. and S. Suresh, *Cell and molecular mechanics of biological materials.* Nat Mater, 2003. **2**(11): p. 715-725.

106. Hochmuth, R.M., *Micropipette aspiration of living cells.* Journal of Biomechanics, 2000. **33**: p. 15-22.

107. Chen, J., et al., *Twisting integrin receptors increases endothelin-1 gene expression in endothelial cells.* American Journal of Physiol-Cell Physiol, 2001. **280**(6): p. C1475-C1484.

108. Svoboda, K. and S.M. Block, *Biological Applications of Optical Forces.* Annual Review of Biophysics and Biomolecular Structure, 1994. **23**(1): p. 247-285.

109. Ashkin, A. and J.M. Dziedzic, *Optical trapping and manipulation of single living cells using infra-red laser beams.* Berichte der Bunsengesellschaft für physikalische Chemie, 1989. **93**(3): p. 254-260.

110. Dong, C. and X.X. Lei, *Biomechanics of cell rolling: shear flow, cell-surface adhesion, and cell deformability.* Journal of biomechanics, 2000. **33**(1): p. 35-43.

111. Burton, K. and D.L. Taylor, *Traction forces of cytokinesis measured with optically modified elastic substrata.* Nature, 1997. **385**(6615): p. 450-454.

112. Mahaffy, R.E., et al., *Scanning Probe-Based Frequency-Dependent Microrheology of Polymer Gels and Biological Cells.* Physical Review Letters, 2000. **85**(4): p. 880-883.

113. Haga, H., et al., *Elasticity mapping of living fibroblasts by AFM and immunofluorescence observation of the cytoskeleton.* Ultramicroscopy, 2000. **82**(1–4): p. 253-258.

114. Lulevich, V., et al., *Cell Mechanics Using Atomic Force Microscopy-Based Single-Cell Compression.* Langmuir, 2006. **22**(19): p. 8151-8155.

115. Collinsworth, A.M., et al., *Apparent elastic modulus and hysteresis of skeletal muscle cells throughout differentiation.* American Journal of Physiology - Cell Physiology, 2002. **283**(4): p. C1219-C1227.

116. Kuznetsova, T.G., et al., *Atomic force microscopy probing of cell elasticity.* Micron, 2007. **38**(8): p. 824-833.

117. Kelly, G.M., et al., *Bone cell elasticity and morphology changes during the cell cycle.* Journal of biomechanics, 2011. **44**(8): p. 1484-1490.

118. Yourek, G., M.A. Hussain, and J.J. Mao, *Cytoskeletal Changes of Mesenchymal Stem Cells During Differentiation.* ASAIO Journal, 2007. **53**(2): p. 219-228 10.1097/MAT.0b013e31802deb2d.

119. Radmacher, M., et al., *Measuring the viscoelastic properties of human platelets with the atomic force microscope.* Biophysical Journal, 1996. **70**(1): p. 556-567.

120. Ludwig, T., et al., *Probing cellular microenvironments and tissue remodeling by atomic force microscopy.* Pflügers Archiv - European Journal of Physiology, 2008. **456**(1): p. 29-49.

121. Touhami, A., B. Nysten, and Y.F. Dufrêne, *Nanoscale Mapping of the Elasticity of Microbial Cells by Atomic Force Microscopy.* Langmuir, 2003. **19**(11): p. 4539-4543.

122. Luby-Phelps, K., *Cytoarchitecture and Physical Properties of Cytoplasm: Volume, Viscosity, Diffusion, Intracellular Surface Area*, in *International Review of Cytology*, D.E.B. Harry Walter and A.S. Paul, Editors. 1999, Academic Press. p. 189-221.

123. Choquet, D., D.P. Felsenfeld, and M.P. Sheetz, *Extracellular Matrix Rigidity Causes Strengthening of Integrin–Cytoskeleton Linkages.* Cell, 1997. **88**(1): p. 39-48.

124. Bausch, A.R., W. Möller, and E. Sackmann, *Measurement of Local Viscoelasticity and Forces in Living Cells by Magnetic Tweezers.* Biophysical Journal, 1999. **76**(1): p. 573-579.

125. Merkel, R., et al., *A Micromechanic Study of Cell Polarity and Plasma Membrane Cell Body Coupling in Dictyostelium.* Biophysical Journal, 2000. **79**(2): p. 707-719.

126. Darling, E.M., *Force scanning: a rapid, high-resolution approach for spatial mechanical property mapping.* Nanotechnology, 2011. **22**(17): p. 175707.

CHAPTER 2

CELL STIFFNESS IS A BIOMARKER OF THE METASTATIC POTENTIAL OF OVARIAN CANCER CELLS

2.1   Abstract

The metastatic potential of cells is an important parameter in the design of optimal strategies for the personalized treatment of cancer. Using atomic force microscopy (AFM), we show, consistent with previous studies conducted in other types of epithelial cancer, that ovarian cancer cells are generally softer and display lower intrinsic variability in cell stiffness than non-malignant ovarian epithelial cells. A detailed examination of highly invasive ovarian cancer cells (HEY A8) relative to their less invasive parental cells (HEY), demonstrates that deformability is also an accurate biomarker of metastatic potential. Comparative gene expression analyses indicate that the reduced stiffness of highly metastatic HEY A8 cells is associated with actin cytoskeleton remodeling, and microscopic examination of actin fiber structure in these cell lines is consistent with this prediction. In addition, we further demonstrate the correlation between stiffness and metastasis using a pancreatic cancer cell line AsPC-1. We observed a reduction in invasiveness and an increase in stiffness upon treatment with N-acetyl-L-cysteine (NAC), a well known antioxidant, reactive oxygen species (ROS), scavenger and glutathione precursor. Changes in gene expression of NAC-treated cells are consistent with suppression of sonic hedgehog signaling, mesenchymal-to-epithelial transition, and repression of myelocytomatosis (MYC). The results of cell mechanics of these two different types of cancer types indicate that cell stiffness is modified for cancer cells in

23

the metastatic state. Therefore aberrant mechanical stiffness may potentially be useful as a biomarker to evaluate the relative metastatic potential of cancer cells.

2.2   Introduction

Cancer is a special type of disease with the hallmark of uncontrolled proliferation, underlying the abnormalities of cellular functions and properties is the cellular structure change. The distribution of the actin network plays an important role in determining a variety of cellular functions and the mechanical properties of single cells [1-3]. As cells undergo malignant transformation, their cytoskeletal structure changes from an organized to an irregular network, and this change subsequently reduces the stiffness of single cells [4, 5]. Studies have shown that abnormalities in the elastic properties of cells are associated with cancer progression [6-16]. For example, invasive tumor cells mechanically soften and modify their adhesion to extracellular matrix, which enhances their capacity to escape the primary tumor [16, 17]. Measurements of cancer cell stiffness, quantified by the Young's modulus, have shown a strong correlation between cell deformability and cell malignancy [4]. Similarly, the stiffness of metastatic cancer cells isolated from the pleural fluids of breast cancer patients was reported to be more than 70% lower, with a standard deviation over five times narrower, than benign reactive mesothelial cells [6]. The studies of mechanical properties of cancer cells discussed above imply that change of stiffness of single cells can indicate the presence of malignancy [14, 15, 18, 19].

The need for effective biomarkers for diseases is particularly important in the case of ovarian epithelial cancer, which is the most lethal of gynecological cancers. Ovarian cancer was ranked fifth among leading causes of cancer-related deaths of U.S. women in

2007 and its 5 year survival rate was 46% for all cases diagnosed within 1999-2005 [20]. Due to the unavailability of reliable screening in clinical practice and the asymptomatic course through early stages of the disease, the majority of ovarian cancer cases (68%) are diagnosed as metastatic disease with poor survival [21].

Exocrine pancreatic carcinoma is another lethal cancer ranking the fourth leading cause of cancer death in the US with an estimated 43,920 new cases and 37,390 deaths in 2012 [22]. The overall survival rate of pancreatic cancer of all stages combined is only 5.8% [22]. This is because 80-90% of pancreatic cancer patients are diagnosed with locally advanced or metastatic disease where currently available chemotherapy is of limited efficacy [23] due to aggressive growth and intrinsic or acquired resistance.

In this study of the mechanical properties of cells from several different ovarian cancer cell lines and non-malignant immortalized ovarian surface epithelial cells (IOSE), we demonstrate that cell stiffness not only distinguishes ovarian cancer cells from non-malignant cells, but also can distinguish more tumorigenic/invasive cancer cells from less tumorigenic/invasive types. We also found reduction in invasive activities as induced by N-acetyl-L-cysteine (NAC), which also accompanies an increase in cell stiffness in the pancreatic cancer cell line AsPC-1. Our findings indicate that measurement of cell stiffness of ovarian and perhaps other types of cancer cells may not only contribute to a better understanding of the physical and molecular mechanisms underlying tumor progression, but may also serve as a useful clinical tool in the assessment of metastatic potential.

## 2.3	Materials and methods

### 2.3.1	*Ovarian cell line growth and sample preparation*

Immortalized ovarian surface epithelium cells (IOSE) were generously provided by Dr. N. Auersperg (University of British Columbia, Vancouver, Canada) and cultured in 199/105 medium (1:1) supplemented with 15% fetal bovine serum (FBS, Atlanta Biologicals, Atalanta, GA) and 1% antibiotic-antimycotic solution (Mediatech-Cellgro, Manassas, VA). The ovarian cancer HEY and HEY A8 cell lines were provided by Dr. G. Mills (MD Anderson Cancer Center, Houston, TX) and grown in RPMI-1640 supplemented with 10% FBS and 1% antibiotic-antimycotic solution (R10 medium). The ovarian cancer OVCAR-3 and OVCAR-4 cell lines were procured from the Developmental Therapeutic Program (DTP) of the National Cancer Institute (NCI) (Bethesda, MD). Before AFM experiments, cells were plated into a Fluorodish (World Precision Instruments, Sarasota, FL) with an initial density of 10,000-20,000 cells/cm^2.

### 2.3.2	*Pancreatic cancer cell line growth culture*

Human pancreatic adenocarcinoma AsPC-1 cells [24] were obtained from ATCC (Manassas, Virginia, USA) and maintained in R10 medium (RPMI 1640 medium supplemented with fetal bovine serum (10%), L-glutamine (2 mM), penicillin (100 IU/mL), streptomycin (100 μg/mL) and amphotericin B (0.25 μg/mL)) in an atmosphere of humidified air with 5% CO_2.

### 2.3.3	*Chemicals to inhibit migration/invasion of pancreatic cancer cell*

N-acetyl-L-cysteine (NAC), a thiol antioxidant that serves as a precursor of intracellular cysteine and glutathione (GSH), has been previously shown to inhibit DNA synthesis and cell proliferation of various cancer cells in vitro, including bladder cancer[25], small cell

lung cancer [26] pheochromocytoma [27], signet ring cell gastric cancer[28], prostate cancer [29], and pancreatic cancer [30]. In addition, NAC suppressed phenotypic features associated with cancer cells, such as migration and invasion in bladder cancer [25, 31], melanoma, and Lewis lung carcinoma cells *in vitro* [32]. In "in vivo" experiments, NAC decreased tumor growth and spontaneous metastasis in a murine model of melanoma [32] and inhibited growth and metastasis of xenografted human breast cancer tumor cells in mice through loss of intratumoral vascular density [33]. Because of its promising cancer chemopreventive properties, as well as its ability to protect against cancer chemotherapy-induced side effects [34], NAC appears to be a compound of considerable promise in cancer chemoprevention and chemotherapy.

N-acetyl-L-cysteine (NAC) was obtained from Sigma-Aldrich (St. Louis, MO, USA) and its stock solution was prepared in sterile H_2O at 500 mM. 2',7'-dichlorodihydrofluorescein diacetate (DCFH2-DA) was obtained from Cayman Chemical (Ann Arbor, MI, USA) and used as 10 mM stock solution in ethanol. Hydro-Cy5 was kindly provided by Dr. Niren Murthy and Dr. Kausik Kundu from Georgia Institute of Technology (Atlanta, GA, USA) and used as 10 mM stock solution in ethanol. Buffered Neutral Formalin 10% was from EMD Chemicals, Inc (Gibbstown, NJ, USA).

2.3.4   *Cell proliferation and cytotoxicity assays of pancreatic cancer cells*

The cytostatic and cytotoxic activity of NAC on AsPC-1 cells was evaluated using the resazurin (AlamarBlue) assay[35], MTT assay[36] and crystal violet staining[37]. In all cell proliferation assays, 100 µL of cell suspension were plated in 96-well black-walled plates at 30,000 cells/mL in R10 medium and grown at 37°C in humidified air with 5% CO2 for 24h. Thereafter, 100 µL of NAC in growth medium at a concentration 2-fold of

the desired final concentration were added in quadruplicates and cells were incubated for 72 hours. For each concentration of NAC, tests were performed in 4 wells and there were 4 untreated control wells in the same column of the 96-well plate. All experiments were performed 2 times and consistency between plates was observed.

Resazurin assay was performed using the TOX-8 kit (Sigma-Aldrich, St. Louis, MO, USA). After 48-hour incubation of cells with NAC, 20 µL of the TOX-8 reagent were added to each well and incubated for the next 5 hours. The increase of fluorescence was measured at a wavelength of 590 nm using an excitation wavelength of 560 nm. The emission of control wells (no drug treatment) after the subtraction of a blank was taken as 100% and the results for treatments were expressed as a percentage of the control.

MTT assay: After 48-hour incubation with NAC, the medium was removed, cells were washed 2 times with 37°C warm PBS, and 100 µL of R-10 media with MTT reagent (3-[4, 5-dimethylthiazol-2-yl]-2, 5-diphenyltetrazolium bromide; 0.5 mg/mL) were added to each well. After 4 h incubation, medium with MTT was removed and formazan precipitate was dissolved in 200 µL DMSO during a 30 min shaking of the plate in the dark. Absorbance was read at 570 nm with a reference wavelength of 650 nm.

Crystal violet staining: After 48-hour incubation of cells with NAC, the medium was removed, cells were washed 2x with PBS and fixed with neutral buffered formalin at 4°C overnight. After fixation, cells were washed 2× with PBS, stained with 0.2% solution of crystal violet for 20 minutes at room temperature, washed 3× with purified water, air-dried and representative fields of cells were photographed. Subsequently, 100 µL of 10% acetic acid were added to each well and absorbance was read at 590 nm.

2.3.5 *Apoptosis assay, cell cycle analysis and cell senescence assay*

Apoptosis by dissipation of the mitochondrial membrane potential was determined using MitoPT™-TMRE assay kit (ImmunoChemistry Technologies, Bloomington, MN). This assay detects apoptosis through determination of the loss of mitochondrial membrane potential based on reduced fluorescence of the potentiometric dye tetramethylrhodamine ethylester (TMRE)[38]. 100 µL of suspension of AsPC-1 cells in R10 medium at density 106 cells/mL were plated into wells of a 96-well black-walled plate and incubated for 24 hours at 37°C. Thereafter, 100 µL of R10 media with 2x desired concentration of NAC were added so that the final concentration of NAC was 5 mM, 10 mM and 15 mM, and cells were incubated with NAC for 24 hours. Carbonyl cyanide m-chlorophenylhydrazone (CCCP) was used as a positive control at a final concentration of 50 µM and an incubation time of 45 minutes. Thereafter, medium was aspired from wells, cells were washed 1x with warm PBS, 100 µL of R10 medium with 100 nM TMRE were added, and the plates were placed in the incubator for 20 minutes. After incubation, cells were washed 1x with washing buffer and 100 µL of washing buffer added to each well. Cells were imaged by fluorescence microscope using an Olympus rhodamine filter peak excitation of 547 nm, emission filter 580 nm long pass, and fluorescence intensity of wells at 540nm excitation/570 nm emission were determined using the Synergy 4 microplate reader (Biotek, Winooski, VT).

Apoptosis was also determined by a FACS experiment using Cy5.5 Annexin V or Annexin V-FITC staining that detects externalization of membrane phosphatidylserine (PS) that accompanies apoptosis [39]. Cells were grown, harvested by trypsinization, stained with Cy5.5 Annexin V (BD Biosciences Pharmingen, San Diego, USA) or

Annexin V-FITC (Apoptosis Detection Kit; Calbiochem, San Diego, CA, USA) following manufacturer instructions, and analyzed by FACS using BD LSR II flow cytometer. Cy5.5 Annexin V and Annexin V-FITC signals were collected in PerCP-Cy5.5 or FITC channel, respectively.

AsPC-1 cells were treated with 5 mM, 10 mM or 15 mM NAC for 48 hrs and the distribution of cells in various phases of the cell cycle was determined by flow cytometry based on cellular DNA content as previously described [40]. DNA content histograms were deconvoluted using the Watson Pragmatic model implemented in FlowJo 7.6 software (Tree Star Inc., Ashland, OR). Each treatment was performed 3 times. Statistical significance of differences among proportions of cells in G1, S and G2/M phases of the cell cycle was tested between control and each NAC treatment (G1: control vs. 5 mM NAC, control vs.10 mM NAC, control vs. 15 mM NAC; S: control vs. 5 mM NAC, control vs. 10 mM NAC and so on) and p-values were adjusted for multiplicity testing.

Cellular senescence of AsPC-1 cells and AsPC-1 cells treated with 15 mM NAC for 42 hours was detected using Quantitative Cellular Senescence Assay Kit (SA- gal, fluorometric). This detection is based on measurement of acidic senescence-associated β-galactosidase activity [41] using membrane permeable fluorogenic substrate. Cells were plated into 25 cm2 cell culture treated flasks and 24 hours later, R10 medium with 15 mM NAC or R10 medium was added and cells were incubated for 42 hours. Thereafter, medium was removed, cells were washed with PBS and stained with SA-β-gal fluorogenic substrate following manufacturer's product manual and analyzed by FACS using FITC channel for detection of SA-β-gal activity.

2.3.6 *Atomic force microscopy*

We conducted atomic force microscopy (AFM) mechanical measurements [42, 43] on single ovarian epithelial cells. The AFM used in our experiments is the MFP-3D (from Asylum Research, Santa Barbara, CA) with a combined Nikon Ti inverted optical microscope (Nikon, Melville, NY) used to optically align the probe to the cells. The probes used in this study were MCST-AUHW (Bruker, Camarillo, CA) with a nominal spring constant of 0.03 *N/m*. To simplify the contact geometry and minimize the lateral strain of the sample during indentation, the cantilever tip is modified by attaching a plain silica microsphere of diameter 4.7 μm. Measurements were conducted in cell culture media at room temperature, with cells plated on the glass bottom of the Fluorodish. To eliminate the confounding effects of neighboring cells on cytoskeleton arrangement and morphology, single cells were measured.

For pancreatic cancer cell line AsPC-1, the stiffness of single cells with or without prior treatment with NAC was measured in the similar manner. Cells were grown in R10 medium supplemented with 15 mM NAC (treatment) or R10 medium only (control) and before measurements the medium was replaced with fresh RPMI-1640 medium

Prior to cell measurements, the cantilever was calibrated on the glass bottom of the Fluorodish using the thermal vibration method [44] with the resultant thermal spectrum fitted with Lorentzian function to determine the spring constant. The cells were indented approximately over the perinuclear region of individual cells. The indentation depth was chosen to be at least 1 μm in order to better simulate deformations which occur physiologically. The force versus indentation curves from each measurement were analyzed using a Hertzian contact model [45, 46] to obtain the Young's modulus of each

cell. A sketch of the experimental set up is shown in Figure 2.1*a*. Scanning electron micrograph of the beaded tip used in this experiment is shown in Figure 2.1 *b*. Examples of optical images obtained during cell indentation are shown in Figures 2.1, *c-g*.
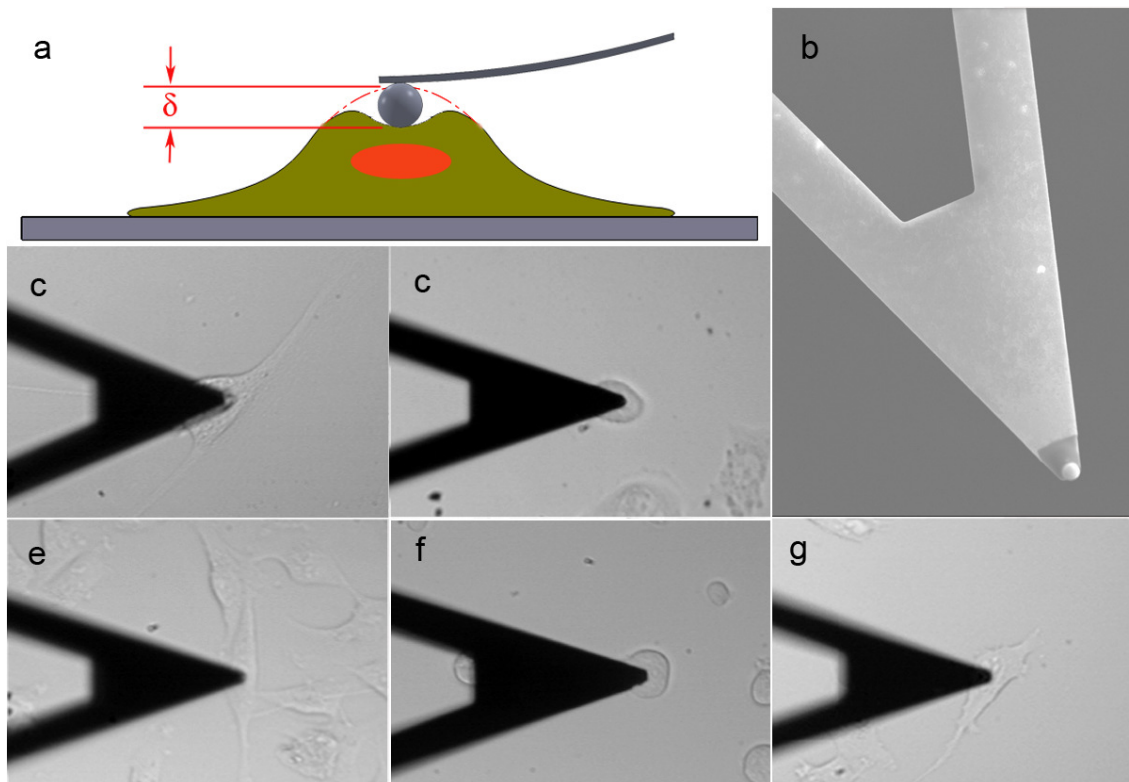
Figure 2.1: Experimental set up a) Sketch of measurements, the cantilever width is about 20 µm, b) SEM image of the beaded tip, stiffness measurements of single cells with AFM for c) IOSE, d) OVCAR4, e) HEY, f) OVCAR3 and g) HEYA8 cells

2.3.7 *Migration and invasion assays*

For ovarian cancer cell lines, the CytoSelect 24-well cell migration and invasion assay kit (Cell Biolabs, San Diego, CA) was used according to the manufacturer's instructions. For

the migration assay, 1.5×10^5 cells in serum-free DMEM/F12 medium containing 0.5% BSA, 2 mM $CaCl_2$ and 2 mM $MgCl_2$ were loaded into individual uncoated inserts with approximately 8 µm pore size. The inserts were placed in a 24-well plate containing RPMI-1640 medium supplemented with 10% FBS. After 3 h incubation at 37 °C in humidified air with 5% CO_2, the cells that migrated to the underside of the inserts were detached, lysed and quantified using CyQuant GR fluorescent dye on a plate reader at 480 nm/520 nm (Synergy 4, BioTek, Winooski, VT). Invasion assays were carried out in an identical manner with 32 h incubation using basement membrane matrix-coated inserts. All assays were carried out in triplicates with an initial time course study conducted to reach significant transmigration. The migration/invasion process is sketched in Figure 2.2.
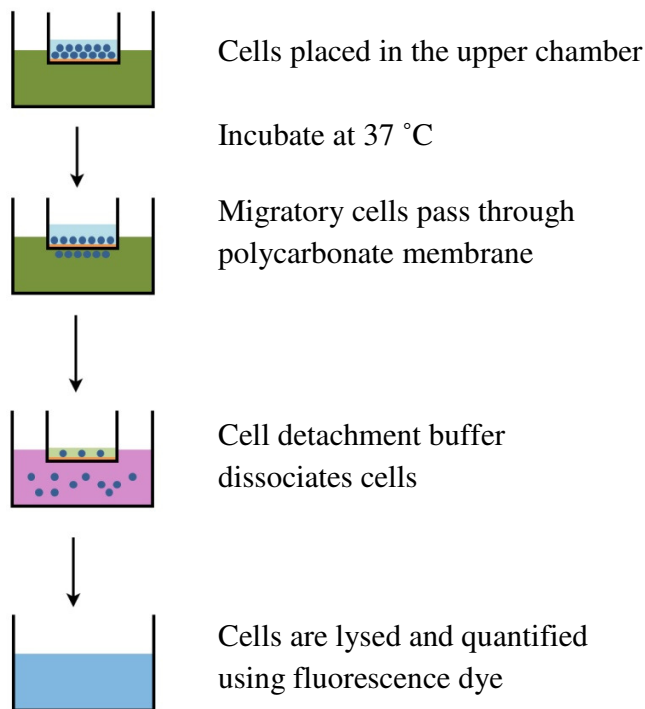
Figure 2.2: Sketch of migration/invasion measurements

In a similar manner, the effect of NAC on migration and invasion of AsPC-1 cells was determined using Cultrex 96 Well BME Cell Invasion Assay (Trevigen, Inc., Helgerman, CT, USA). This assay employed simplified Boyden chamber design with PET membranes coated with 0.5 X solution of Basement Membrane Extract (BME) following manufacturer's instructions. AsPC-1 cells were serum starved for 24 hours in DMEM/F12 medium supplemented with 0.4% BSA, penicillin (100 IU/mL), streptomycin (100 μg/mL) and amphotericin B (0.25 μg/mL) in an atmosphere of humidified air with 5% CO_2 and 12,500 cells/well in 50 μL media were loaded onto the upper chamber of the cell invasion device (treatment-15 mM NAC in DMEM/F12 medium supplemented with 0.4% BSA, penicillin (100 IU/mL), streptomycin (100 μg/mL) and amphotericin B (0.25 μg/mL) media; control - the same medium without

NAC). Cells were incubated at 37 oC in the CO2 incubator for 24 hours and the quantity of cells that invaded through the BME barrier was determined by fluorometry after staining with Calcein AM.

2.3.8 *Microarray and pathway enrichment analysis*

RNA was extracted from two non-confluent cultures of HEY and HEY A8 cells grown in R10 medium using Arcturus PicoPure RNA Isolation Kit (Applied Biosciences, Carlsbad, CA) according to the manufacturer's instructions and RNA integrity was verified using a Bioanalyzer RNA Pico Chip (Agilent Technologies, Santa Clara, CA). mRNA was labeled using the IVT Labeling Kit (Affymetrix, Santa Clara, CA) and biotin-labeled mRNA was hybridized on GeneChip Probe Arrays U133 Plus 2.0 (Affymetrix). Affymetrix .CEL files were processed using the Affymetrix Expression Console Software version 5.0 using the RMA 3'-expression workflow. The 4,746 features with lowest 10% values of the logarithm of signal intensities across all 4 chips were removed and the remaining 49,929 features were analyzed using Significance Analysis of Microarrays (SAM) version 4.0 [47] with following parameters: Response type: two-class unpaired; Test statistic: T-statistic; Number of permutations: 500; Data in log2 scale; No median centering. Genes were reported as differentially expressed between HEY and HEY A8 classes if they met following criteria: (i) False Discovery Rate =1.1% and (ii) absolute fold change (FC) $\geq$ 1.5.

Biological interpretations of the differential gene expression data were performed by pathway enrichment analysis using MetaCore 5.2 (GeneGO, St Joseph, MI). Significantly perturbed pathways and networks were identified by mapping up-regulated and down-regulated genes (combined and individually) onto GeneGO canonical pathway maps

35

(collection of manually curated signaling and metabolic pathways) and GeneGO process networks (manually curated network models of main cellular processes) [48].

GeneGO canonical pathway maps and process networks were ranked according to their relevance to the input set of genes using p-values calculated based on a hypergeometric distribution. Multiple testing correction was performed using False Discovery Rate with the adaptive threshold set to permit no more than 1 pathway/network incorrectly predicted as significantly enriched.

To further extend biological interpretation of the differential gene expression data, the topological significance analysis (TSA) of gene expression profile was performed using online tool from GeneGO Inc (http://topology.genego.com/zcgi/topology_scoring.cgi). This tool maps differentially expressed genes onto a GeneGO proprietary database of protein-protein interactions and identifies proteins that occupy topologically significant positions with respect to differentially expressed genes [49, 50]. Topologically significant genes ($p < 0.01$) were identified for all genes up-regulated in HEY A8 cells relative to HEY cells using the "transcriptional activation paths from all nodes" algorithm and subsequently mapped to GeneGO canonical pathway maps as described above.

2.3.9 *qPCR*

Selected genes (PRKAA2, TWF1 and MYLK), identified by microarray analysis as significantly differentially expressed between HEY A8 and Hey cells, were validated using predesigned TaqMan® Gene Expression Assays (Life Technologies, Grand Island, NY). RNA was extracted from 3 non-confluent cultures of HEY and HEY A8 cells (Arcturus PicoPure RNA Isolation Kit) and reverse-transcribed and amplified using Applause 3'-Amp system (NuGen Technologies, Inc., San Carlos, CA) according to the

36

manufacturer's instructions. qPCR assays were performed for each gene and each sample in 4 replicates using thermal cycling conditions recommended for TaqMan® Gene Expression Master Mix and fold change values between HEY A8 and Hey cells were determined using $2^{-\Delta\Delta Ct}$ method using GAPDH gene as internal control.

For pancreatic cancer cell line AsPC-1, qPCR was conducted in the similar manner, AsPC-1 cells were grown in R10 medium with or without 15 mM NAC for 8 and 24 hours, harvested by trypsinization, washed with PBS and flash frozen in liquid nitrogen. Total cell RNA was isolated using RNeasy Mini Kit (Qiagen) using manufacturer's protocol for purification of total RNA from animal cells using spin technology, including on-column DNase digestion to eliminate genomic DNA contamination. RNA purity and integrity were verified by A260/A280 ratio and capillary gel electrophoresis using the Bioanalyzer RNA Pico Chip (Agilent Technologies).

About 800 ng of total RNA were reverse transcribed with Superscript III First-Strand Synthesis System for RT-PCR (Invitrogen) to synthesize first-strand cDNA according to the manufacturer's instructions. The cDNA was amplified in 10 µL reactions (5 ng cDNA/reaction) with SsoFast EvaGreen Supermix (Bio-Rad, Hercules, CA) on a CFX96 Real-Time PCR System (Bio-Rad, Hercules, CA, USA). The cycling conditions: 1: 95 ˚C for 30 sec (enzyme activation), 2: 95 ˚C for 5 sec (denaturation), 3: 55 ˚C for 5 sec (annealing/extension). Selection of genes for qPCR evaluation was based on their role in proliferation and epithelial-to-mesenchymal transition of cancer cells. All primers were used at 500 nM (primer sequences for individual genes are listed in Table S1 of [51]). Fold changes for expression of evaluated genes and statistical significance of differences in expression of genes between NAC-treated and control cells were determined from

threshold cycles using REST 2005 software ver. 1.9.12 that implements ΔΔCt method and simple statistical randomization tests [52].

2.3.10 *Statistical analysis*

Overall statistical significance of differences in mean stiffness among cell types was tested using the Kruskal-Wallis test. Significance of differences between all pairs of cells was tested using Dunn's post test. Significance of differences in migration and invasion among IOSE, HEY and HEYA8 cells were tested by ANOVA, followed by Tukey's test for pairwise comparisons (*$p < 0.05$; **$p < 0.01$; ***$p < 0.001$. Kruskal-Wallis test, ANOVA and all post tests were performed using GraphPad Prism version 5.02 for Windows (GraphPad Software, San Diego, CA). Associations between cell stiffness and cell invasiveness, cell stiffness and cell migratory properties and cell stiffness and the degree of co-alignment of F-actin were tested using Pearson's product-moment correlation and Spearman's rank correlation and expressed as correlation coefficients (r and ρ, respectively). Correlation analysis was performed using the free statistical software R [53].

For AsPC-1 cells, significance of differences between means of two-class data was tested by Student's t-test and expressed as a two-tailed p-value. Where necessary, multiplicity adjustment was performed using Holm's step-down method.

2.3.11 *Fluorescence imaging and analysis of F-actin*

We imaged the labeled F-actin network of each cell line using fluorescence microscopy. Cells were grown on a glass coverslip to a density of 5,000 cells/cm^2. The cover slip with plated cells was placed in a well of a 6-well plate with 2 mL cell culture media. The cells were incubated at 37 ^{o}C overnight and then stained with fluorochrome-conjugated

38

phalloidin. The cells were stained by first fixing with 1 mL 4% formaldehyde in PBS (pH 7.4) for 10 min and permeabilizing with 1 mL 0.2% TX-100, blocking with 1% BSA for 20 min and incubating for one hour with 1:20 Alexa Fluor 546 phalloidin (Life Technologies, Grand Island, NY) in 1% BSA. All steps during the staining process were conducted at room temperature in a dark room. After staining, the cells were sandwiched between the glass coverslip and a glass slide, mounted with ProLong Gold and sealed with nail polish. Multiple images of each cell line were taken using a Nikon Ti microscope (Nikon, Melville, NY) with the TRITC excitation/emission filter set. The analysis was limited to single cells which were not in contact with other cells.

The alignment of the actin fibers was analyzed by quantifying an orientation parameter for actin filaments. A two-dimensional Fast Fourier Transform (FFT) was applied to the original fluorescence images using MATLAB routines (The MathWorks, Natick, MA). From the transformed image, we developed custom MATLAB codes calculating the angular amplitude of the FFT by summing the square of the FFT components, from which the orientation distribution of actin filaments was determined as a function of angle. The mathematical algorithms calculating the orientation distribution function were based upon those reported previously in the literature [54]. The method is illustrated in Figure 2.3 with a representative fluorescence image of an IOSE cell.
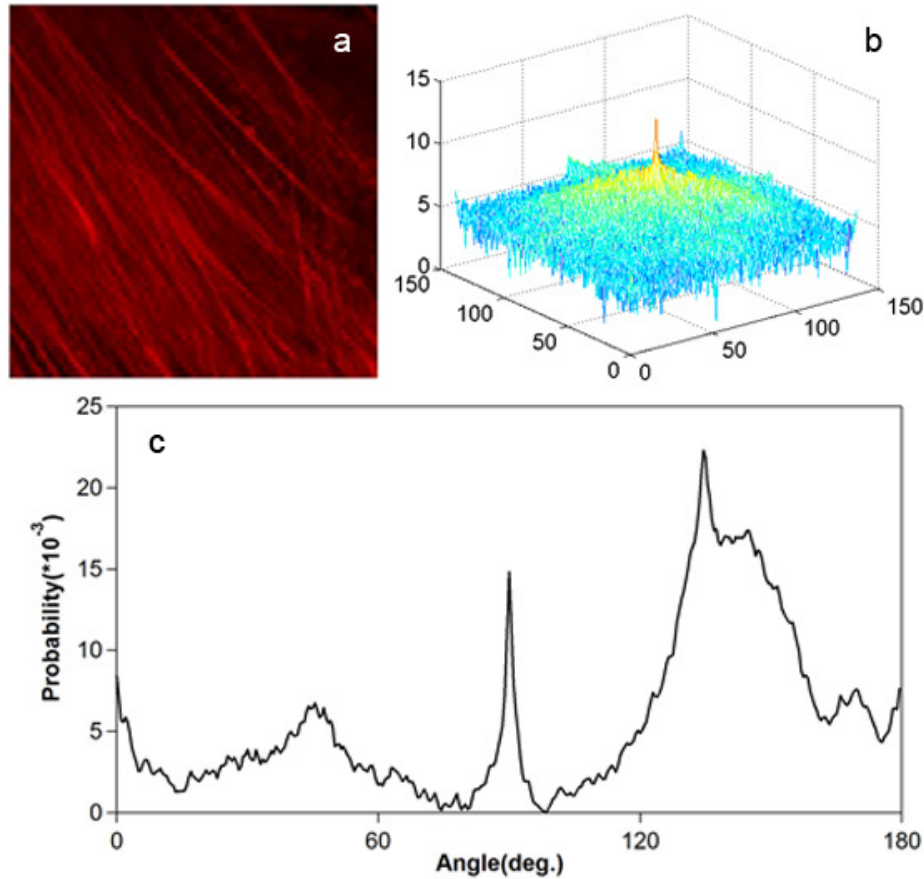
Figure 2.3: Calculation of the orientation distribution function from fluorescence image and Fast Fourier Transform. a) Original fluorescence image, b) mesh representation of the transformed image, and c) orientation distribution function.

2.4 Results and discussion

2.4.1 *Cell stiffness is a biomarker of metastatic (migratory/invasiveness) potential of ovarian cancer*

Representative force-indentation curves obtained from mechanical probing of individual cells are plotted in Figure 2.4*a*. Each curve represents the applied force necessary to indent an individual ovarian cell from the IOSE and HEY cell lines. The probe contacts the cell at an indentation of 0 µm. Since the slope at a point of each force-indentation curve is related to the cell stiffness, variability of slopes for each probed cell in a given

cell line indicate variability of stiffness among individual cells from the same culture. In general, curves corresponding to non-malignant IOSE cells have larger slopes than those corresponding to ovarian cancer HEY cells and are therefore stiffer.
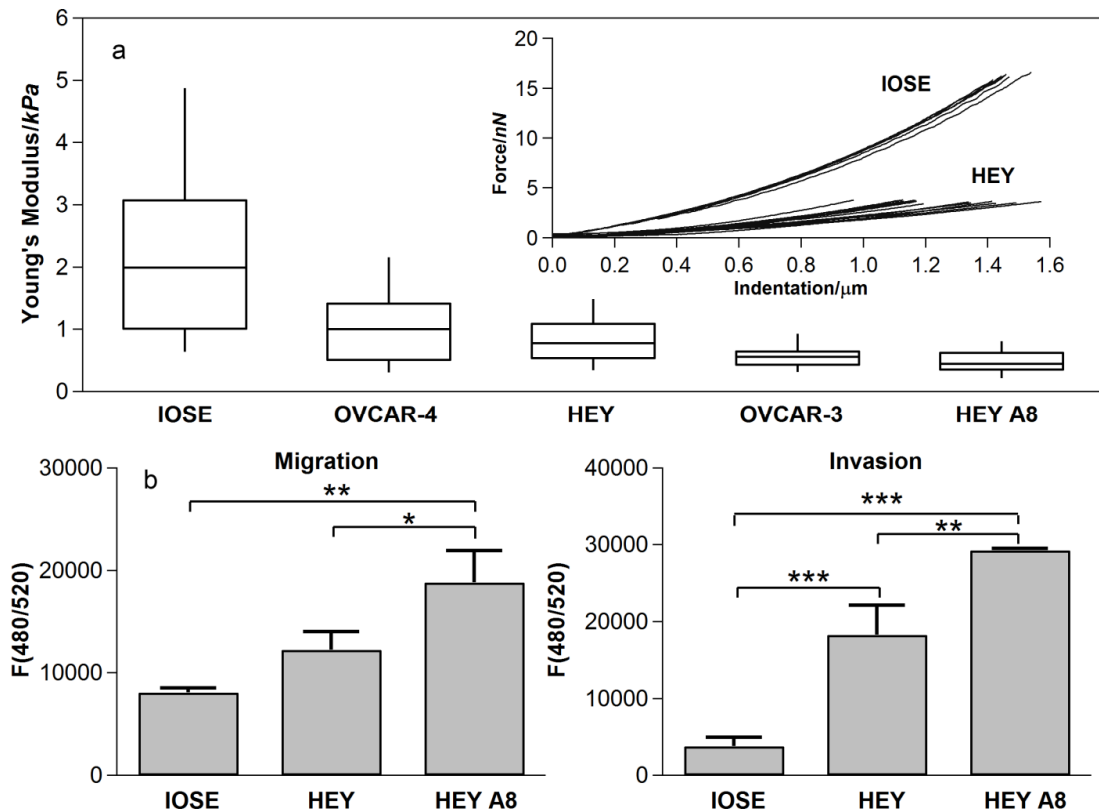
Figure 2.4: Stiffness distribution of cells and results of migration and invasion test. a) Box-and-whisker plots of stiffness of single cells for different cell lines, the percentiles are 10%, 25%, 50%, 75% and 90%, the inset shows the representative force curves of IOSE and HEY. Overall difference among means is significant (p-value$<2.2\times10^{-16}$, Kruskal-Wallis); pairwise differences are significant between IOSE and HEY, HEY A8 and OVCAR-3 cells, between HEY A8 and HEY cells and between HEY A8 and OVCAR-4 cells ($p<0.05$, Dunn's post test); b) Migration and invasion tests for IOSE, HEY and HEY A8 cells. F(480/520) is a fluorescence intensity at 480 nm excitation and 520 nm emission, which is proportional to the number of migrating or invading cells.

41

The force curves were analyzed with a Hertzian contact model to determine the corresponding Young's modulus of individual cells. We determined the Young's modulus for different ovarian epithelial cell lines, including non-malignant IOSE and a variety of cancer cell lines (OVCAR-3, OVCAR-4, HEY, and HEY A8). The distribution of Young's modulus of individual cells from different cell lines is depicted in the box-and whisker plots (Figure 2.4a). IOSE demonstrated higher mean stiffness than any of the ovarian cancers. The overall difference among cell lines was significant ($p < 2.2 \times 10^{-16}$) with the following pairs displaying significant differences ($p < 0.05$): IOSE vs OVCAR-3, IOSE vs HEY, IOSE vs HEY A8, OVCAR-4 vs HEY A8, and HEY vs HEY A8. The mean Young's moduli and standard deviations of these cells are summarized in Table 2.1. The non-malignant IOSE cells demonstrated higher intrinsic variability in cell stiffness than cells from any ovarian cancer cell line, which is consistent with the previously reported higher variability in stiffness of benign cells relative to breast cancer cells isolated from pleural fluids [6].

Table 2.1: Mean Young's moduli and corresponding standard deviations, with sample size in parentheses. Tests of significance tests between different cell populations are also included.

	IOSE (n=55)	OVCAR4 (n=18)	HEY (n=60)	OVCAR3 (n=20)	HEYA8 (n=59)
Mean stiffness/kPa	2.472	1.120	0.884	0.576	0.494
Standard deviation/kPa	2.048	0.865	0.529	0.236	0.222
Dunn's Multiple Comparison Test	**Difference in rank sum**		**Significant?** $p < 0.05$?		**Summary**
IOSE vs OVCAR-4	46.17		No		ns
IOSE vs HEY	55.91		Yes		***
IOSE vs HEYA8	105.7		Yes		***
IOSE vs OVCAR-3	91.40		Yes		***
OVCAR-4 vs HEY	9.742		No		ns

Table 2.1 (Continued)

OVCAR-4 vs HEYA8	59.49	Yes	**
OVCAR-4 vs OVCAR-3	45.23	No	ns
HEY vs HEYA8	49.75	Yes	***
HEY vs OVCAR-3	35.49	No	ns
HEYA8 vs OVCAR-3	-14.26	No	ns

ns: not significant; **: $p<0.01$; ***: $p<0.001$

Notably, HEY and HEY A8 cells derived from the same tumor specimen [55] displayed significant differences in stiffness, with HEY A8 cells being more compliant (Figure 2.2*a*). This finding is significant in that these isogenic cells also differ in their tumorigenicity in nude mice, whereby HEY A8 but not HEY cells are tumorigenic after intraperitoneal injection to nude mice [55]. To explore the relationship between mechanical properties of these ovarian cell lines and their metastatic potential, we examined the migratory and invasive properties of HEY and HEY A8 cells relative to IOSE using *in vitro* assays. HEY A8 cells displayed the greatest invasive and migratory activity followed by HEY cells and the IOSE control cells (Figure 2.4*b*) indicating that relative stiffness is inversely correlated with the indicators of metastatic potential (migration and invasiveness). These findings, summarized in Figure 2.5 and Table 2.2, are consistent with previous reports linking cellular deformability with tumorgenic and metastatic potential [4, 9, 47].
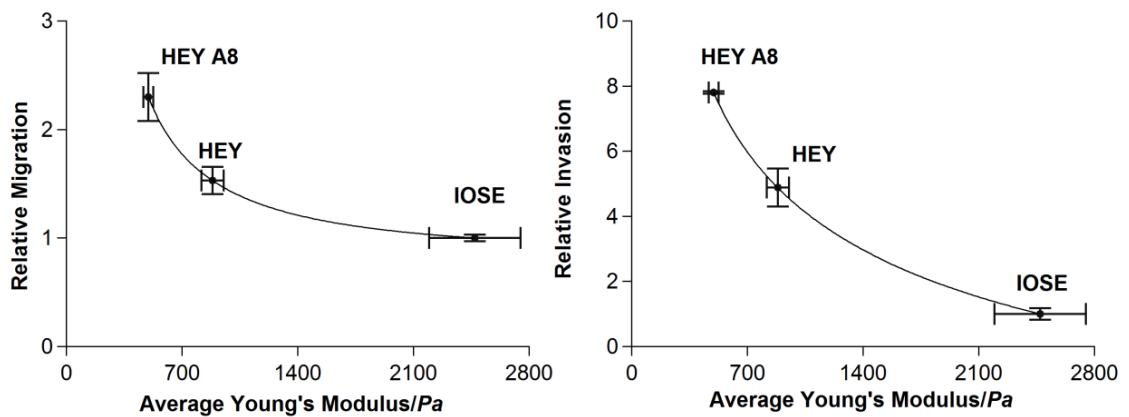
Figure 2.5: Scatterplots of relative migration and invasion versus average stiffness for IOSE, HEY and HEY A8 cells (migration and invasion of IOSE cells = 1). The data points are fitted with power law for clarity. Error bars: standard errors of means.

Table 2.2: The strength of association between stiffness/migratory and stiffness/invasive properties expressed as Pearson's product-moment (r) and Spearman's rank (ρ) correlation coefficients and their p-values.

	Pearson		Spearman	
	r	*p*-val	ρ	*p*-val
Stiffness/relative migration	-0.894	0.2956	-1	0.3333
Stiffness/relative invasion	-0.9670	0.1641	-1	0.3333

2.4.2   *Gene expression profiling of HEY and HEY A8 cells links increased metastatic potential with changes in actin-mediated cytoskeletal remodeling pathways*

Having established that the acquisition of decreased stiffness in HEY A8 cells relative to HEY cells is correlated with an increase in metastatic potential (i.e., cell migration and invasiveness), we performed a comparative gene expression analysis (DNA microarray) of these two cell lines in order to gain insight into the possible molecular basis of the acquired phenotype.

Using Significance Analysis of Microarrays (SAM) we identified 3,641 differentially expressed features between these cell lines (supplemental file 1 of [56]) and determined that 1,258 genes were up-regulated and 1,272 down-regulated in HEY A8 relative to HEY cells (15 genes displayed discordant changes in expression between HEY and HEY A8 cells for redundant probe sets). Significantly enriched GeneGO pathways (Table 2.3) and process networks (Table 2.4) corresponding to our set of differentially expressed genes indicate that differences between HEY and HEY A8 cells include changes in mitotic phase of cell cycle (spindle assembly/chromosome separation, spindle microtubules), regulation of epithelial-to mesenchymal transition (EMT), cytoskeletal remodeling, cell adhesion, and regulation of CFTR (cystic fibrosis transmembrane conductance regulator).

Table 2.3: Significantly enriched Genego Maps.

Map	p-val	Ratio
Up- and down-regulated genes (FDR=0.08)		
Cell cycle: The metaphase checkpoint	1.548e-12	26/36
Cell cycle_Role of APC in cell cycle regulation	3.719e-11	23/32
Cell cycle_Chromosome condensation in prometaphase	2.895e-9	16/20
Cell cycle_Spindle assembly and chromosome separation	3.758e-9	21/32
Cell cycle_Role of Nek in cell cycle regulation	7.795e-6	16/29
Cell cycle_Start of DNA replication in early S phase	2.396e-5	16/31
Immune response_MIF - the neuroendocrine-macrophage connector	1.130e-4	15/31
Regulation of CFTR activity (norm and CF)	2.908e-4	17/40
Cell adhesion_ECM remodeling	3.202e-4	20/51
Reproduction_Progesterone-mediated oocyte maturation	7.001e-4	14/32
Development_Regulation of epithelial-to-mesenchymal transition (EMT)	1.070e-3	22/63
Cell adhesion_Plasmin signaling	1.443e-3	14/34
Up-regulated genes (FDR=0.07)		
Cell cycle_The metaphase checkpoint	2.935e-19	26/36

Table 2.3 (Continued)

Cell cycle_Role of APC in cell cycle regulation	4.422e-17	23/32
Cell cycle_Chromosome condensation in prometaphase	1.880e-13	16/20
Cell cycle_Spindle assembly and chromosome separation	3.278e-13	20/32
Cell cycle_Start of DNA replication in early S phase	4.183e-9	16/31
Cell cycle_Role of Nek in cell cycle regulation	1.204e-7	14/29
dCTP/dUTP metabolism	2.508e-4	13/45
Cell cycle_Initiation of mitosis	3.762e-4	9/25
Immune response_MIF - the neuroendocrine-macrophage connector	4.937e-4	10/31
Reproduction_Progesterone-mediated oocyte maturation	6.565e-4	10/32
Oxidative stress_Role of ASK1 under oxidative stress	7.419e-4	8/22
dATP/dITP metabolism	1.393e-3	13/53
wtCFTR and deltaF508 traffic / Membrane expression (norm and CF)	1.431e-3	8/24
Down-regulated genes (FDR=0.14)		
Development_Regulation of epithelial-to-mesenchymal transition (EMT)	5.125e-5	16/63
Cell adhesion_Plasmin signaling	3.750e-4	10/34
Cytoskeleton remodeling_TGF, WNT and cytoskeletal remodeling	5.918e-4	20/107
Development_TGF-beta-dependent induction of EMT via RhoA, PI3K and ILK	7.233e-4	11/43
Cell adhesion_ECM remodeling	9.434e-4	12/51
Development_PEDF signaling	1.233e-3	10/39

Table 2.4: Significantly enriched Genego Process Networks.

Network	p-val	Ratio
Up and down-regulated genes (FDR=0.04)		
Cell cycle_Mitosis	5.493e-20	83/177
Cytoskeleton_Spindle microtubules	2.712e-16	56/108
Cell cycle_Core	6.026e-15	56/114
Cell cycle_G2-M	1.752e-10	73/204
Cell cycle_S phase	4.428e-8	53/147
Protein folding_Response to unfolded proteins	1.236e-5	27/68
Protein folding_ER and cytoplasm	6.199e-5	19/44
DNA damage_Checkpoint	9.910e-5	39/124
Inflammation_MIF signaling	2.442e-4	36/116
Cell cycle_G1-S	4.239e-4	46/163
Neurophysiological process_Circadian rhythm	4.631e-4	19/50

Table 2.4 (Continued)

Reproduction_Progesterone signaling	5.458e-4	52/192
Muscle contraction_Nitric oxide signaling in the cardiovascular system	1.161e-3	27/86
Development_Regulation of angiogenesis	1.273e-3	54/208
Transcription_mRNA processing	1.652e-3	43/159
Cell cycle_Meiosis	2.033e-3	30/102
Protein folding_Folding in normal condition	2.288e-3	33/116
Cell adhesion_Integrin-mediated cell-matrix adhesion	2.454e-3	53/209
Development_EMT_Regulation of epithelial-to-mesenchymal transition	2.454e-3	53/209
DNA damage_BER-NER repair	3.018e-3	29/100
Cell cycle_G0-G1	3.849e-3	22/71
Cytoskeleton_Cytoplasmic microtubules	3.860e-3	32/115
Apoptosis_Apoptotic nucleus	5.767e-3	40/155
Up-regulated genes (FDR=0.04)		
Cell cycle_Mitosis	1.026e-33	76/177
Cytoskeleton_Spindle microtubules	3.704e-26	52/108
Cell cycle_Core	7.111e-23	50/114
Cell cycle_G2-M	5.794e-19	63/204
Cell cycle_S phase	9.838e-16	48/147
Transcription_mRNA processing	8.204e-8	37/159
Cell cycle_G1-S	4.918e-7	36/163
DNA damage_Checkpoint	5.834e-7	30/124
DNA damage_BER-NER repair	2.709e-6	25/100
Cytoskeleton_Cytoplasmic microtubules	3.723e-5	25/115
Cell cycle_Meiosis	4.127e-5	23/102
Muscle contraction_Nitric oxide signaling in the cardiovascular system	2.527e-4	19/86
Protein folding_Folding in normal condition	3.250e-4	23/116
Apoptosis_Apoptotic nucleus	3.917e-4	28/155
DNA damage_MMR repair	4.318e-4	14/56
Cytoskeleton_Regulation of cytoskeleton rearrangement	1.094e-3	30/181
Protein folding_Response to unfolded proteins	1.128e-3	15/68
Protein folding_ER and cytoplasm	1.755e-3	11/44
DNA damage_DBS repair	1.893e-3	20/108
Protein folding_Protein folding nucleus	2.037e-3	13/58
Apoptosis_Apoptotic mitochondria	2.394e-3	15/73
Proteolysis_Ubiquitin-proteasomal proteolysis	2.524e-3	27/166
Reproduction_Progesterone signaling	5.399e-3	29/192

Table 2.4(Continued)

Down-regulated genes (FDR=0.07)

Development_EMT_Regulation of epithelial-to-mesenchymal transition	2.152e-5	36/209
Development_Regulation of angiogenesis	4.657e-5	35/208
Signal Transduction_TGF-beta, GDF and Activin signaling	1.730e-4	26/146
Cell adhesion_Platelet-endothelium-leucocyte interactions	2.006e-4	29/172
Inflammation_MIF signaling	5.717e-4	21/116
Neurophysiological process_Circadian rhythm	6.861e-4	12/50
Inflammation_Protein C signaling	7.018e-4	18/94
Blood coagulation	7.713e-4	17/87
Proliferation_Negative regulation of cell proliferation	1.615e-3	27/177
Reproduction_FSH-beta signaling pathway	3.870e-3	23/152
Proteolysis_ECM remodeling	4.364e-3	15/85
Proteolysis_Connective tissue degradation	4.593e-3	19/119
Signal transduction_Androgen receptor signaling cross-talk	4.827e-3	12/62
Translation_Elongation-Termination	5.344e-3	22/147

To further explore the potential biological significance of the differences in gene expression between HEY and HEY A8 cells, we employed topological significance analysis. Using this approach we identified 1,108 unique Entrez Gene IDs corresponding to topologically relevant proteins associated with up-regulated genes in HEY A8 cells (Supplemental file 2 of [56]). Significantly enriched GeneGO pathways for these topologically relevant proteins (360 pathways at FDR=0.26%) suggest considerable biological differences between HEY and HEY A8 cells including those that could not be identified on transcriptional level (supplemental file 3 of [56]). A full discussion of these results is beyond the scope of this paper and will be presented elsewhere. Here we will limit our discussion to those changes most relevant to the observed differences in cell stiffness discussed above.
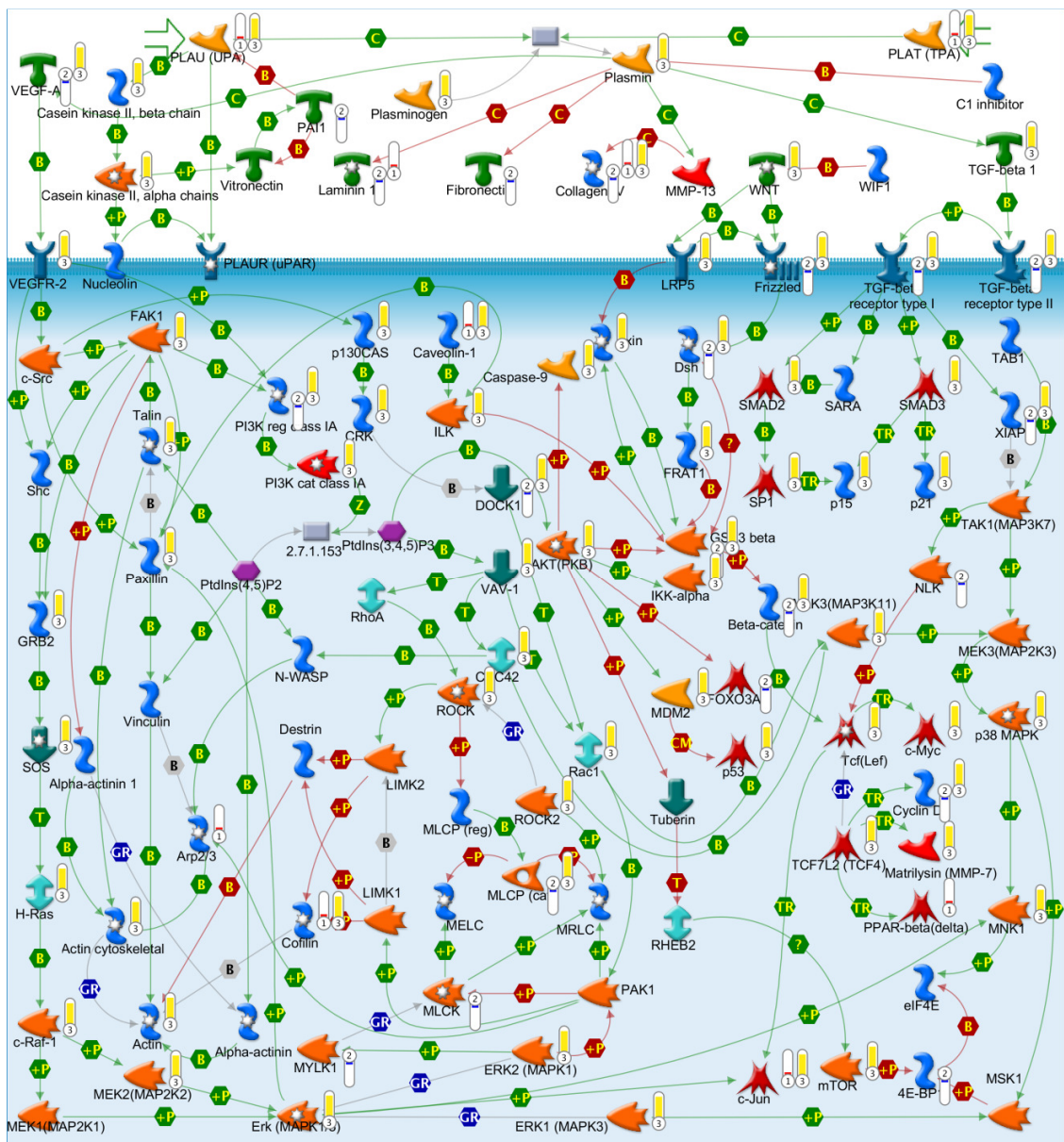
Figure 2.6: TGF, WNT and cytoskeletal remodeling GeneGO pathway. Red thermometer: genes transcriptionally up-regulated in HEY A8 cells; blue thermometer: genes transcriptionally down-regulated in HEY A8 cells; yellow thermometer: proteins topologically relevant to the set of up-regulated genes.

The top scoring GeneGO pathway for topologically relevant proteins (supplemental file 3 of [56]) is the "TGF, WNT and cytoskeletal remodeling pathway" (Figure 2.6). This pathway was also identified as significantly enriched for genes down-regulated in HEY

A8 cells (Table 2.3). These findings indicate that differences in stiffness between HEY and HEY A8 cells are related to cytoskeletal remodeling. Our findings support earlier predictions that the basis of reduced stiffness associated with cancer [57] and highly invasive cells [58] may be associated with cytoskeletal remodeling. Further support for this conclusion comes from TSA which found various isophorms of actin superfamily topologically significant for genes up-regulated in HEY A8 cells (supplemental file 2 of [56]), as well as from differential expression analysis, which found that the actin-monomer-binding proteins CFL2, TWF1 and PFN1 that regulate the incorporation of actin monomers into filaments [59] are overexpressed in HEY A8 cells. Overexpression of cofilin-2 (CFL2) enhances the rate of actin filament turnover by depolymerizing filaments at their pointed ends [60] while twinfilin (TWF1) functions as an actin-monomer-sequestering protein that also severs actin filaments to promote filament disassembly *in vitro* and its rapid turnover *in vivo* [61]. The fact that myosin light chain kinase (MYLK), which promotes an actin-activated myosin motor activity and tension generation [62], is significantly down-regulated in HEY A8 cells further supports the role of stress fibers in observed difference in cell stiffness. Interestingly, BDM and ML-7, the inhibitors of MYLK, have been previously reported to induce softening of fibroblast cell lines [63]. Phosphorylation of myosin light chain, stress fiber formation, and subsequent increase in cell stiffness can be also induced via RhoA/Rho kinase pathway [64], which is inactivated by cAMP-dependent protein kinase (PKA) [65]. We found that regulatory (PKAR2A, PKAR2B) and catalytic (PKACB) subunit genes of PKA are significantly overexpressed in HEY A8 relative to HEY cells suggesting PKA-dependent inactivation of RhoA/Rho kinase pathway in HEY A8 cells. *q*PCR validation of differential gene

expression data from microarray experiment confirmed overexpression of PRKAA2 and TWF1 genes with respective fold changes 3.89 and 2.63 and decreased expression of MYLK gene with fold change -2.0 in HEY A8 cells relative to HEY cells, as shown in Figure 2.7.
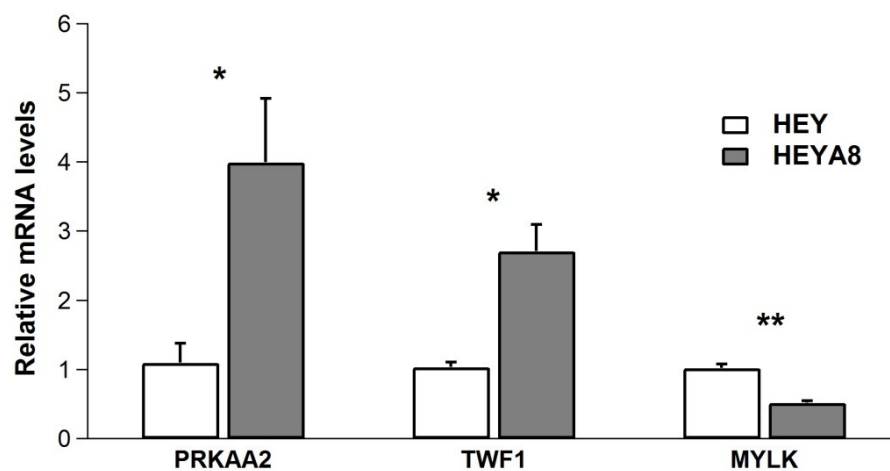
Figure 2.7: Results of qPCR validation of microarray gene expression data for selected genes. FC: gene expression fold changes in HEYA8 relative to HEY cells. Error bars: standard errors of means, N = 3. *: $p < 0.05$; **: $p < 0.01$ (Student's t-test).

2.4.3 *Microscopic analyses of ovarian cancer and control cells confirm that actin-mediated cytoskeletal remodeling is associated with change in metastatic potential*

Since our molecular analyses indicated that actin-mediated cytoskeletal remodeling may be a major contributor to the observed differences in cell stiffness between HEY and the more invasive/tumorigenic HEY A8 cells, we tested the hypothesis by examining the cytoskeletal structure of HEY and HEY A8 cells relative to other ovarian cancer cells (OVCAR-3, OVCAR-4) and non-malignant immortalized ovarian surface epithelial cells

(IOSE). The results presented in Figure 2.8 display denser, well-aligned F-actin with longer stress fibers in IOSE relative to all of the ovarian cancer cells. This is consistent with previously reported comparisons between normal and cancer cells [2, 4].
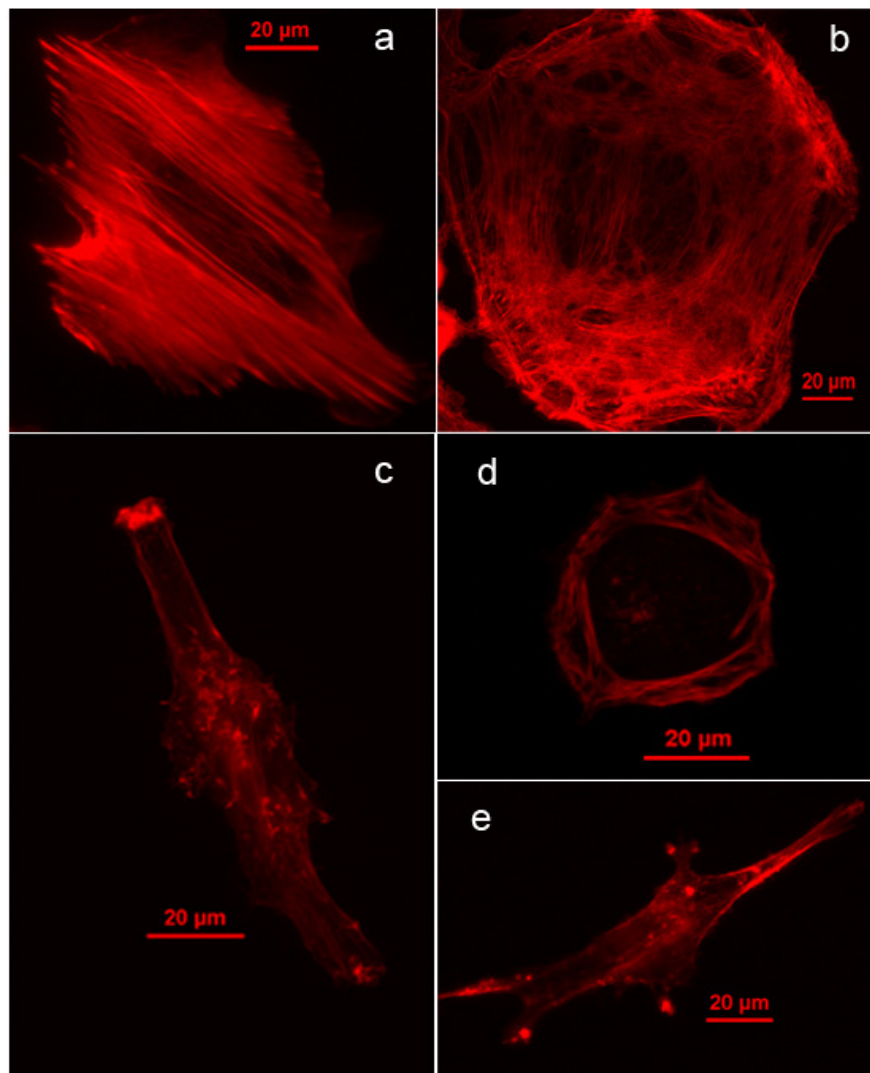
Figure 2.8: Fluorescence images of F-actin. (A) IOSE, (B) OVCAR-4, (C) HEY, (D) OVCAR-3 and (E) HEY A8

In addition, the degree of co-alignment of F-actin fibers among the various examined cell lines correlated with the observed difference in cells stiffness. For example, for the stiffer IOSE cells, the actin filaments are distributed through the cell body, with most F-actin bundles aligned along the long axis of the cell with well-defined stress fibers and focal contacts. In contrast, actin filaments in the softer ovarian cancer cells are less organized and F-actin bundles are oriented randomly with disrupted, short segments. In OVCAR-4 cells, actin filaments are aligned only locally and form a tangled network. In HEY cells, the actin filaments break into shorter segments and display reduced co-alignment. F-actin in OVCAR-3 cells maintains a cortical structure with most filaments lying in the peripheral region of the cell, though at a relatively low density. HEY A8 cells show similar characteristics of F-actin distribution to HEY cells, but with a lower density. Since the actin cytoskeleton contributes to the mechanical properties of the cells, observed variations are consistent with differences in cell stiffness and with previous reports [1, 66].

We analyzed the degree of co-alignment of F-actin in all five cell lines by using orientation distribution function. The results are displayed in Figure 2.9, orientation distributions of F-actin differ among the five ovarian cell lines. In non-malignant IOSE cells, most of F-actin bundles were aligned along the long axis of the cell, which is ~135˚. In contrast, OVCAR-4 cells display several orientations of F-actin, indicating that actin filaments are neither uniformly aligned, nor evenly distributed. This result is readily apparent from the fluorescence image in Figure 2.8.
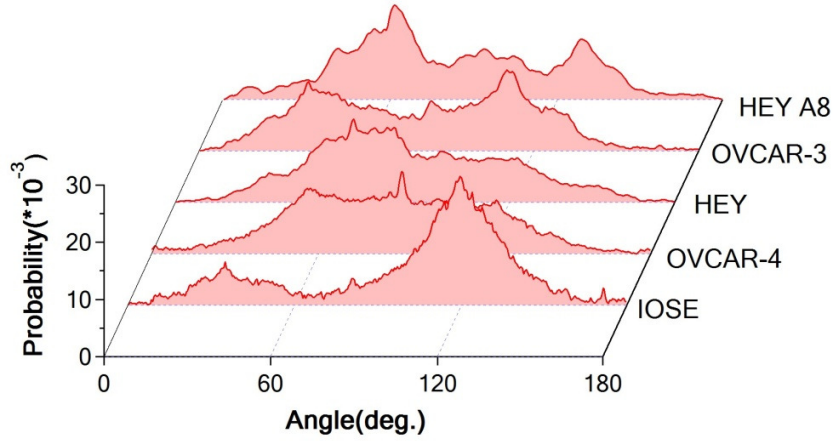
Figure 2.9: Representative orientation distribution function for each cell line.

To evaluate the contribution of degree of F-actin co-alignment to single cell stiffness, a parameter D, defined as $D = \int_0^\pi |P(\theta) - P_0(\theta)|d\theta$ was used to quantify the degree of co-alignment of F-actin from the orientation distribution functions, where $P(\theta)$ represents the orientation distribution function, which is the probability for a fiber oriented at the angle of θ in the fluorescence image. $P_0(\theta)$ is the orientation distribution function for the extreme case where F-actin are completely randomly distributed and therefore has a value of $P_0(\theta) = 1/180$. In the extreme case in which all actin fibers are oriented randomly without any preference, the orientation distribution function should be a constant and independent of angle. From the definition of D, a higher value of D indicates an increasing deviation from random alignment and a higher degree of co-alignment of F-actin. The method is illustrated in Figure 2.10. The relationship between the degree of co-alignment of F-actin and stiffness of single cell is plotted in Figure 2.9*b*, which shows strong and significant positive correlation ($r = 0.99834$ with p-val $= 8.064\times10^{-5}$ and $\rho=1$ with p-val $= 0.01667$). This result suggests that changes in co-alignment of F-actin

bundles could also contribute to the differences in cell stiffness within the examined ovarian cell lines.
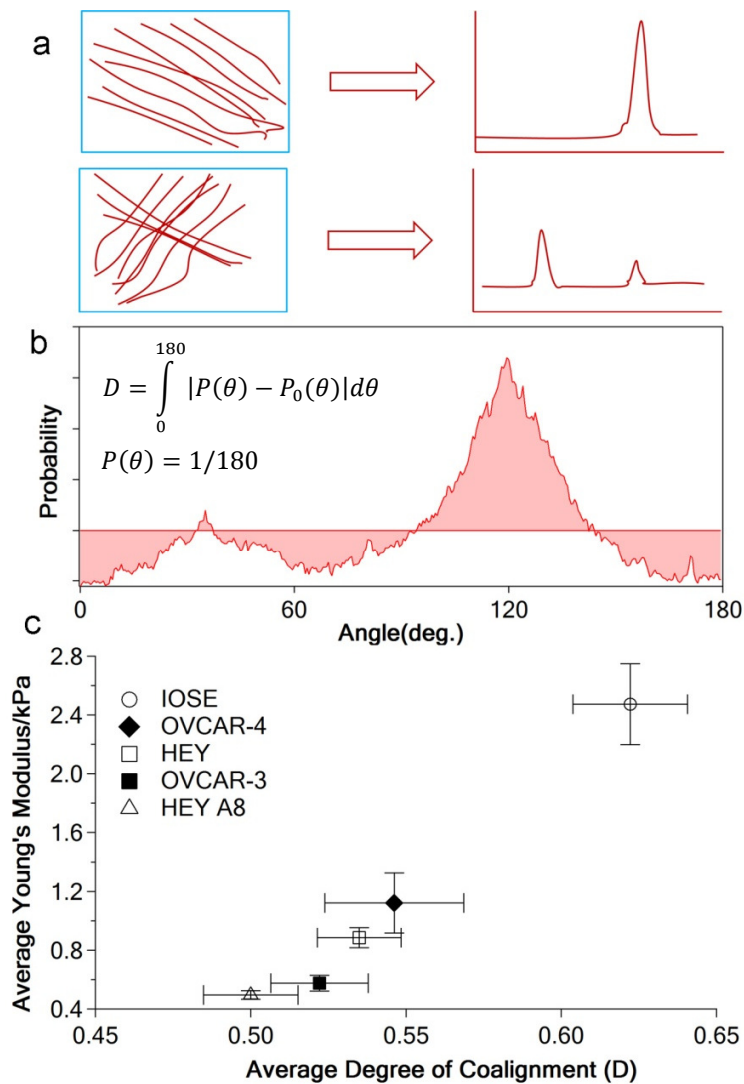
Figure 2.10: Quantification of F-actin coalignment and correlation with stiffness, a) Correspondence between F-actin orientations and orientation distribution functions; b) Quantification of orientation distribution function; and c) stiffness versus degree of coalignment of F-actin, error bar represents standard error of mean (SEM).

2.4.4 *NAC inhibits growth of pancreatic cancer AsPC-1 cell culture*

The MTT assay demonstrated that 48 hour treatment with NAC significantly inhibits growth of AsPC-1 cells at drug concentrations of 10 mM and 15 mM (Figure 2.11, insert MTT and Table 2.5). According to the results of crystal violet staining, NAC significantly inhibited growth of AsPC-1 cell culture at 10 mM and 15 mM, but also at 1 mM concentration, although the effect size at 1 mM was not appreciable (Figure 2.11, insert Crystal violet staining and Table 2.5). While both these assays report the same qualitative effect and trend, there are differences in % growth values for individual concentrations of NAC. The MTT assay consistently indicated less cell culture growth than crystal violet staining. The reason for this difference likely reflects mechanistic differences between these two assays: while MTT quantifies cells based on their metabolic activity [35], crystal violet staining estimates the number of cells based on total cell protein and DNA content [67]. Since the activity of mitochondrial succinate dehydrogenase, which is primarily responsible for reduction of MTT [68], might be modulated by NAC treatment, we believe that crystal violet staining is a more objective measure of growth inhibition by NAC than the MTT assay. In contrast, the results of TOX-8 assays performed in a homogeneous format suggest that NAC at concentrations 1-15 mM significantly stimulated growth of AsPC-1 cells (Figure 2.11 insert TOX-8 and Table 2.5). However, images of formazan crystals (Figure 2.11a-d) and crystal violet-stained cells (Figure 2.11e-h) support the results obtained by the MTT and the crystal violet assays, indicating that the resazurin-based TOX-8 assay failed to demonstrate the NAC inhibitory effects at 5 mM and 10 mM and falsely suggested that NAC stimulated proliferation of AsPC-1 cells at all examined concentrations.
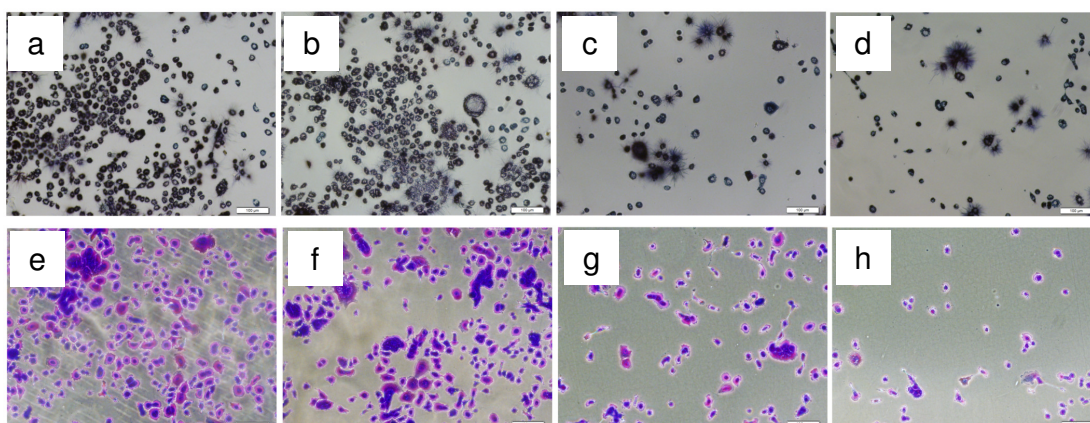
Figure 2.11: Effect of NAC on AsPC-1 cells determined by MTT assay, crystal violet staining and resazurin-based TOX-8 assay. c(NAC)–concentration of N-acetyl-L-cysteine in mM; % growth - amount of cells relative to untreated control; a-d – representative microscopic fields for MTT assay (a – untreated control; b – 5 µM NAC; c – 10 µM NAC; d – 15 µM NAC); e-h – representative microscopic fields for crystal violet staining (e – untreated control; f – 5 µM NAC; g – 10 µM NAC; h – 15 µM NAC); scale bar = 100 µm. Error bars: SEM

Table 2.5: Effect of NAC on the growth of AsPC-1 cells reported by MTT assay, crystal violet staining and TOX-8 assay. Results presented as % of blank corrected signal of treated cells relative to untreated control. *P*-value: two-tailed Student's t-test; N=4.

	MTT		Crystal violet staining		TOX-8	
	% growth±SD	**p-val**	**% growth±SD**	**p-val**	**% growth±SD**	**p-val**
1 mM	101.2±12.0	0.8415	80.6±2.6	3.2e-4	145.0±23.6	4.2e-5
10 mM	49.9±5.0	5.1e-5	25.8±5.3	2.4e-5	128.1±21.6	4.9e-13
15 mM	21.9±3.0	2.8e-6	11.8±2.6	1.4e-6	151.9±45.5	1.0e-13

2.4.5 *NAC at concentrations up to 15 mM does not induce apoptosis in AsPC-1 cells treated for 24 and 48 hrs*

A significant decrease in AsPC-1 cell culture growth upon treatment with NAC may be a consequence of treatment-induced cell cycle arrest or cell death. Compared to untreated AsPC-1 cells, cells treated with 5-15 mM NAC for 24 hours do not display reduced

57

fluorescence after TMRE staining indicating that NAC did not induce mitochondrial membrane depolarization and apoptosis under these conditions, while the CCCP (positive control) significantly decreased TMRE-associated fluorescence of AsPC-1 cells (Figure 2.12 and Figure S1 of [51]).
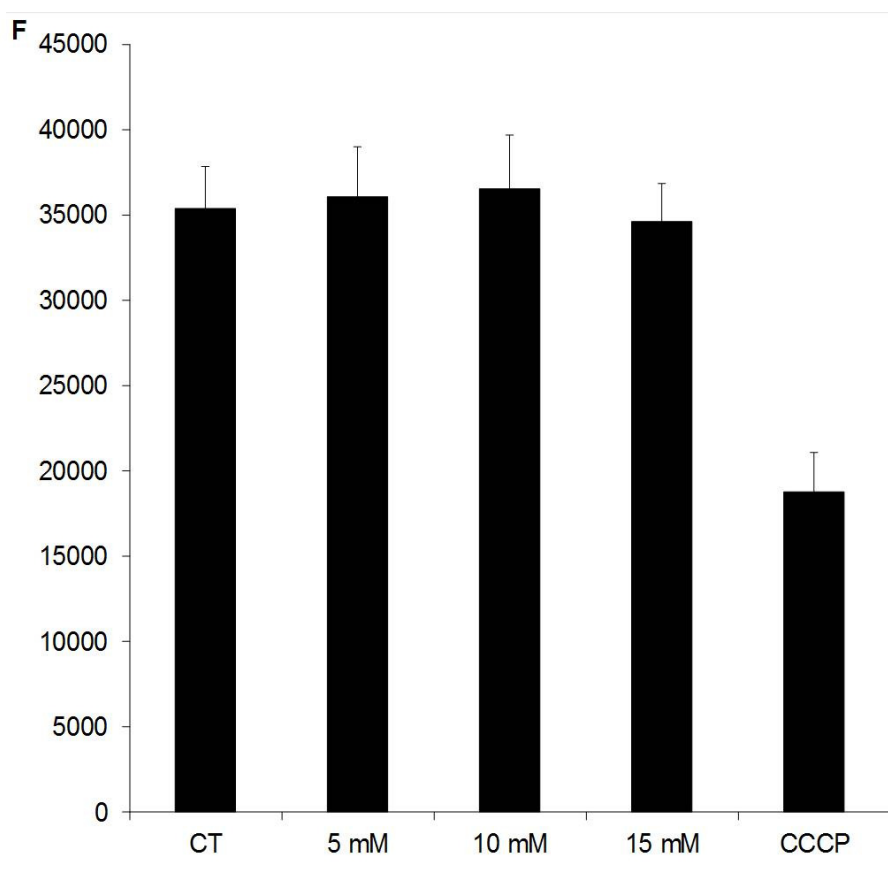
Figure 2.12: Detection of apoptosis by TMRE staining. F-TMRE fluorescence; horizontal axis - concentration of NAC [mM]; CT: untreated cells; CCCP: mitochondrial membrane potential disruptor (positive control). p-value for difference among all data points (ANOVA) = 0.0006; differences between CT and NAC treated cells were not significant (p>0.05); difference between CT and CCCP was significant (Tukey post-hoc test).

Similarly, the FACS experiment does not show a significant increase in a population of cells with externalization of PS (a hallmark of apoptosis) after 24 h and 48 h (Figure 4 of [51]) treatment with 15 mM NAC. As a result, the observed decrease in AsPC-1 culture growth upon NAC treatment is not a consequence of cell death by apoptosis.

2.4.6 *NAC induces cell cycle arrest and cellular senescence in AsPC-1 treated cells*

Since inhibition of the growth of AsPC-1 culture by NAC could not be attributed to apoptosis, we performed an analysis of the distribution of AsPC-1 cells in various phases of the cell cycle upon treatment with 5mM, 10 mM and 15 mM NAC for 48 hours and compared it to the cell cycle distribution of untreated cells. DNA content histograms were fitted with the Watson model implemented in FlowJo 7.6 software (see representative DNA content histograms in Figure S2 of [51]) and the proportion of cells in individual phases of the cell cycle are presented in Figure 2.13. The results indicate a monotonous increase in the proportion of cells in the G1 phase and a decrease in the proportion of G2/M and S phases with an increasing concentration of NAC. The percentage of AsPC-1 cells was statistically significantly higher in the G1 phase and lower in S and G2/M phases after treatment with 15 mM NAC. The statistically significantly higher proportion of cells in G1 phase was also found in cells treated with lower concentrations of NAC (5 mM and 10 mM; Figure 2.13). These results indicate that treatment with NAC under these conditions arrests cells in the G1 phase of the cell cycle. Percentages of cells in the sub-G1 population that corresponds to apoptosis, are small and comparable for all treatments, which is consistent with the conclusion that the observed decrease in AsPC-1 culture growth upon NAC treatment is not a consequence of cell death by apoptosis.
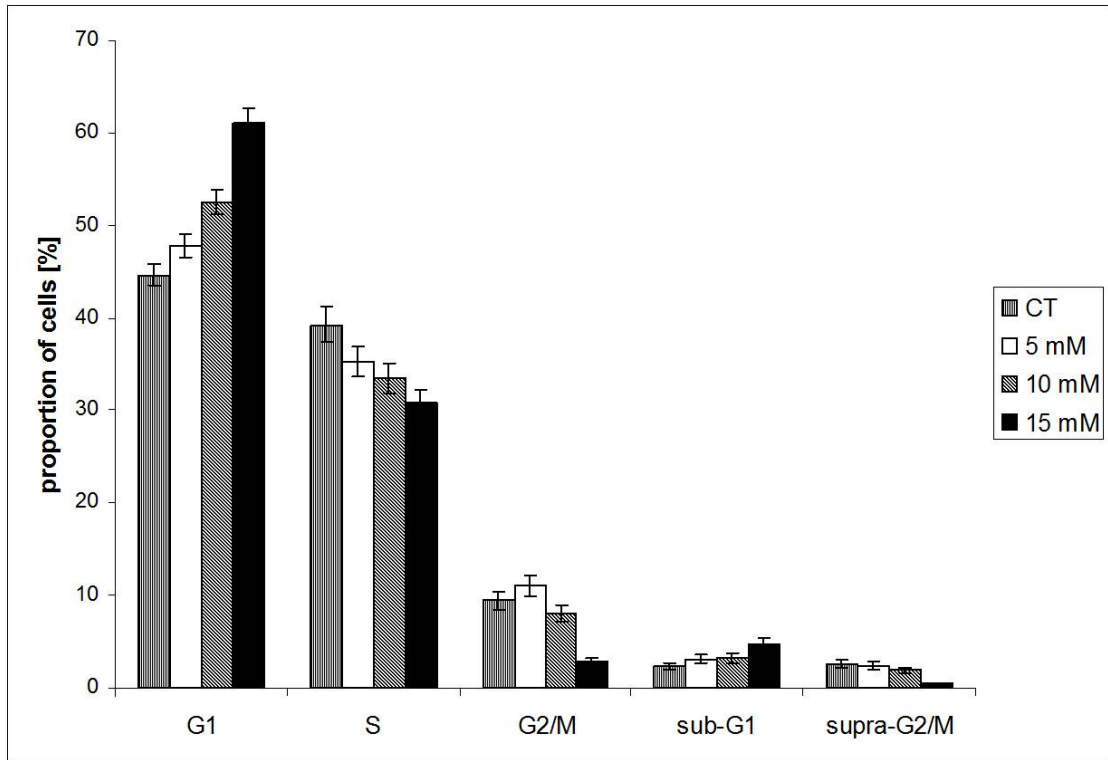
Figure 2.13: Cell cycle analysis by FACS based on DNA content. Presented are proportions of cells in G0/G1, S, G2/M phases of the cell cycle, as well as sub-G1 and supra-G2/M fractions in untreated cells (CT) and cells treated with various concentrations of NAC for 48 hours. Error bars: SEM. Statistical significance of differences between proportion of untreated and NAC-treated cells in individual phases of cell cycle was tested by Holm's multiplicity adjusted t-test and depicted as * ($p<0.05$) and ** ($p<0.01$).

Cellular senescence is a status of permanent growth arrest with a failure to enter the S phase in response to mitogenic stimuli. Cellular senescence can be triggered by telomere shortening (replicative senescence) or by cellular stress induced by ionizing radiation, DNA-damaging drugs, and by activation of oncogenes such as RAS and RAF (stress-induced senescence) [69]. Since NAC inhibited the growth of AsPC-1 cell cultures without inducing apoptosis within the first 48 hours, we hypothesized that this growth inhibitory effect could have been a consequence of NAC-induced cellular senescence, NAC-induced cell quiescence or NAC-induced terminal differentiation of AsPC-1 cells.

The FACS experiment data showed significantly higher activity of senescence-associated β-galactosidase (two-tailed Student's t-test p-value: 0.0258) in AsPC-1 cells treated with 15 mM NAC for 48 hours (mean fluorescent intensity±SD: 433±22.63) relative to untreated cells (321±12.73) that is consistent with cellular senescence and permanent growth arrest in NAC-treated cells as shown in Figure 2.14.
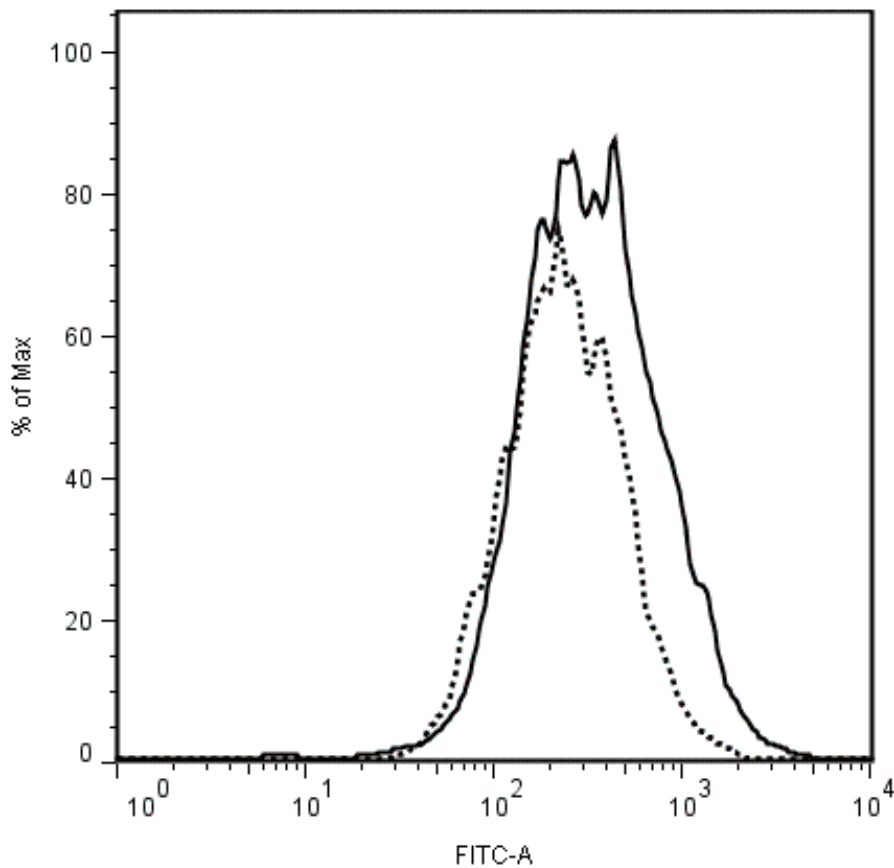
Figure 2.14: Senescence determined through β-galactosidase activity. Dotted line: untreated cells; solid line: cells treated with 15 mM NAC for 48 hours. Fluorescence intensity representing the activity of β-galactosidase was collected in FITC-A channel.

2.4.7 *Reduced in vitro invasion is accompanied with increased cell stiffness in pancreatic cancer AsPC-1 cell*

The *in vitro* invasion through basement membrane extract (BME) was tested for AsPC-1 cells with and without NAC treatment, with the result indicating a statistically highly significant decrease of invasive capability in AsPC-1 cells treated with 15 mM NAC for 24 hours. On average, treatment with NAC decreased the number of cells invading through BME by 97%, as shown in Figure 2.15.
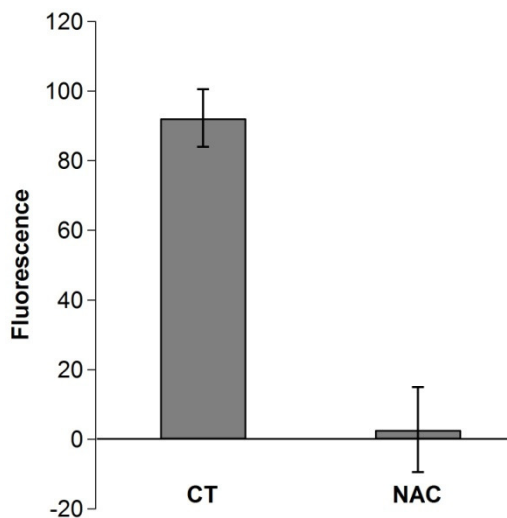
Figure 2.15: *In vitro* cell invasion assay. Untreated cells (CT) and cells treated with 15 mM NAC (NAC) were left to migrate through the basement membrane extract barrier for 24 hours and quantified by fluorescence after Calcein AM staining. Error bars: SEM (N=4); $p=6.72\times10^{-5}$.

To mechanical compliance of single cells as characterized by Young's modulus was also measured by AFM for AsPC-1 cells treated with 15 mM NAC and compared with untreated control cells. The results of 27 treated and 20 control cells, presented as mean ± SEM in Figure 2.16, demonstrate a significant increase in stiffness in NAC-treated

relative to untreated AsPC-1 cells. Since cell stiffness inversely correlates with invasiveness, the observed increase in stiffness of NAC-treated cells is consistent with the decreased *in vitro* invasive capability of these cells, and strongly implies that the observed decrease in invasiveness of NAC-treated cells is not an artifact resulting from inhibition of cell proliferation during the *in vitro* invasion assay.
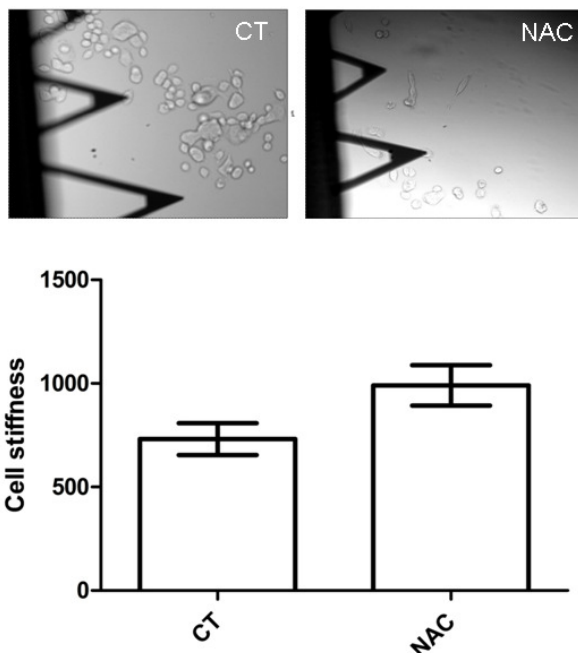
Figure 2.16: Stiffness of AsPC-1 cells increased upon treatment with NAC. Stiffness (Young's modulus) of individual untreated cells (CT) and cells treated with 15 mM NAC for 72 hours (NAC) was determined by AFM

AsPC-1 cells treated with NAC display decreased invasiveness and increased cellular stiffness compared to the untreated group, suggesting that the correlation not only exists for different cell lines of the ovarian cancer as we showed before, but also holds valid when metastatic potential of cancer is artificially modified via chemical methods, at least

in AsPC-1 cell line. The results is consistent with previous reported study on ovarian cancer cells [58], where blebbistatin promotes invasiveness and reduces stiffness simultaneously in ovarian cancer cell line IGROV.

2.4.8 *NAC induces changes in gene expression in AsPC-1 cells that are consistent with mesenchymal-to-epithelial transition (MET), repression of MYC and its target and inhibition of hedgehog (HH) signaling*

qPCR experiments were performed to determine early (8 hours) and late (24 hours) changes in gene expression of several known cancer related genes between cells treated with 15 mM NAC and untreated control cells. We found that CDH1 (E-cadherin), CDKN1A (p21), CDKN1C (p57), and CDKN2A (p16) (up-regulated in treated cells) and CDH2 (N-cadherin), MYC (c-Myc), SHH (sonic hedgehog), TERT (telomerase reverse transcriptase), and TGFBR2 (transforming growth factor, beta receptor II (down-regulated in NAC-treated cells) were significantly differentially expressed between NAC-treated and control cells at, at least, one time point (Figure 2.17). Up-regulation of the epithelial marker CDH1 in parallel with down-regulation of the mesenchymal markers CDH2 and TGFBR2 strongly suggest an induction of mesenchymal-to-epithelial transition of AsPC-1 cells [70, 71].
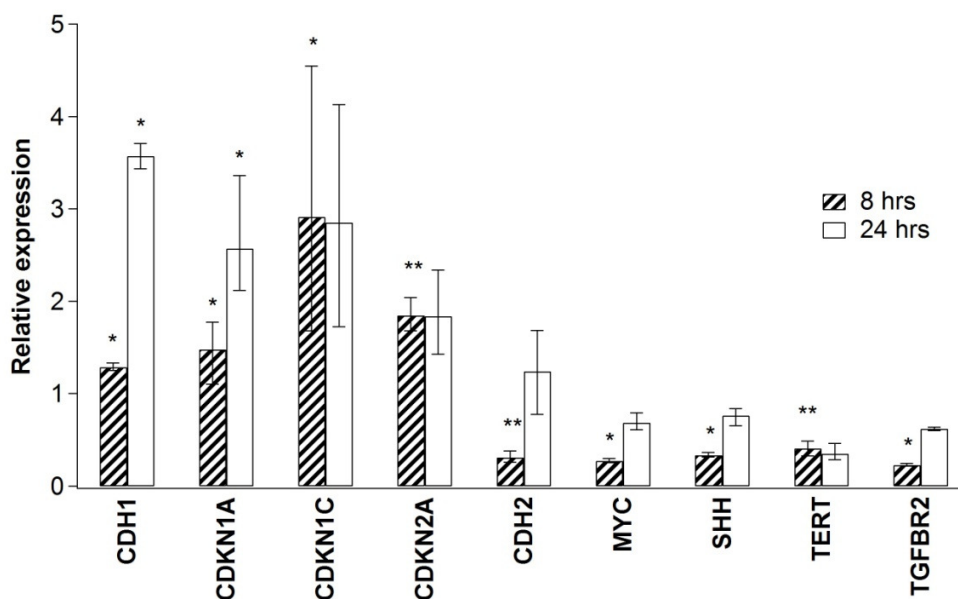
Figure 2.17: Gene expression determined by qPCR. Relative expression between NAC-treated and untreated AsPC-1 cells. Cells were treated for 8 hours or 24 hours with 15 mM NAC. Error bars: SEM. *p*-values for significance of differences between RE values and 1 were determined by randomization test and depicted as follows: *: $0.01 \leq p < 0.05$; **: $p < 0.01$

Since ectopic overexpression of c-Myc in an immortalized mammary epithelial cell line induced epithelial-to-mesenchymal transition (EMT) through inhibition of GSK3B followed by down-regulation of CDH1 and up-regulation of CDH2 [72], it is not surprising that we observed that treatment of AsPC-1 cells with NAC induced changes consistent with mesenchymal-to-epithelial transition (MET) in parallel with down-regulation of MYC. Several lines of evidence suggest a crucial role of EMT in cancer progression and the loss of E-cadherin (CDH1) represents a hallmark of this process [73-75]. Furthermore, CDH1 serves as a suppressor of tumor growth and tumor invasion in animal models of breast cancer [76]. Thus, our observation of up-regulation of CDH1 in NAC-treated AsPC-1 cells is consistent with the decreased invasive capability of these cells. The concomitant down-regulation of CDH2, a marker of EMT is further evidence

65

of a MET in NAC-treated AsPC-1 cells. Moreover, treatment of AsPC-1 cells with NAC results in down-regulation of TGFBR2 and SHH that was also observed in experimentally induced MET in a rat adenocarcinoma model [77].

The previously reported finding that SHH, a secreted hedgehog ligand, is abnormally expressed in pancreatic adenocarcinomas suggests that the hedgehog (HH) pathway may play a critical role early in pancreatic cancer development and pancreatic cancer cell proliferation [78]. Interestingly, SHH secreted by pancreatic cancer cells has been associated with high HH pathway activity predominantly in pancreatic cancer stroma that in turn supplies the tumor with growth-promoting factors [79]. Since the HH signaling pathway has been previously implicated in pancreatic cancer stem cell renewal and chemoresistance [80], down-regulation of SHH may be an important component of the pancreatic cancer inhibitory effect of NAC. Similar to our results with NAC, inhibition of HH signaling in pancreatic cancer cells by cyclopamine has been previously reported to result in down-regulation of CDH1 and a remarkable reduction of *in vitro* invasive capability [81].

Another cancer stem cell relevant molecule is CD44 - a transmembrane glycoprotein that was previously reported to be a marker of cancer stem cells for various cancers [82], including pancreatic cancer [83-85]. Since its expression is associated with drug resistance and clonogenicity of cancer cells *in vitro*, as well as tumor grade and poor survival in clinical settings [86], and since the AsPC-1 cell line is CD44-positive [87], we were interested to test whether NAC down-regulates expression of CD44. However, the results of our FACS experiment show no difference in CD44-expression of NAC-treated and untreated AsPC-1 cells (Figure S4 of [51]).

66

The significant role of epithelial to mesenchymal transition (EMT) in cancer metastasis has been well known [88-91]. The results shown here, together with other studies [92-94], demonstrated that EMT accompanies with increase in migration/invasion, and MET with reduction in migration/invasion. Morphology, stiffness and invasiveness as phenotypic properties of cells, are all modulated by cellular structure, which is in turn dictated by the genetics and gene expression profiles. The correlation between stiffness and invasiveness, and the role of cell morphology in metastasis, make us to postulate that there also exists a relationship between stiffness and cell morphology, as both are modulated by cytoskeleton at the cellular level and genetics and epigenetics as the molecular mechanism.

2.5   Summary and conclusion

Our analysis of non-malignant IOSE and four ovarian cancer cell lines indicate that cancer cells exhibit a lower mean stiffness relative to non-malignant precursor cells. Interestingly, we also find that the increase in invasive and migratory capacity associated with HEY A8 cells relative to HEY cells is also correlated with a significant reduction in cell stiffness. Comparative gene expression analysis of HEY A8 and HEY cells indicates that the molecular basis of the reduction in stiffness between these cells is reflective of extensive molecular changes including changes in actin cytoskeleton remodeling pathways. Protein expression differences were found in the actin monomer binding proteins overexpressed in HEY A8 relative to HEY, tension generating proteins down-regulated in HEY A8 relative to HEY, and pathway network remodeling of the RhoA/Rho kinase pathway and TGF, WNT and cytoskeletal remodeling pathway. Microscopic analyses of actin cytoskeleton in ovarian cancer and control cells are

consistent with this hypothesis. The correlation between stiffness and metastasis also exists in pancreatic cancer cell line AsPC-1 upon treatment with NAC, gene expression profile also revealed the structural change of single cells of AsPC-1 upon treatment with NAC. The results shown here support cell stiffness as a biomarker of metastatic potential in these two distinct cancer types and the stiffness-invasiveness correlation might be extendable to other types of cancer.

Since our measurements are conducted with cancer cell lines, further studies will be needed to see if similar results are found in the case of patient-derived cells. Establishing the relative metastatic potential of cancer cells is an important factor in the design of optimal strategies in the personalized treatment of cancer [95]. Currently, extensive molecular profiling is required to estimate the metastatic potential of cancer cells [96]. Collectively, our results indicate that mechanical stiffness may be a useful biomarker in the development of accurate, non-invasive clinical methods to evaluate the relative metastatic potential of ovarian and perhaps other types of cancer cells. Stiffness may be particularly important as a biomarker with the development of rapid biomechanical assaying techniques [97, 98].

2.6 References

1. Friedman, E., et al., *Actin Cytoskeletal Organization Loss in the Benign-to-Malignant Tumor Transition in Cultured Human Colonic Epithelial Cells.* Cancer Research, 1984. **44**(7): p. 3040-3050.

2. Katsantonis, J., et al., *Differences in the G/total actin ratio and microfilament stability between normal and malignant human keratinocytes.* Cell Biochemistry and Function, 1994. **12**(4): p. 267-274.

3. Fuhrmann, A., et al., *AFM stiffness nanotomography of normal, metaplastic and dysplastic human esophageal cells.* Physical Biology, 2011. **8**(1): p. 015007.

4.   Guck, J., et al., *Optical Deformability as an Inherent Cell Marker for Testing Malignant Transformation and Metastatic Competence.* Biophysical Journal, 2005. **88**(5): p. 3689-3698.

5.   Moustakas, A. and C. Stournaras, *Regulation of actin organisation by TGF-beta in H-ras-transformed fibroblasts.* Journal of Cell Science, 1999. **112**(8): p. 1169-1179.

6.   Cross, S.E., et al., *Nanomechanical analysis of cells from cancer patients.* Nat Nano, 2007. **2**(12): p. 780-783.

7.   Yamazaki, D., S. Kurisu, and T. Takenawa, *Regulation of cancer cell motility through actin reorganization.* Cancer Science, 2005. **96**(7): p. 379-386.

8.   Suresh, S., *Nanomedicine: Elastic clues in cancer detection.* Nat Nano, 2007. **2**(12): p. 748-749.

9.   Suresh, S., *Biomechanics and biophysics of cancer cells.* Acta Materialia, 2007. **55**(12): p. 3989-4014.

10.   Elson, E.L., *Cellular Mechanics as an Indicator of Cytoskeletal Structure and Function.* Annual Review of Biophysics and Biophysical Chemistry, 1988. **17**(1): p. 397-430.

11.   Lekka, M., et al., *Elasticity of normal and cancerous human bladder cells studied by scanning force microscopy.* European Biophysics Journal, 1999. **28**(4): p. 312-316.

12.   Rao, J.Y. and N. Li, *Microfilament Actin Remodeling as a Potential Target for Cancer Drug Development.* Current Cancer Drug Targets, 2004. **4**(4): p. 345-354.

13.   Williamson, J., et al., *Microrheologic investigation of erythrocyte deformability in diabetes mellitus.* Blood, 1985. **65**(2): p. 283-288.

14.   Lekka, M. and P. Laidler, *Applicability of AFM in cancer detection.* Nat Nano, 2009. **4**(2): p. 72-72.

15. Lee, G.Y.H. and C.T. Lim, *Biomechanics approaches to studying human diseases.* Trends in Biotechnology, 2007. **25**(3): p. 111-118.

16. Suresh, S., et al., *Connections between single-cell biomechanics and human disease states: gastrointestinal cancer and malaria.* Acta Biomaterialia, 2005. **1**(1): p. 15-30.

17. Hou, H., et al., *Deformability study of breast cancer cells using microfluidics.* Biomedical Microdevices, 2009. **11**(3): p. 557-564.

18. McKnight, A.L., et al., *MR Elastography of Breast Cancer: Preliminary Results.* American Journal of Roentgenology, 2002. **178**(6): p. 1411-1417.

19. Bercoff, J., et al., *In vivo breast tumor detection using transient elastography.* Ultrasound in Medicine & Biology, 2003. **29**(10): p. 1387-1396.

20. Jemal, A., et al., *Cancer Statistics, 2010.* CA: A Cancer Journal for Clinicians, 2010. **60**(5): p. 277-300.

21. Bhoola, S. and W.J. Hoskins, *Diagnosis and Management of Epithelial Ovarian Cancer.* Obstetrics & Gynecology, 2006. **107**(6): p. 1399-1410.

22. Howlader, N., et al. *SEER Cancer Statistics Review*. 1975-2009(Vintage 2009 Publication). Bethesda, MD: National Canceer Institute.

23. Li, J., M.G. Wientjes, and J.S. Au, *Pancreatic Cancer: Pathobiology, Treatment Options, and Drug Delivery.* The AAPS Journal, 2010. **12**(2): p. 223-232.

24. Chen, W.H., et al., *Human pancreatic adenocarcinoma: In vitro and in vivo morphology of a new tumor line established from ascites.* In Vitro Cellular & Developmental Biology - Plant, 1982. **18**(1): p. 24-34.

25. Supabphol, A., et al., *N-acetylcysteine inhibits proliferation, adhesion, migration and invasion of human bladder cancer cells.* Journal of the Medical Association of Thailand, 2009. **92**(9): p. 1171-1177.

26. Vanisree, A.J. and C.S. Shyamaladevi, *The effect of N-acetylcysteine in combination with vitamin C on the activity of ornithine decarboxylase of lung carcinoma cells — In vitro.* Life Sciences, 2006. **79**(7): p. 654-659.

27. Yan, C.Y.I., G. Ferrari, and L.A. Greene, *N-Acetylcysteine-promoted Survival of PC12 Cells Is Glutathione-independent but Transcription-dependent.* Journal of Biological Chemistry, 1995. **270**(45): p. 26827-26832.

28. Jian, J.L., et al., *N-acetyl cysteine inhibits human signet ring cell gastric cancer cell line (SJ-89) cell growth by inducing apoptosis and DNA synthesis arrest.* Eur J Gastroenterol Hepatol, 2007. **19**(9): p. 769-774.

29. Lee, Y.-J., et al., *Suppression of human prostate cancer PC-3 cell growth by N-acetylcysteine involves over-expression of Cyr61.* Toxicology in Vitro, 2011. **25**(1): p. 199-205.

30. Kusano, C., et al., *N-acetyl cysteine inhibits cell cycle progression in pancreatic carcinoma cells.* Human cell, 2000. **13**(4): p. 213-220.

31. Kawakami, S., et al., *Inhibitory effect of N-acetylcysteine on invasion and MMP-9 production of T24 human bladder cancer cells.* Anticancer research, 2001. **21**(1A): p. 213-219.

32. Albini, A., et al., *Inhibition of invasion, gelatinase activity, tumor take and metastasis of malignant cells by N-acetylcysteine.* International Journal of Cancer, 1995. **61**(1): p. 121-129.

33. Agarwal, A., et al., *N-Acetyl-Cysteine Promotes Angiostatin Production and Vascular Collapse in an Orthotopic Model of Breast Cancer.* The American Journal of Pathology, 2004. **164**(5): p. 1683-1696.

34. De Flora, S., et al., *Mechanisms of N-acetylcysteine in the prevention of DNA damage and cancer, with special reference to smoking-related end-points.* Carcinogenesis, 2001. **22**(7): p. 999-1013.

35. O'Brien, J., et al., *Investigation of the Alamar Blue (resazurin) fluorescent dye for the assessment of mammalian cell cytotoxicity.* European Journal of Biochemistry, 2000. **267**(17): p. 5421-5426.

36. Vistica, D.T., et al., *Tetrazolium-based Assays for Cellular Viability: A Critical Examination of Selected Parameters Affecting Formazan Production.* Cancer Research, 1991. **51**(10): p. 2515-2520.

37. Jeng, Y.-J.J. and C.S. Watson, *Proliferative and anti-proliferative effects of dietary levels of phytoestrogens in rat pituitary GH3/B6/F10 cells - the involvement of rapidly activated kinases and caspases.* BMC Cancer, 2009. **9**: p. 334.

38. Jayaraman, S., *Flow cytometric determination of mitochondrial membrane potential changes during apoptosis of T lymphocytic and pancreatic beta cell lines: Comparison of tetramethylrhodamineethylester (TMRE), chloromethyl-X-rosamine (H2-CMX-Ros) and MitoTracker Red 580 (MTR580).* Journal of Immunological Methods, 2005. **306**(1–2): p. 68-79.

39. Reutelingsperger, C.P.M. and W.L. van Heerde, *Annexin V, the regulator of phosphatidylserine-catalyzed inflammation and coagulation during apoptosis.* Cellular and Molecular Life Sciences CMLS, 1997. **53**(6): p. 527-532.

40. Mezencev, R., et al., *Camalexin induces apoptosis in T-leukemia Jurkat cells by increased concentration of reactive oxygen species and activation of caspase-8 and caspase-9.* Journal of Natural Medicines, 2011. **65**(3-4): p. 488-499.

41. Dimri, G.P., et al., *A biomarker that identifies senescent human cells in culture and in aging skin in vivo.* Proceedings of the National Academy of Sciences, 1995. **92**(20): p. 9363-9367.

42. Bao, G. and S. Suresh, *Cell and molecular mechanics of biological materials.* Nat Mater, 2003. **2**(11): p. 715-725.

43. IyerS, et al., *Atomic force microscopy detects differences in the surface brush of normal and cancerous cells.* Nat Nano, 2009. **4**(6): p. 389-393.

44. Hutter, J.L. and J. Bechhoefer, *Calibration of atomic-force microscope tips.* Review of Scientific Instruments, 1993. **64**(7): p. 1868-1873.

45. Johnson, K.L., *Contact mechanics.* 1985, Cambridge, UK: Cambridge university press.

46.   Xu, W., N. Chahine, and T. Sulchek, *Extreme Hardening of PDMS Thin Films Due to High Compressive Strain and Confined Thickness.* Langmuir, 2011. **27**(13): p. 8470-8477.

47.   Tusher, V.G., R. Tibshirani, and G. Chu, *Significance analysis of microarrays applied to the ionizing radiation response.* Proceedings of the National Academy of Sciences, 2001. **98**(9): p. 5116-5121.

48.   Shi, W., et al., *Functional analysis of multiple genomic signatures demonstrates that classification algorithms choose phenotype-related genes.* Pharmacogenomics J, 2010. **10**(4): p. 310-323.

49.   Vellaichamy, A., et al., *"Topological Significance" Analysis of Gene Expression and Proteomic Profiles from Prostate Cancer Cells Reveals Key Mechanisms of Androgen Response.* PLoS ONE, 2010. **5**(6): p. e10936.

50.   Dezső, Z., et al., *Identifying disease-specific genes based on their topological significance in protein networks.* BMC Systems Biolog, 2009. **3**: p. 36.

51.   Mezencev, R., et al., *Molecular analysis of the inhibitory effect of N-acetyl-L-cysteine on the proliferation and invasiveness of pancreatic cancer cells.* Anticancer Drugs, 2013. **24**(5): p. 504-518.

52.   Pfaffl, M.W., G.W. Horgan, and L. Dempfle, *Relative expression software tool (REST©) for group-wise comparison and statistical analysis of relative expression results in real-time PCR.* Nucleic Acids Research, 2002. **30**(9): p. e36.

53.   Team, R.D.C., *R: A language and environment for statistical computing.* 2009, Vienna, Austria: R Foundation for Statistical Computing. 409.

54.   Marquez, J.P., *Fourier analysis and automated measurement of cell and fiber angular orientation distributions.* International Journal of Solids and Structures, 2006. **43**(21): p. 6413-6423.

55.   Mills, G.B., et al., *Ascitic fluid from human ovarian cancer patients contains growth factors necessary for intraperitoneal growth of human ovarian adenocarcinoma cells.* The Journal of Clinical Investigation, 1990. **86**(3): p. 851-855.

56.   Xu, W., et al., *Cell Stiffness Is a Biomarker of the Metastatic Potential of Ovarian Cancer Cells.* PLoS ONE, 2012. **7**(10): p. e46609.

57.   Sokolov, I., *Atomic force microscopy in cancer cell research*, in *Cancer nanotechnology-nanomaterials for cancer diagnosis and therapy*, H. Singh and T. Webster, Editors. 2007, American Scientific Publishers: California, USA.

58.   Swaminathan, V., et al., *Mechanical Stiffness Grades Metastatic Potential in Patient Tumor Cells and in Cancer Cell Lines.* Cancer Research, 2011. **71**(15): p. 5075-5080.

59.   Palmgren, S., M. Vartiainen, and P. Lappalainen, *Twinfilin, a molecular mailman for actin monomers.* Journal of Cell Science, 2002. **115**(5): p. 881-886.

60.   Hotulainen, P., et al., *Actin-depolymerizing Factor and Cofilin-1 Play Overlapping Roles in Promoting Rapid F-Actin Depolymerization in Mammalian Nonmuscle Cells.* Molecular Biology of the Cell, 2005. **16**(2): p. 649-664.

61.   Moseley, J.B., et al., *Twinfilin is an actin-filament-severing protein and promotes rapid turnover of actin structures in vivo.* Journal of Cell Science, 2006. **119**(8): p. 1547-1557.

62.   An, S.S., et al., *Stiffness changes in cultured airway smooth muscle cells.* American Journal of Physiology - Cell Physiology, 2002. **283**(3): p. C792-C801.

63.   Schäfer, A. and M. Radmacher, *Influence of myosin II activity on stiffness of fibroblast cells.* Acta Biomaterialia, 2005. **1**(3): p. 273-280.

64.   Mott, A., et al., *Modulation of host cell mechanics by Trypanosoma cruzi.* Journal of Cellular Physiology, 2009. **218**(2): p. 315-322.

65.   Ridley, A.J. and A. Hall, *Signal transduction pathways regulating Rho-mediated stress fibre formation: requirement for a tyrosine kinase.* The EMBO Journal, 1994. **13**(11): p. 2600-2610.

66.   Rotsch, C. and M. Radmacher, *Drug-Induced Changes of Cytoskeletal Structure and Mechanics in Fibroblasts: An Atomic Force Microscopy Study.* Biophysical Journal, 2000. **78**(1): p. 520-535.

67. Lu, W.L., L. McCallum, and A.E. Irvine, *A rapid and sensitive method for measuring cell adhesion.* J. Cell Commun. Signal., 2009. **3**: p. 147-149.

68. Kaneko, I., et al., *Suppression of Mitochondrial Succinate Dehydrogenase, a Primary Target of β-Amyloid, and Its Derivative Racemized at Ser Residue.* Journal of Neurochemistry, 1995. **65**(6): p. 2585-2593.

69. Qanungo, S., M. Wang, and A.-L. Nieminen, *N-Acetyl-l-cysteine Enhances Apoptosis through Inhibition of Nuclear Factor-κB in Hypoxic Murine Embryonic Fibroblasts.* Journal of Biological Chemistry, 2004. **279**(48): p. 50455-50464.

70. Willis, B.C. and Z. Borok, *TGF-β-induced EMT: mechanisms and implications for fibrotic lung disease.* American Journal of Physiology - Lung Cellular and Molecular Physiology, 2007. **293**(3): p. L525-L534.

71. Shimojo, Y., et al., *Attenuation of reactive oxygen species by antioxidants suppresses hypoxia-induced epithelial-mesenchymal transition and metastasis of pancreatic cancer cells.* Clinical & Experimental Metastasis, 2013. **30**(2): p. 143-154.

72. Cho, K.B., et al., *Overexpression of c-myc induces epithelial mesenchymal transition in mammary epithelial cells.* Cancer Letters, 2010. **293**(2): p. 230-239.

73. Kang, Y. and J. Massagué, *Epithelial-Mesenchymal Transitions: Twist in Development and Metastasis.* Cell, 2004. **118**(3): p. 277-279.

74. Hazan, R.B., et al., *Cadherin Switch in Tumor Progression.* Annals of the New York Academy of Sciences, 2004. **1014**(1): p. 155-163.

75. Thompson, E.W. and D.F. Newgreen, *Carcinoma Invasion and Metastasis: A Role for Epithelial-Mesenchymal Transition?* Cancer Research, 2005. **65**(14): p. 5991-5995.

76. Cowin, P., T.M. Rowlands, and S.J. Hatsell, *Cadherins and catenins in breast cancer.* Current Opinion in Cell Biology, 2005. **17**(5): p. 499-508.

77. Moen, I., et al., *Hyperoxic Treatment Induces Mesenchymal-to-Epithelial Transition in a Rat Adenocarcinoma Model.* PLoS ONE, 2009. **4**(7): p. e6381.

78. Thayer, S.P., et al., *Hedgehog is an early and late mediator of pancreatic cancer tumorigenesis.* Nature, 2003. **425**(6960): p. 851-856.

79. Yauch, R.L., et al., *A paracrine requirement for hedgehog signalling in cancer.* Nature, 2008. **455**(7211): p. 406-410.

80. Huang, F.-T., et al., *Inhibition of hedgehog signaling depresses self-renewal of pancreatic cancer stem cells and reverses chemoresistance.* International Journal of Oncology, 2012. **41**(5): p. 1707-1714.

81. Feldmann, G., et al., *Blockade of Hedgehog Signaling Inhibits Pancreatic Cancer Invasion and Metastases: A New Paradigm for Combination Therapy in Solid Cancers.* Cancer Research, 2007. **67**(5): p. 2187-2196.

82. Jaggupilli, A. and E. Elkord, *Significance of CD44 and CD24 as cancer stem cell markers: an enduring ambiguity.* Clinical and Developmental Immunology, 2012. **2010**: p. 708036.

83. Li, C., et al., *Identification of Pancreatic Cancer Stem Cells.* Cancer Research, 2007. **67**(3): p. 1030-1037.

84. Lee, C.J., J. Dosch, and D.M. Simeone, *Pancreatic Cancer Stem Cells.* Journal of Clinical Oncology, 2008. **26**(17): p. 2806-2812.

85. Ji, Q., et al., *MicroRNA miR-34 Inhibits Human Pancreatic Cancer Tumor-Initiating Cells.* PLoS ONE, 2009. **4**(8): p. e6816.

86. Hong, S.P., et al., *CD44-positive cells are responsible for gemcitabine resistance in pancreatic cancer cells.* International Journal of Cancer, 2009. **125**(10): p. 2323-2331.

87. Wei HJ, Y.T., Zhu Z, Shi PF, Tian Y, Wang CY, *Expression of CD44, CD24 and ESA in pancreatic adenocarcinoma cell lines varies with local microenvironment.* Hepatobiliary Pancreat Dis Int, 2011. **10**(4): p. 428-434.

88. Tsai, Jeff H., et al., *Spatiotemporal Regulation of Epithelial-Mesenchymal Transition Is Essential for Squamous Cell Carcinoma Metastasis.* Cancer Cell, 2012. **22**(6): p. 725-736.

89.   Iwatsuki, M., et al., *Epithelial–mesenchymal transition in cancer development and its clinical significance.* Cancer Science, 2010. **101**(2): p. 293-299.

90.   Meng, F. and G. Wu, *The rejuvenated scenario of epithelial–mesenchymal transition (EMT) and cancer metastasis.* Cancer and Metastasis Reviews, 2012. **31**(3-4): p. 455-467.

91.   Yilmaz, M. and G. Christofori, *EMT, the cytoskeleton, and cancer cell invasion.* Cancer and Metastasis Reviews, 2009. **28**(1-2): p. 15-33.

92.   Chen, J., et al., *Overexpression of miR-429 induces mesenchymal-to-epithelial transition (MET) in metastatic ovarian cancer cells.* Gynecologic Oncology, 2011. **121**(1): p. 200-205.

93.   Han, S.-Y., et al., *CIIA induces the epithelial–mesenchymal transition and cell invasion.* Biochemical and Biophysical Research Communications, 2009. **387**(3): p. 548-552.

94.   Bao, X.-l., et al., *Wnt3a promotes epithelial-mesenchymal transition, migration, and proliferation of lens epithelial cells.* Molecular Vision, 2012. **18**: p. 1983-1990.

95.   Tian, Q., N.D. Price, and L. Hood, *Systems cancer medicine: towards realization of predictive, preventive, personalized and participatory (P4) medicine.* Journal of Internal Medicine, 2012. **271**(2): p. 111-121.

96.   Sethi, N. and Y. Kang, *Unravelling the complexity of metastasis — molecular understanding and targeted therapies.* Nat Rev Cancer, 2011. **11**(10): p. 735-748.

97.   Rosenbluth, M.J., W.A. Lam, and D.A. Fletcher, *Analyzing cell mechanics in hematologic diseases with microfluidic biophysical flow cytometry.* Lab on a Chip, 2008. **8**(7): p. 1062-1070.

98.   Gossett, D.R., et al., *Hydrodynamic stretching of single cells for large population mechanical phenotyping.* Proceedings of the National Academy of Sciences, 2012.

CHAPTER 3

STIFFNESS OF SINGLE CELLS THROUGH THE CELL CYCLE

3.1   Abstract

Based on our results in chapter 2, the stiffness of ovarian cancer cells is softer than for healthy phenotypes. We also found that healthy cell types with larger mean Young's moduli also display larger variations in stiffness (Figure 2.3a and Table 2.1), whereas softer cells display a narrow variance of stiffness. Among many factors that might contribute to variations among these cell types, we hypothesized that the alterations in cell cycle progression, and the concomitant cytoskeletal rearrangements that occur, may account for these increased variations in stiffness. In this chapter, we study how the stiffness of ovarian cancer cells can change during natural progression in the cell cycle. In this chapter, we labeled the cell cycle progression of ovarian health and cancer cells (IOSE and HEY A8) while simultaneously measuring their mechanical properties. The cell cycle phase was labeled using the fluorescent FUCCI label system. The results show that only IOSE cells at G1 phase are significant stiffer than IOSE cells at other phases and HEY A8 at S, G2/early mitosis, and late mitosis phases. We conclude that the mechanical abnormalities of invasive ovarian cancer cells are primarily manifested through a decreased stiffness of the G1 phase.

3.2   Introduction

The eukaryotic cell cycle consists of a temporal sequence of biological events through which cells grow, divide and reproduce. Cytoskeleton and associated proteins are actively involved in this process through a variety of mechanisms and pathways such as the Rho GTPase family [1, 2]. The role of cytoskeleton in key steps of the cell cycle, including

78

such processes as signal transduction, chromosomal separation, and formation of cleavage furrow during cytokinesis, has been well recognized, as the cytoskeletal structure and morphological changes through the cell cycle are optically observable [3, 4]. The cytoskeleton also affects the progression of cell cycle [5-7], force transmission in response to environment through atcin cytoskeleton is known to alter gene expression profiles [8-10]. Since the cytoskeleton acts as a scaffold for molecular interaction and also provides mechanical support for cellular processes, understanding the mechanics of single cells during the cell cycle will contribute to the resolving the role of cytoskeleton in cell cycle. The particular significance of the cell cycle to cancer is also important to highlight—cell cycle regulation processes awry and the consequent unregulated growth is an import factor contributing to tumorigenesis.

In the eukaryotic cell cycle, the "clock + checkpoint" central control machinery relies on cyclin-CDK complex and its associated proteins [11-15], ensuring the cell growth cycle progresses precisely and accurately. Tumorigenic processes includes mutations in proto-oncogenes or tumor suppressor genes and epigenetic alterations [16-20] which cause a loss of cell cycle regulation [12, 21]. Abnormality in expression and function of Rho GTPases and related pathways is a major factor contributing to tumorigenesis [20, 22], metastasis [23, 24], which all result in cytoskeleton remodeling, observed through fluorescence imaging of unorganized cytoskeleton structure in cancer cells compared to noncancerous cells [25, 26], understanding the mechanics of cancer cell cycle will provide insightful information of cytoskeleton in the progression of cell cycle.

Previous research on cell cycle has focused on the roles of relevant gene expression profiles and pathways in cell cycle regulation and their therapeutic potentials [20, 24, 27,

28]. Cell cycle-dependent biophysical properties have been investigated for some cell types [29-31], particularly the effect of myosin light chain kinase [32] activity, nuclear morphology [33] and cytoplasmic components [3, 6, 34, 35] on the biomechanical evolution through cell cycle. We have measured stiffness distributions of different ovarian cells as described in chapter 2, however, the effect of cell cycle on stiffness still remain elusive. The understanding of how stiffness of healthy and cancer cells varies with cell cycle will improve our ability to use stiffness as a biomarker in ovarian cancer, based on our results in Chapter 2.

Similar cell stiffness measurements have been conducted on bone cells and HL-60 cells [29, 30] showing dependence of single cell stiffness on cell cycle. Different methods were used to determine the cell cycle phases, such as centrifugal elutriation [30, 36, 37], serum starvation [29, 38-42], chemical method [40, 43], cell confluence [40, 44] or DNA content sorting [45]. While these methods provide straightforward methods to separate cells by cell cycle phases, there are serious limitations of these techniques for our studies. Release of cells from serum starvation in cell synchronization [46] does not produce cells reflecting cells during the normal division cycle; serum starvation was also reported to cause DNA damage and changes to the morphology of the cells [47-49], which likely affects cell stiffness. In addition, serum starvation cannot be used to differentiate G2 and mitosis phases from other two. Cell elutriation [30] is not a good choice in our study either, cells in suspension states are different from cells in adherent states, and the time period required for cells to settle down from the suspension to the glass substrate might be enough for cells to move to another phases. Several methods have been used to determine the cell cycle phases and then measure cell stiffness, another issue yet to be

addressed in cell mechanics measurements with atomic force microscopy (AFM) relates to the time from the cells sorted to the actual measurement, during this time period, cells might have moved to a different phase. Measuring stiffness of live cells at each phase through the cell cycle is needed and requires a method different from those we described above.

In this chapter, we aim to understand the modifications to biomechanics during ovarian cancer cell proliferation and natural growth by performing simultaneous measurement of the cell cycle and stiffness measurements. We presented the measurement of single live cell stiffness distribution for each of the cell cycle phases, by combining fluorescent imaging of cell cycle labels and AFM mechanical measurement. We were able to visualize cell cycle in live using a new cell cycle labeling technique, and importantly, we determined that the staining doesn't significantly impact the mechanical properties of the cells. We therefore could measure the single cell stiffness and identify cell cycle phases simultaneously. We tested the stiffness distribution of IOSE and HEY A8 cells at different phases through the cell cycle. The results shown here not only provide meaningful data of mechanical stiffness correlated with cell cycle, but also shed light on the interaction of mechanics and biology of the cell cycle.

3.3   Materials and methods

3.3.1   Sample preparation and labeling of cell cycle

IOSE and HEY A8 cells were cultured in Fluorodish (World Precision Instruments, Sarasota, FL) as described in chapter 2. Prior to the day of cell cycle labeling, cells were plated in a Fluorodish with a glass bottom at an initial density of 10,000-20,000 cells/cm^2,

and then incubated at 37 ˚C overnight. By the time of cell cycle labeling, cells were already settle down and adhere to the glass bottom of the Fluorodish.

To measure stiffness of single cells at different cell cycle phases, we have to identify cell cycle phases of single cells under AFM measurements in a quick and easy way. To this end, cell cycle labeling was implemented using fluorescence ubiquitination cell cycle indicator (FUCCI, from Life Technologies, Carlsbad, CA) so that cells are readily identifiable by a particular band of fluorescence under the FITC/TRITC emission filters. In brief, as cells progress through the cell cycle, ubiquitin-mediated proteolysis is involved in the cell cycle regulation by targeting and degrading proteins associated with the cell cycle [50]. APC and SCF are two examples of E3 ubiquitin ligase proteins [51, 52], and therefore make their substrates Geminin and Cdt1 oscillate biphasically through the cell cycle [51]. Figure 3.1 shows the protein levels of Geminin and Cdt1 through the cell cycle [53]. The basic idea of FUCCI cell cycle labeling is fusing fluorescent proteins into the cell cycle regulators Cdt1 and geminin, by monitoring the red/green fluorescence intensity of the labeled cell, the cell cycle phase of the single cell under measurement is easy to determine.
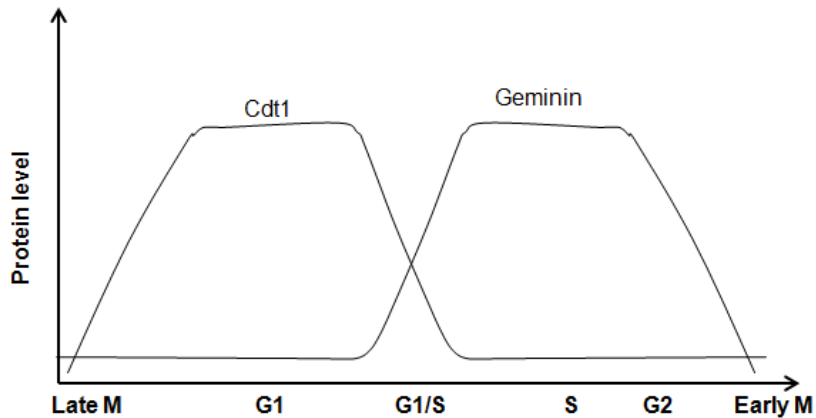
Figure 3.1: Cdt1 and Geminin levels through the cell cycle, adapted from reference [53]

When the plated cells reached around 50% confluency, they were labeled with FUCCI kit following the protocol from the manufacturer. A Premo FUCCI transduction solution was made by mixing 20 µL of Premo-geminin-GFP and 20 µL of Premo Cdt1-RFP with 2 mL of D-PBS without calcium or magnesium. The cell culture media was removed and substituted with FUCCI transduction solution and incubated at room temperature for 2 hours with gentle stirring. When cells were incubated at room temperature, 1X BacMam enhancer working solution was made by diluting the original 1000X BacMam/DMSO stock solution into cell culture media. After 1-2 hours, FUCCI transduction solution was substituted with 1X BacMam enhancer working solution and the cells were incubated in at 37 ˚C for 60-90 minutes. Finally, the BacMam solution was replaced by normal growth media and the cells were incubated at 37 ˚C for over 16 hours prior to the stiffness measurements. The labeling process was conducted in a dark room.

3.3.2 *Cell stiffness measurement and identification of cell cycle phases*

The stiffness measurements of single cells at specific cell cycle phases were made possible by the combination of AFM and an inverted Nikon-Ti microscope, which is

capable of providing bright field and fluorescence functions. The AFM cantilever (Model number: MCST-AUHW, from Bruker) used to indent single cells has a nominal spring constant of 0.03 N/m. A plain silica microsphere of diameter 4.74 μm was attached to the cantilever tip to simplify the contact geometry and minimize lateral strain during indentation. Prior to cell stiffness measurements, the cantilever was calibrated on the glass bottom of the Fluorodish using the thermal vibration method [54] and the spring constant was determined by fitting the resultant thermal spectrum with Lorentzian function. Measurements were conducted in cell culture media with cells immobilized on glass bottom of the Fluorodish, the experiments were implemented at room temperature in absence of room light. Single cells were measured to eliminate possible effect of cell contacting on stiffness.

Following the same experiment set up as we used in chapter 2, the measurements took place in cell culture media environment and cells adhered to glass bottom of the Fluorodish. First, the cell cycle phase was determined by fluorescence as cells show different sets of color under FITC/TRITC filter; then fluorescence was turned off and cell stiffness measured by AFM under bright field as described in chapter 2. Force-indentation curves were collected when cells are indented by AFM probe and analyzed using Hertz contact model [55, 56] to determine Young's modulus. The measurement using AFM and fluorescence microscopy is sketched in Figure 3.2.
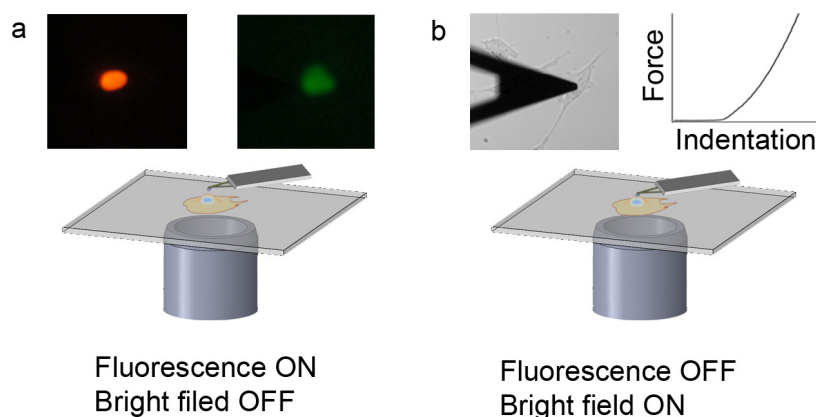
Figure 3.2: Combination of AFM and fluorescence microscopy to determine cell stiffness through cell cycle, a) use fluorescence to identify cell cycle, and b) use AFM to measure stiffness of the identified single cell

3.3.3 Statistical analysis

Overall statistical significance of differences in mean stiffness among cell distributions was tested using the Kruskal-Wallis test. Significance of differences between all pairs of distributions was tested using Dunn's post test. All tests were run in Igor Pro (Wavemetrics, OR)

3.4 Results and discussion

3.4.1 Cells distributed unevenly among cell cycle phases

FUCCI cell cycle labeling successfully stained single cells from IOSE and HEY A8 cell types. Cells at G1 phase are only visible under TRITC excitation/emission filter, whereas cells at G2/early mitosis phase are only visible under FITC excitation/emission filter, cells at S phases are visible under both FITC and TRITC filters, while cells at late mitosis is identified by their morphology under bright filed microscopy. Representative fluorescence images of IOSE and HEY A8 cells labeled with FUCCI labeling kit are shown in Figure 3.3.
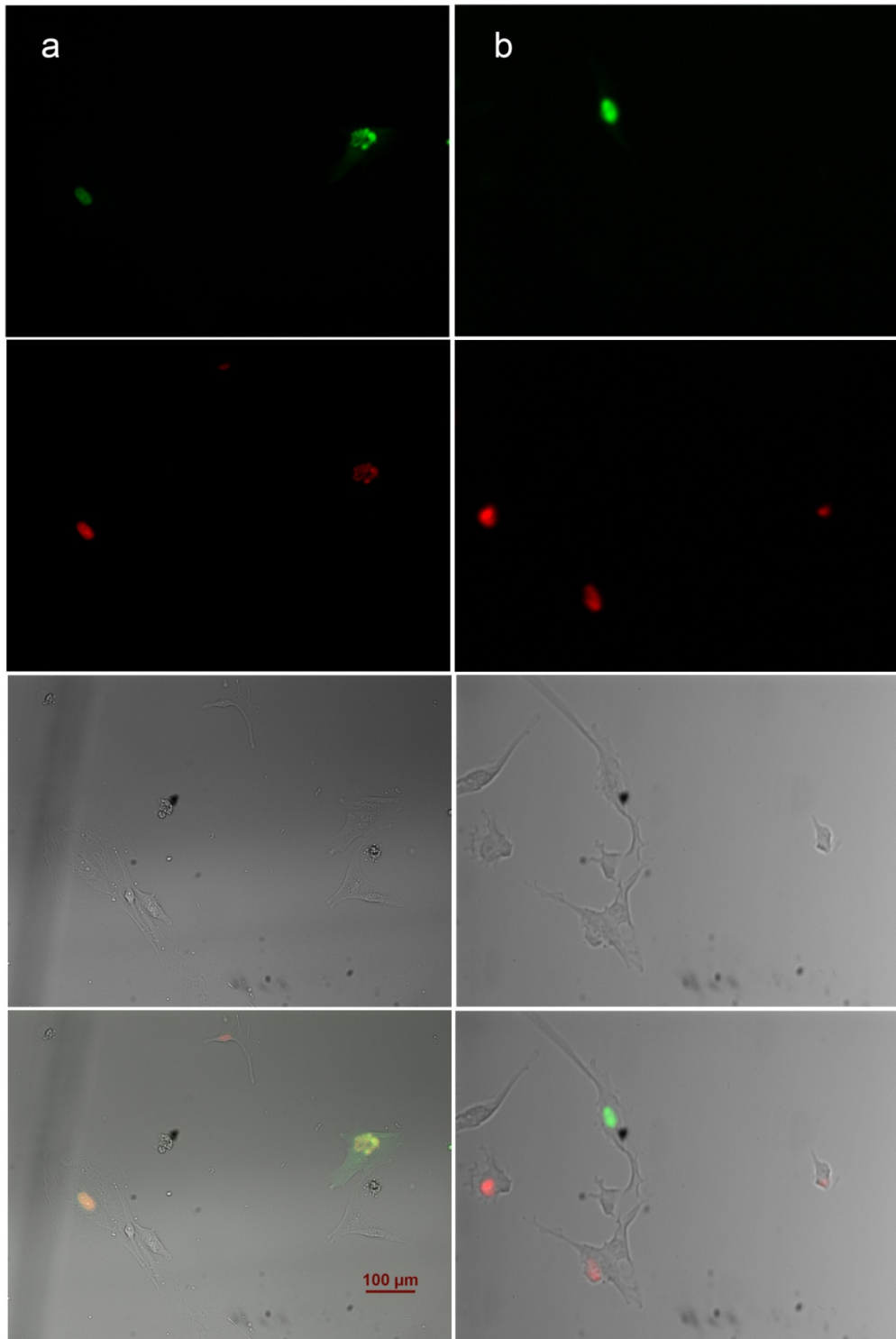
Figure 3.3: Representative fluorescence and bright field images of IOSE (column a) and HEY A8 (column b) cells labeled with FUCCI, from top to bottom: FITC, TRITC, bright field, overlay

Cells are not evenly distributed at four phases through the cell cycle, for both cell types, as there was a larger number of cells stained red than green, meaning larger fraction of cells were at G1 phase than G2 phase. The percentage of cells at G1 phase was 50% for IOSE and the percentage for HEY A8 cells was approximately the same.

3.4.2   *Single cell stiffness is modulated during the cell cycle*

Figure 3.4 shows representative force curves of IOSE cells at G1 phases versus G2/early M phase, the cells showed different fluorescence patterns under FITC/TRITC excitation/emission sets. Though the force curves in each graph both show some degree of variation in slope, which is the coarse indicator of stiffness, IOSE cells at G1 phase are generally stiffer than cells at G2/early M phase.
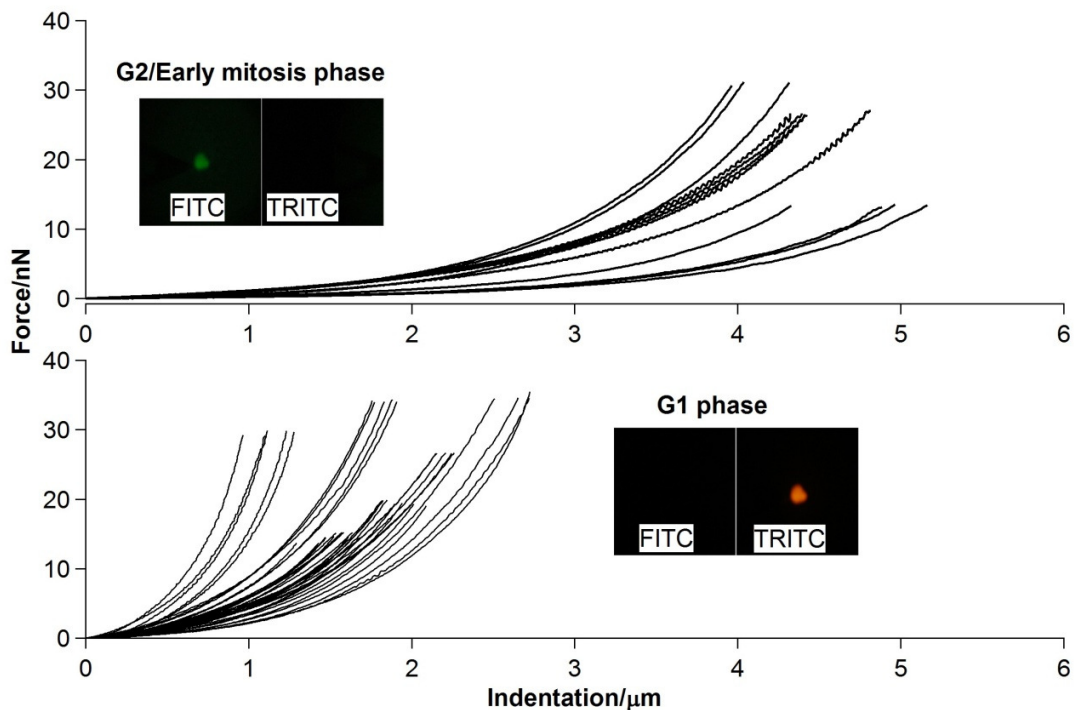
Figure 3.4: Representative force curves of IOSE cells at G1 versus G2/Early M phases

Figure 3.5 shows the distribution of stiffness as cells progress through the cell cycle, the inset shows our previous data of stiffness distribution of IOSE and HEY A8 in chapter 2 for comparison.
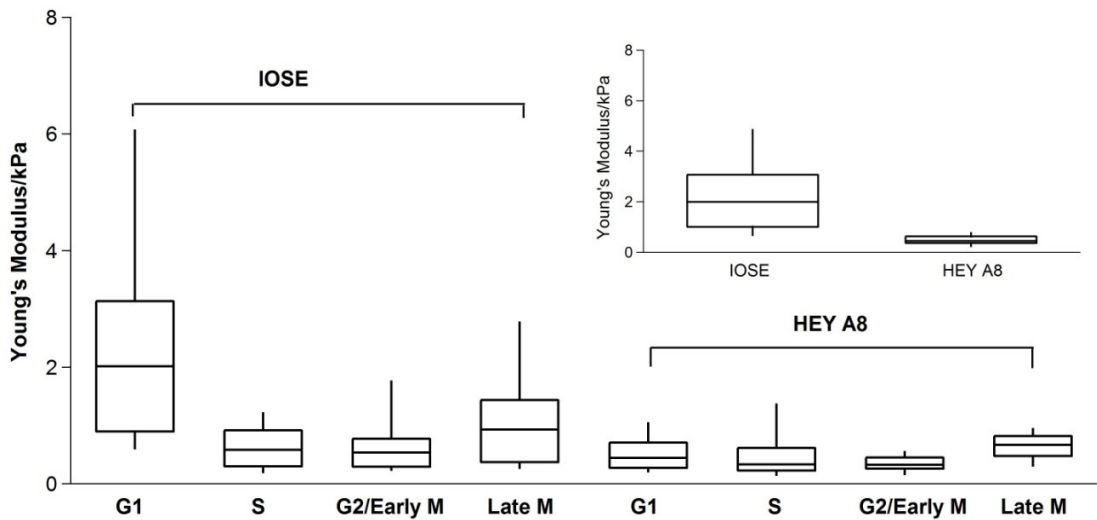
Figure 3.5: Box-and-whisker plots of single cells stiffness distribution of IOSE and HEY A8 through the cell cycle, the inset plot shows the previous data from chapter 2, the percentiles are 10%, 25%, 50%, 75% and 90%. Overall difference among distributions is significant (p-value$<1\times10^{-9}$, Kruskal-Wallis test). Early M=early mitosis, Late M=late mitosis

For IOSE, cells at G1 phases are in generally stiffer than cells at other three phases; in contrast, cell stiffness from HEY A8 doesn't show strong dependence on cell cycle. Stiffness distribution of IOSE and HEY A8 through cell cycle is consistent with the old data in chapter 2, as shown in the inset of Figure 3.5, which confirms that cell cycle labeling with FUCCI doesn't affect single cell stiffness of these two cell types. To better quantify the difference, the stiffness distributions were summarized in Table 3.1, Dunn's

test was performed with the pairwise differences between individual groups shown in
Table 3.2.

Table 3.1: Stiffness distribution of IOSE and HEY A8 through cell cycle

	IOSE		HEY A8	
	Mean Young's Modulus/Pa	Standard Deviation/Pa	Mean Young's Modulus/Pa	Standard Deviation/Pa
G1	2463	2127	514	301
S	699	648	461	385
G2/Early M	669	521	334	129
Late M	1471	2024	643	220

Table 3.2: Multiple comparison test of stiffness distribution of IOSE and HEY A8 (LM: late mitosis: EM: early mitosis)

Dunn's multiple comparison test		Difference in rank sum	Significant? ($p<0.05$)
Group A	Group B		
IOSE G1	HEY A8 G2/EM	108.777	Yes
IOSE G1	HEY A8 S	94.3515	Yes
IOSE G1	HEY A8 G1	82.0515	Yes
IOSE G1	IOSE G2/EM	70.4293	Yes
IOSE G1	IOSE S	68.0126	Yes
IOSE G1	HEY A8 LM	57.5515	No
IOSE G1	IOSE LM	42.8438	Yes
IOSE LM	HEY A8 G2/EM	65.9327	No
IOSE LM	HEY A8 S	51.5077	No
IOSE LM	HEY A8 G1	39.2077	No
IOSE LM	IOSE G2/EM	27.5855	No
IOSE LM	IOSE S	25.1688	No
IOSE LM	HEY A8 LM	14.7077	No
HEY A8 LM	HEY A8 G2/EM	51.225	No
HEY A8 LM	HEY A8 S	36.8	No
HEY A8 LM	HEY A8 G1	24.5	No
HEY A8 LM	IOSE G2/EM	12.8778	No
HEY A8 LM	IOSE S	10.4611	No
IOSE S	HEY A8 G2/EM	40.7639	No
IOSE S	HEY A8 S	26.3389	No
IOSE S	HEY A8 G1	14.0389	No
IOSE S	IOSE G2/EM	2.41667	No
IOSE G2/EM	HEY A8 G2/EM	38.3472	No

Table 3.2(Continued)

IOSE G2/EM	HEY A8 S	23.9222	No
IOSE G2/EM	HEY A8 G1	11.6222	No
HEY A8 G1	HEY A8 G2/EM	26.725	No
HEY A8 G1	HEY A8 S	12.3	No
HEY A8 S	HEY A8 G2/EM	14.425	No

From the results of stiffness distribution and pairwise comparison shown above, IOSE cells at G1 phase are statistically stiffer than any other group except HEY A8 cells at late mitosis, other groups are not statistically different from each other in stiffness distribution.

The dependence of cell stiffness on cell cycle phases is consistent with the structure characteristics of the F-actin network observed from the distinct actin cytoskeleton structures of IOSE and HEY A8 cells shown in chapter 2. The fraction of cells at G1 phase is larger than that of any other phases for HEY A8 and IOSE cells. The actin network of HEY A8 cells is irregular and unstructured for almost every cell investigated in the actin staining experiment in chapter 2, implying the actin cytoskeleton displays an irregular structure throughout the cell cycle. In contrast, the majority of IOSE cells display actin networks well organized but more variant in density and organization, therefore we further speculate that IOSE cells at G1 phase have more regularities in their actin density and structural organization than cells at other phases. This speculation is consistent with previous studies [3] showing that cells during the interphase have more organized F-actin structures than those at mitosis.

 In both IOSE and HEY A8 cell types, the stiffest cells are in G1 phase, followed by late mitosis, which is higher than other two groups in mean stiffness. While this is indicated

in Figure 3.5 and Table 3.1, late mitosis phase could be difficult to detect and therefore may be misidentified in practice. The cell cycle labeling technique we used in these studies does not positively identify cells in the late mitosis phases but only through a lack of fluorescence under excitation, so it is possible that these cells were not in late mitosis but rather unsuccessfully stained. In addition, when fluorescence signal is too weak to be detectable, it's possible that cells at G1 phases are misidentified as at late mitosis.

If we consider the stiffness of cells at each cell cycle phase and the corresponding fractions of cells at this specific phase, the distributions of single cell stiffness through the cell cycle as tested in this study show consistent stiffness to previously measured results for ovarian cancer cell mechanics [25]. Therefore, the stiffness distribution of cells through the cell cycle, together with the results we obtained in chapter 2, not only provide insightful mechanical and biological information about ovarian cancer cells, but also contribute to the designing of biomechanical assays for ovarian cancer diagnosis.

3.5   Summary and conclusion

In this study, we measured single cell stiffness as a function of positions through the cell cycle. The stiffness distributions we obtained here are consistent with our previous data on ovarian cell mechanics from chapter 2, therefore cell labeling with the FUCCI stain does not significantly affect the mechanical properties of the cells in our experiments. Comparing the results for IOSE and HEY A8 cell types showed that only IOSE cells at G1 phases are significantly stiffer than the corresponding phases of HEY A8. IOSE cells at other phases and didn't display significant difference in mean Young's modulus compared to HEY A8.

91

The results shown here provided detailed information of cell cycle dependence of mechanical stiffness in IOSE and HEY A8 cell types, it will not only deepen the understanding of normal and cancerous cell cycle from the mechanical perspective, but also help to illustrate the interplay of mechanics and cellular biology in cancer development.

3.6   References

1.   Ridley, A.J., *Rho-related proteins: actin cytoskeleton and cell cycle.* Current Opinion in Genetics & Development, 1995. **5**(1): p. 24-30.

2.   Provenzano, P.P. and P.J. Keely, *Mechanical signaling through the cytoskeleton regulates cell proliferation by coordinated focal adhesion and Rho GTPase signaling.* Journal of Cell Science, 2011. **124**(8): p. 1195-1205.

3.   Heng, Y.-W. and C.-G. Koh, *Actin cytoskeleton dynamics and the cell division cycle.* The International Journal of Biochemistry & Cell Biology, 2010. **42**(10): p. 1622-1633.

4.   Ingber, D.E., et al., *Cell shape, cytoskeletal mechanics, and cell cycle control in angiogenesis.* Journal of biomechanics, 1995. **28**(12): p. 1471-1484.

5.   Huang, S., C.S. Chen, and D.E. Ingber, *Control of Cyclin D1, p27Kip1, and Cell Cycle Progression in Human Capillary Endothelial Cells by Cell Shape and Cytoskeletal Tension.* Molecular Biology of the Cell, 1998. **9**(11): p. 3179-3193.

6.   Foisner, R., *Dynamic organisation of intermediate filaments and associated proteins during the cell cycle.* BioEssays, 1997. **19**(4): p. 297-305.

7.   Assoian, R.K. and X. Zhu, *Cell anchorage and the cytoskeleton as partners in growth factor dependent cell cycle progression.* Current Opinion in Cell Biology, 1997. **9**(1): p. 93-98.

8.   Provenzano, P.P., et al., *Matrix density-induced mechanoregulation of breast cell phenotype, signaling and gene expression through a FAK-ERK linkage.* Oncogene, 2009. **28**(49): p. 4326-4343.

9.   Provenzano, P.P., et al., *Contact Guidance Mediated Three-Dimensional Cell Migration is Regulated by Rho/ROCK-Dependent Matrix Reorganization.* Biophysical Journal, 2008. **95**(11): p. 5374-5384.

10.   Wang, N., J.D. Tytell, and D.E. Ingber, *Mechanotransduction at a distance: mechanically coupling the extracellular matrix with the nucleus.* Nat Rev Mol Cell Biol, 2009. **10**(1): p. 75-82.

11.   Schafer, K.A., *The Cell Cycle: A Review.* Veterinary Pathology Online, 1998. **35**(6): p. 461-478.

12.   Collins, K., T. Jacks, and N.P. Pavletich, *The cell cycle and cancer.* Proceedings of the National Academy of Sciences, 1997. **94**(7): p. 2776-2778.

13.   Olson, M., A. Ashworth, and A. Hall, *An essential role for Rho, Rac, and Cdc42 GTPases in cell cycle progression through G1.* Science, 1995. **269**(5228): p. 1270-1272.

14.   Howell, A.S. and D.J. Lew, *Morphogenesis and the Cell Cycle.* Genetics, 2012. **190**(1): p. 51-77.

15.   Sánchez, I. and B.D. Dynlacht, *New insights into cyclins, CDKs, and cell cycle control.* Seminars in Cell & Developmental Biology, 2005. **16**(3): p. 311-321.

16.   Sherr, C.J., *Cancer Cell Cycles.* Science, 1996. **274**(5293): p. 1672-1677.

17.   Hartwell, L. and M. Kastan, *Cell cycle control and cancer.* Science, 1994. **266**(5192): p. 1821-1828.

18.   Bueno, M.J. and M. Malumbres, *MicroRNAs and the cell cycle.* Biochimica et Biophysica Acta (BBA) - Molecular Basis of Disease, 2011. **1812**(5): p. 592-601.

19.   Evan, G.I. and K.H. Vousden, *Proliferation, cell cycle and apoptosis in cancer.* Nature, 2001. **411**(6835): p. 342-348.

20.   Ridley, A.J., *Rho proteins and cancer.* Breast Cancer Research and Treatment, 2004. **84**(1): p. 13-9.

21.   Foster, I., *Cancer: A cell cycle defect.* Radiography, 2008. **14**(2): p. 144-149.

22.   Pruitt, K. and C.J. Der, *Ras and Rho regulation of the cell cycle and oncogenesis.* Cancer Letters, 2001. **171**(1): p. 1-10.

23.   Parri, M. and P. Chiarugi, *Rac and Rho GTPases in cancer cell motility control.* Cell Communication and Signaling, 2010. **8**: p. 23.

24.   Sahai, E. and C.J. Marshall, *RHO-GTPases and cancer.* Nat Rev Cancer, 2002. **2**(2): p. 133-142.

25.   Xu, W., et al., *Cell Stiffness Is a Biomarker of the Metastatic Potential of Ovarian Cancer Cells.* PLoS ONE, 2012. **7**(10): p. e46609.

26.   Friedman, E., et al., *Actin Cytoskeletal Organization Loss in the Benign-to-Malignant Tumor Transition in Cultured Human Colonic Epithelial Cells.* Cancer Research, 1984. **44**(7): p. 3040-3050.

27.   Friday, B.B. and A.A. Adjei, *K-ras as a target for cancer therapy.* Biochimica et Biophysica Acta (BBA) - Reviews on Cancer, 2005. **1756**(2): p. 127-144.

28.   Vermeulen, K., D.R. Van Bockstaele, and Z.N. Berneman, *The cell cycle: a review of regulation, deregulation and therapeutic targets in cancer.* Cell Proliferation, 2003. **36**(3): p. 131-149.

29.   Kelly, G.M., et al., *Bone cell elasticity and morphology changes during the cell cycle.* Journal of biomechanics, 2011. **44**(8): p. 1484-1490.

30.   Tsai, M.A., R.E. Waugh, and P.C. Keng, *Cell cycle-dependence of HL-60 cell deformability.* Biophysical Journal, 1996. **70**(4): p. 2023-2029.

31.   Dvorak, J.A. and E. Nagao, *Kinetic Analysis of the Mitotic Cycle of Living Vertebrate Cells by Atomic Force Microscopy.* Experimental Cell Research, 1998. **242**(1): p. 69-74.

32.   Poperechnaya, A., et al., *Localization and Activity of Myosin Light Chain Kinase Isoforms during the Cell Cycle.* The Journal of Cell Biology, 2000. **151**(3): p. 697-708.

33.   Kendall, F., et al., *Nuclear morphometry during the cell cycle.* Science, 1977. **196**(4294): p. 1106-1109.

34.   Skalli, O., Y.H. Chou, and R.D. Goldman, *Cell Cycle-Dependent Changes in the Organization of an Intermediate Filament-Associated Protein: Correlation with Phosphorylation by p34cdc2.* Proceedings of the National Academy of Sciences of the United States of America, 1992. **89**(24): p. 11959-11963.

35.   Fishkind, D.J. and Y.-L. Wang, *Orientation and Three-Dimensional Organization of Actin Filaments in Dividing Cultured Cells.* The Journal of Cell Biology, 1993. **123**(4): p. 837-848.

36.   Keng, P., C. Li, and K. Wheeler, *Synchronization of 9L rat brain tumor cells by centrifugal elutriation.* Cell Biochemistry and Biophysics, 1980. **2**(3): p. 191-206.

37.   Palis, J., B. King, and P. Keng, *Separation of spontaneously differentiating and cell cycle-specific populations of HL-60 cells.* Leukemia Research, 1988. **12**(4): p. 339-344.

38.   Chen, M., et al., *Serum Starvation Induced Cell Cycle Synchronization Facilitates Human Somatic Cells Reprogramming.* PLoS ONE, 2012. **7**(4): p. e28203.

39.   Khammanit, R., et al., *Effect of serum starvation and chemical inhibitors on cell cycle synchronization of canine dermal fibroblasts.* Theriogenology, 2008. **70**(1): p. 27-34.

40.   Cho, S.R., et al., *Effects of Confluent, Roscovitine Treatment and Serum Starvation on the Cell-cycle Synchronization of Bovine Foetal Fibroblasts.* Reproduction in Domestic Animals, 2005. **40**(2): p. 171-176.

41.   Schorl, C. and J.M. Sedivy, *Analysis of cell cycle phases and progression in cultured mammalian cells.* Methods, 2007. **41**(2): p. 143-150.

42.   Han, Z.-M., et al., *Flow cytometric cell-cycle analysis of cultured fibroblasts from the giant panda, Ailuropoda melanoleuca L.* Cell Biology International, 2003. **27**(4): p. 349-353.

43. Tobey, R.A., N. Oishi, and H.A. Crissman, *Cell cycle synchronization: reversible induction of G2 synchrony in cultured rodent and human diploid fibroblasts.* Proceedings of the National Academy of Sciences, 1990. **87**(13): p. 5104-5108.

44. Holley, R.W. and J.A. Kiernan, *"Contact inhibition" of cell division in 3T3 cells.* Proceedings of the National Academy of Sciences, 1968. **60**: p. 5.

45. Liliensiek, S.J., et al., *Cell sorting but not serum starvation is effective for SV40 human corneal epithelial cell cycle synchronization.* Experimental Eye Research, 2006. **83**(1): p. 61-68.

46. Cooper, S., *Rethinking synchronization of mammalian cells for cell cycle analysis.* Cellular and Molecular Life Sciences, 2003. **60**(6): p. 1099-1106.

47. Huang, Y., et al., *Serum withdrawal and etoposide induce apoptosis in human lung carcinoma cell line A549 via distinct pathways.* Apoptosis, 1997. **2**(2): p. 199-206.

48. Hayes, O., et al., *Cell confluency is as efficient as serum starvation for inducing arrest in the G0/G1 phase of the cell cycle in granulosa and fibroblast cells of cattle.* Animal Reproduction Science, 2005. **87**(3–4): p. 181-192.

49. Gibbons, J., et al., *Enhanced Survivability of Cloned Calves Derived from Roscovitine-Treated Adult Somatic Cells.* Biology of Reproduction, 2002. **66**(4): p. 895-900.

50. Ciechanover, A., A. Orian, and A.L. Schwartz, *Ubiquitin-mediated proteolysis: biological regulation via destruction.* BioEssays, 2000. **22**(5): p. 442-451.

51. Sakaue-Sawano, A., et al., *Visualizing Spatiotemporal Dynamics of Multicellular Cell-Cycle Progression.* Cell, 2008. **132**(3): p. 487-498.

52. Vodermaier, H.C., *APC/C and SCF: Controlling Each Other and the Cell Cycle.* Current Biology, 2004. **14**(18): p. R787-R796.

53. Méchali, M. and M. Lutzmann, *The Cell Cycle: Now Live and in Color.* Cell, 2008. **132**(3): p. 341-343.

54.   Hutter, J.L. and J. Bechhoefer, *Calibration of atomic-force microscope tips.* Review of Scientific Instruments, 1993. **64**(7): p. 1868-1873.

55.   Johnson, K.L., *Contact mechanics*. 1985, Cambridge, UK: Cambridge university press.

56.   Xu, W., N. Chahine, and T. Sulchek, *Extreme Hardening of PDMS Thin Films Due to High Compressive Strain and Confined Thickness.* Langmuir, 2011. **27**(13): p. 8470-8477.

CHAPTER 4

POINTWISE HERTZIAN METHOD ACCURATELY MEASURES NONLINEARITY IN POLYMERS

4.1 Abstract

The cell is a highly complex material and cell stiffness is unlikely be able to quantified by a single value of Young's modulus during deformations. Mechanical nonlinearity is pronounced as cells undergo large deformations and strains, such as those that may occur during metastasis as invasive cancer cells travel through small confines to enter new tissue spaces. Having established the correlation between cell stiffness and metastatic potential of cancer cells in chapter 2, we further investigate the nonlinear nature of the mechanical properties of cancer cells. To better understand the nonlinear mechanical properties of materials in stiffness measurements with atomic force microscopy (AFM), a methodology using a pointwise contact mechanics method is developed and tested on a simple hyperelastic polydimethylsiloxane (PDMS) sample shaped into well-defined geometries.

We use this methodology to determine the mechanical properties of ultrathin PDMS films undergoing large strains. The PDMS was molded into extremely thin films of variable thickness and adhered to a hard substrate. We found that for films below 1 µm in thickness, the Young's modulus increased with decreasing sample thickness with a power law exponent of 1.35. Furthermore, as the soft PDMS film was indented, significant strain-hardening was observed as the indentation depth approached 45% of the sample thickness for all thicknesses measured. To properly quantify the nonlinear mechanical measurements, we utilized a pointwise Hertzian method which assumes only piecewise

linearity on the part of the probed material. This analysis revealed three regions within the polymer material. A linear region with a constant Young's modulus was seen for compression up to 45% strain. At strains higher than 45%, a marked increase Young's modulus was measured. The onset of strain induced stiffening is well modeled by finite element modeling and occurs as stress contours expanding from the probe and the substrate overlap. A third region of mechanical variation occurred at small indentations of less than 10 nm. The pointwise Young's modulus at small indentations was several orders of magnitude higher than that in the linear elasticity region; we studied and eliminated causes responsible for this phenomenon. In total, these effects can cause thin elastomer films to become extremely stiff such that the measured Young's modulus is over a hundredfold higher than the bulk PDMS. Therefore, the mechanics of polymeric materials can be changed by simply adjusting the geometry of a material, in addition to changing the material itself. In addition to understanding the mechanics of thin polymer films, this work provides an excellent test of experimental techniques to measure the mechanics of other nonlinear and heterogeneous materials such as biological cells, or to understand how modulus will change as different parts of the cell is indented.

4.2   Introduction

The mechanical properties of biological materials are complicated by a variety of effects, such as stress-strain nonlinearity and scale/geometry dependent behavior. Such effects may dominate the mechanical behavior of soft matter. For example, it is well known that thin layers of polymeric materials may be stiff and that the stiffness will increase with indentation (i.e. nonlinear). Even the size-normalized stiffness, or modulus, also can exhibit scale-dependent behavior. Single cells, as a complex biological material, are

usually immobilized on hard substrates during stiffness measurement with atomic force microscope, with the resultant force curves fitted with the Hertz model to calculate Young's modulus. This methodology could generate erroneous results, since the Hertz model assumes small deformation and homogeneity in material, but both assumptions are usually violated during stiffness measurement with AFM. As shown in Figure 4.1, large deformation during indentation and intrinsic heterogeneity of single cells both impair the applicability of the Hertz model in the determination of Young's modulus but are usually overlooked.
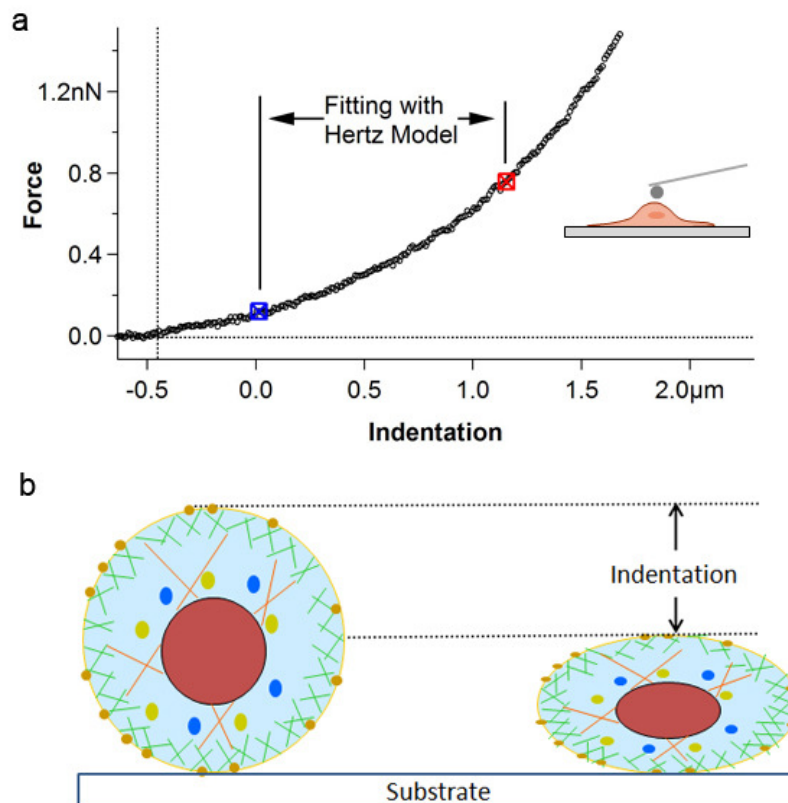
Figure 4.1: Large deformation and heterogeneity of single cells ignored in stiffness measurements with AFM, a) traditional method of fitting force curve with Hertz model gives a single value regardless of indentation depth, the inset sketches AFM indentation on single cells, and b) single cells usually undergo large deformations comparable to their sizes during stiffness measurements

As shown in Figure 4.1, single cells are heterogeneous and large deformation introduces nonlinearity in force response, fitting the force curve with the Hertz model regardless of indentation depth generates one single value of Young's modulus and could lead to wrong estimation of mechanical properties of the cell.

Accounting for nonlinear mechanics of single cells is especially important when considering the deformation of invasive cancer cells during metastasis as illustrated in Figure 4.2. During metastasis, cells deform largely to be able to travel through limited

space in the extracullar matrix (ECM) and the small pores on the blood vessel. The large deformation makes the mechanical behavior of the cells highly nonlinear.
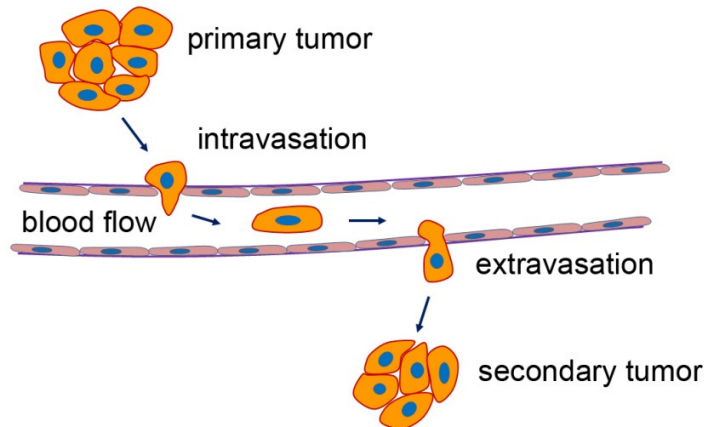
Figure 4.2: Cancer cells undergo large deformation during metastasis; cells undergo large deformation when entering and leaving the blood vessel

To properly quantify the nonlinear mechanical measurements with AFM, we used a pointwise Hertzian model, initially developed by Costa *et al.* [1], which assumes only piecewise linearity on the part of the measured material. Prior to the application of this methodology to cell mechanics measurements, a validation of this methodology is implemented on a simple polymer film.

A wedge-shaped ultrathin film was fabricated from PDMS to validate the pointwise Hertzian approach to determining nonlinear mechanics. PDMS is a hyperelastic material and therefore can undergo large deformation without showing any plasticity, making it good for simulating single cell mechanics under large deformation. PDMS and other soft elastomeric polymers are also frequently constructed with micrometer dimensions for use

in many science and engineering applications [2-5]. As small deformations of PDMS within microdevices can impact their function [6, 7], understanding how strain and geometry affects the mechanical properties of PDMS is of considerable relevance[8, 9]. However, few studies have investigated PDMS mechanics at the micro/nanoscale, where even small displacements can lead to deformations that are comparable to sizes of the samples, and significant modulations of the mechanics of the polymer are required.

Indentation of thin films and biomaterials with the atomic force microscope (AFM) is a widely used method to characterize mechanical properties [1, 10-12]. To properly quantify the mechanical properties from the force indentation curves, researchers apply various models, which include the Hertz model, JKR model and DMT model [13], to obtain a Young's modulus [1, 13, 14]. However, indentation of materials defined by nanoscale dimensions differs from traditional indentation in that small deformations of geometrically confined materials can lead to deviations from the properties of bulk materials [15-19].

The objective of this research is to test the pointwise Hertzian model on ultrathin PDMS films upon hard substrates, to determine the effect of the geometry (thickness of the film) as well as the applied strain on their mechanical properties. The results and methodology developed here will lead to the further investigation of nonlinear mechanics of single cells. In previous studies of thin PDMS films, the polymer films used were at least ten microns in thickness [18, 19], which prohibited the emergence of strong nonlinear mechanical behavior due to very high strains (>45%). High strain or large deformation allows to simulate nonlinear mechanics of single cells and to observe novel physical effects, which serves to improve our understanding of cell mechanics in stiffness

measurements and metastasis. In this study, we probe PDMS films which have thicknesses ranging from 43 nm to 1 µm. These ultrathin elastomer films allow us to generate significant strains of over 50%. The large compressive strains reveal highly nonlinear mechanical behavior. Consequently, we have employed a pointwise model, developed first by Costa [1]**Error! Reference source not found.**, to analyze the indentation-dependent stiffness of ultrathin PDMS without any assumptions of linearity of the polymer and therefore can be used to quantitatively describe the strain dependent stiffness. We also improved the model by including the effect of adhesion, since adhesion could a big effect in biology. The experimentally determined indentation dependent Young's modulus plots obtained agreed with the finite element modeling (FEM) simulations of PDMS thin films upon an underlying glass substrate.

We explored the response of ultrathin PDMS films in three regions: contact, small deformation, and large deformation ranges. We find that at small deformations, (strain<45%), the modulus increased to the 1.35 power as the sample thickness decreased. The modulus value gradually approached the value for the bulk sample for film thickness greater than 900 nanometers. In the large deformation range, the Young's modulus abruptly increases with indentation, indicating significant strain hardening. In addition to the stiffening due to geometry and strain, previous studies have shown that the point of contact results in extremely high values of Young's modulus [20-22]. This phenomenon of contact stiffening occurs over very small indentations of a few nanometers. Based upon our pointwise analysis of thin polymer films, we show that the contact stiffening phenomenon is not due to probe-sample adhesion.

4.3 Materials and methods

4.3.1 Sample preparation

The thin PDMS film used in this research was fabricated using Sylgard 184 Silicone Elastomer Kit from Dow Corning. The mixture of two components was placed in a vacuum chamber to remove the gas in the mixture, and then poured between two angled glass slides to form a PDMS film of decreasing thickness at the end. The curing process took place in an oven at 60 ˚C for 30 minutes. The top slide was carefully separated to reveal a thin PDMS film with slightly varying thickness bonded to a glass substrate, as shown in Figure 4.3a. The thickness of the film at the locations of the indentation was determined by AFM topography measurement. The thickness for the experiment was measured to be 43 nm to 90 nm, and shown schematically as locations A to D in Figure 4.3 a. In addition thicker PDMS samples were investigated (1000 nm and greater), though the thickness was measured with optical microscopy. The nanoindentation experiment conducted on samples of different thicknesses investigated the dependence of sample thickness on the force response.
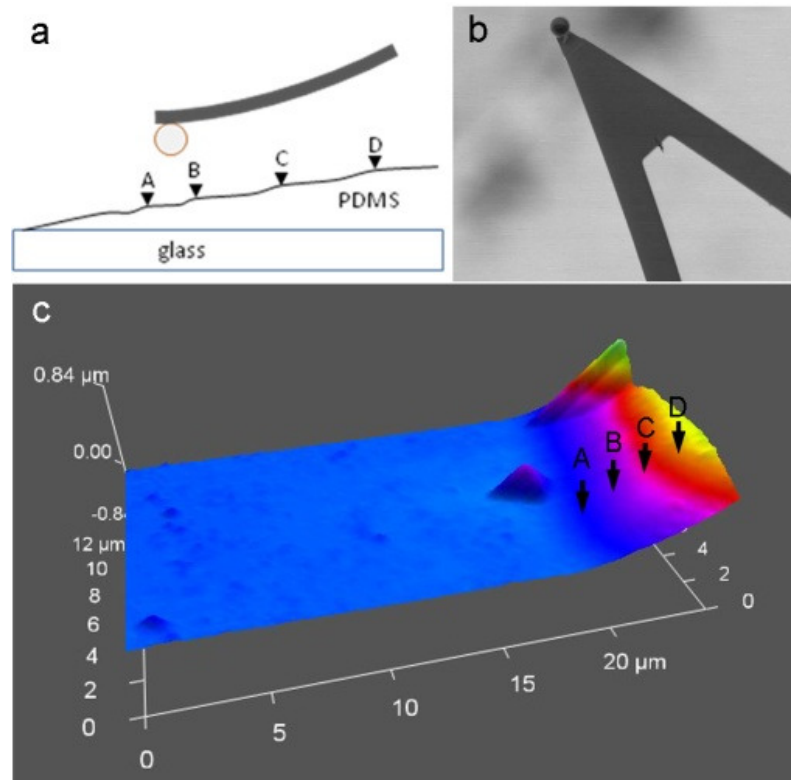
Figure 4.3: Experimental configuration and sample topography, a) Experimental configuration of the mechanical measurement. b) A beaded cantilever tip that is similar to that used in this study; and c) Topological profile of the PDMS sample acquired by AFM

4.3.2 *Atomic Force Microscope imaging and stiffness measurements*

The AFM (Asylum MFP-3D) was used for both imaging of the polymer films and for polymer mechanics measurements. Cantilevers from Olympus (Model #:AC160TS) were used as indenters. To simplify the contact geometry between the indenter and the PDMS sample, the cantilever was modified by attaching a silica microsphere on the tip, as shown in Figure 4.3b. The nominal value of the microsphere diameter is 4.74 μm. The modified cantilever indenter was calibrated on the glass substrate, and the spring constant was determined as 61.0 N/m using thermal vibration method [23], in which a Lorentzian function was used to fit the thermal noise spectrum. In all experiments, the deflection of

the cantilever did not exceed the linearity of the photo sensitive detector, even for forces up to 16 μN. AFM was combined with an inverted optical bright field microscope (Nikon Ti-U) to align the cantilever to the PDMS sample. Samples of different thicknesses used in this study include 43 nm, 52 nm, 70 nm, 90 nm, and 1000 nm. Bulk PDMS samples (thickness values much greater than a micron) were also studied for comparison.

4.3.3   Modified Hertz model & JKR model

The Hertz model is widely used in contact mechanics research [14, 24]. Hertz derived this model to describe the normal contact between two deformable spheres and the model has been adapted for other contact geometries as well [24, 25]. The details of Hertz model has been described in chapter 1 with mathematical expressions in Equations 1.1 and 1.2.

The topography of the PDMS surface at the indentation location, and thus the cross sectional profiles, were obtained by AFM scanning; by analyzing the specific cross sectional profile, we were able to determine the radius of curvature in the corresponding orientation. The smallest radius of curvature of the PDMS surface at the indentation locations is 24 μm, therefore our assumption that the indented surface is flat compared to the radius of the indenter is valid, and thus we simplify R to R_1, the radius of the microsphere used in this study.

The Hertz model assumes linear elasticity, which is typically valid when the indentation is small compared to the sample thickness (small strain). However, PDMS is a hyperelastic material and can elastically undergo large nonlinear deformations. In this case, the assumption of small indentation is not valid and the Hertz model will not accurately predict the mechanical response of the material. To obtain the pointwise

Young's modulus, we follow the methodology developed by Costa *et al.* [26]. Briefly, each data point (δ_i, P_i) in the indentation-force curve obtained from experiments was substituted into Eq. 2 to calculate the corresponding E_i^*. The point wise Young's modulus E^* versus indentation δ can then be plotted.

In order to examine the contact response of ultrathin PDMS, we employed the JKR (Johnson-Kendall-Roberts) model to determine the effect of adhesion force on contact conformations. The mathematical expressions for the JKR model are shown in Equations 4.1 and 4.2, where σ is the surface energy between indenter and sample and the other parameters are the same as described previously.

$$a^3 = \frac{R\left(P+3\sigma\pi R+\sqrt{6\sigma\pi RP+(3\sigma\pi R)^2}\right)}{E^*}$$

Eqn. 4.1

$$E^* = \frac{\left(\frac{2}{3}P\right)^{\frac{3}{2}}}{\delta^{\frac{3}{2}}R^{\frac{1}{2}}\left[P+3\sigma\pi R+\sqrt{6\sigma\pi RP+(3\sigma\pi R)^2}\right]^{\frac{1}{2}}}$$

Eqn. 4.2

When the indentation is small, the adhesion force plays an important role in deforming the contact conformation [14] and hamper interpretation of the data. However, as the indentation increases, the significance of the adhesion force decreases and the JKR model will typically approach the Hertz model in describing contact behavior between the indenter and sample.

### 4.3.4   Finite Element simulation

We also used the finite element analysis (FEA) simulation software Abaqus from SIMULIA to simulate PDMS contact mechanics for comparison with the experimental measurements. We follow the work of previous researchers [1]. The PDMS film was

modeled as a planar, axisymmetric mesh. The silica bead was modeled as a rigid body, with a diameter of 4.74 μm, which contacts the PDMS mesh during the course of simulation. The bottom of the PDMS mesh was fixed in position to simulate adherence to the substrate. To capture the hyperelasticity of PDMS during the large deformation of our experiments, we used the Mooney-Rivlin model [27]**Error! Reference source not found.** which is appropriate for rubber-like materials undergoing large deformations [17]**Error! Reference source not found.**. For incompressible hyperelastic materials, the model derives the stress-strain relationship from the expression $W=C_1(I_1-3)+C_2(I_2-3)$, where W is the strain energy function, $I_1=$ trace(G), and $I_2=$(trace(G)-trace(G^2))/2, where G is the right Cauchy-Green deformation tensor defined as $G=FF^T$, with F as the deformation gradient tensor. C_1 and C_2 are material constants, which were obtained by fitting the experimental force versus indentation curve of the 90-nm-thick film and then input into Abaqus to model the other thicknesses. The indentation depths used in the simulation were identical to the experimental values.

4.4   Results and discussion

4.4.1 Mechanical behaviors deviate from Hertz model

The results for nanoindentation of ultrathin PDMS films are shown and compared in Figure 4.4. Individual force versus indentation curves for 43 nm, 52 nm, 70 nm, and 90 nm thick PDMS samples are plotted on the same scale. From these data, it is clear that the slope at a given indentation increases with decreasing film thickness.
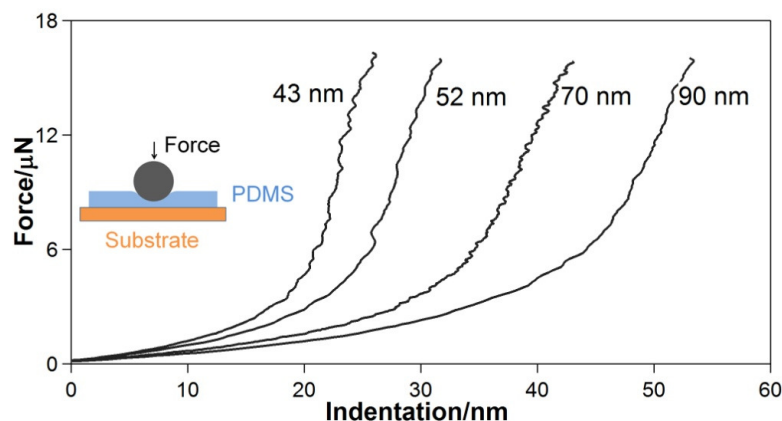
Figure 4.4: Force versus indentation curves for 45 nm, 52 nm, 70 nm and 90 nm thick PDMS samples. The inset sketches the indentation on PDMS

Figure 4.5 compares the experimental data to a Hertzian contact model of force indentation by an indenter, as well as a FEA simulation of a thin elastomer in compression. The experimental force curves and the FEA simulations closely match over the whole indentation range for all polymer thicknesses. The FEA results do show slight deviations in regions, which may be due other factors not taken into account in the model, such as friction between the sample and the indenter due to probe adhesion [28]. Also from Figure 4.5, we see that the Hertz model does not accurately describe the relationship between force and indentation for PDMS compression over large strain values. It is apparent that the Hertz model is initially relatively accurate, but deviates from the experimental data at indentation greater than 45% of the film thickness. This result is not surprising in light of the fact that even small indentations of thin polymer films on a hard substrate will cause large strains and an apparent hardening, and has been described in several previous articles [15, 16, 29].
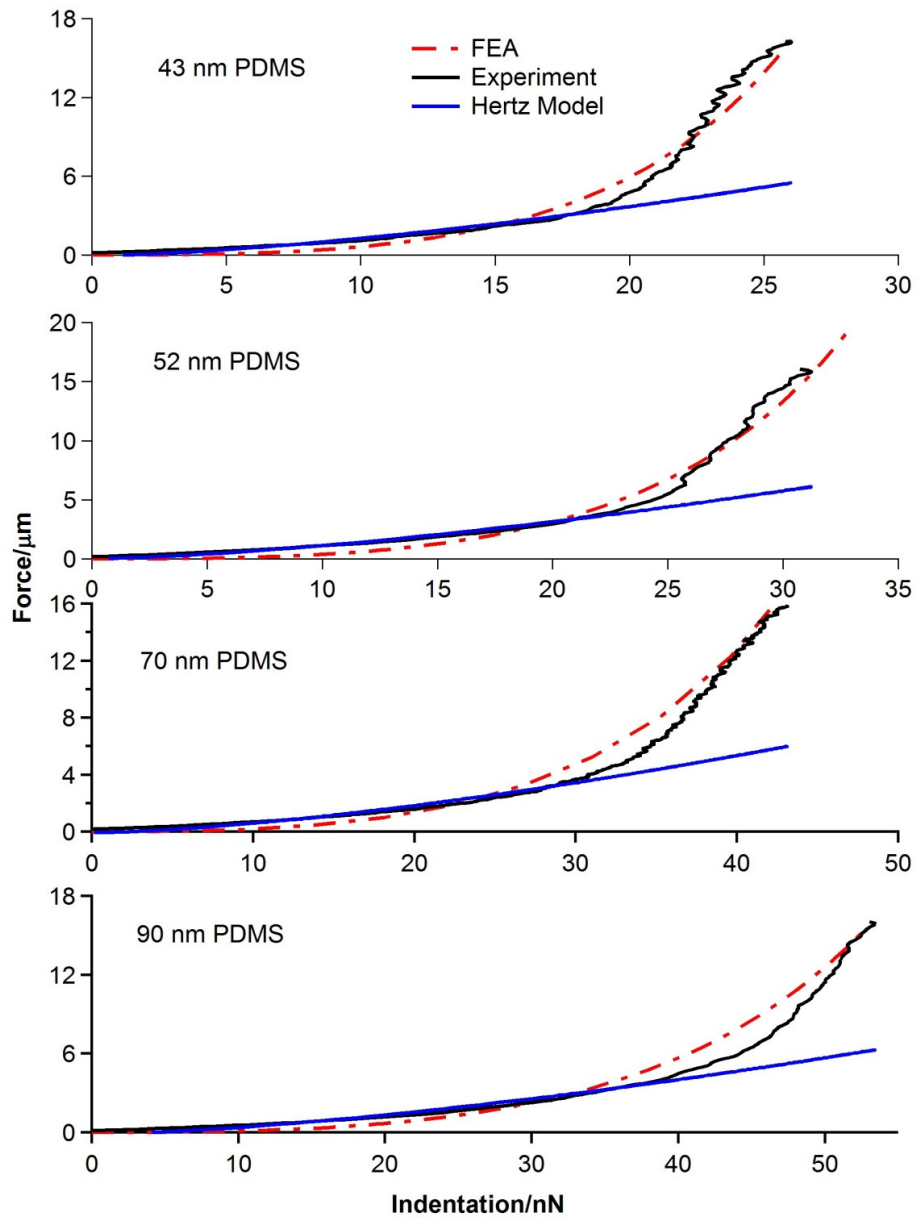
Figure 4.5: Experimental force curves and FEA simulation results for PDMS films for 43nm, 52nm, 70nm and 90nm samples. Legends: FEA: force-indentation curve obtained from FEA simulation, Experiment: experimental force curves from AFM, Hertz model: force curve predicted by Hertz model at the indentation values

### 4.4.2 Pointwise Young's modulus versus thickness

The stiffness of nonlinear materials can be empirically determined by fitting the Hertz model to sections of the force versus indentation curve to calculate a pointwise Young's modulus [1]. The pointwise Young's modulus plotted as a function of indentation (Figure 4.6) determines the amount of deformation at which point nonlinearity in the stiffness emerges. We highlight three regions of interest in the modulus-indentation relationship of PDMS samples with different thicknesses, identified by three partitions separated by indentation values δ_1 and δ_2. Region 1 is characterized by a constant Young's modulus independent of indentation; in region 2, the Young's modulus increases with indentation, indicating an increasing stiffness; and in region 3 (i.e. immediately post contact), the Young's modulus initially shows a very high value upon contact and then drops drastically to a constant level. For an indentation depth within region 1, the point wise elastic modulus was found to be nearly constant with indentation for each sample, therefore, the mechanical behavior is linear and Hertz model is applicable to this indentation range. As the indentation increases to region 2, the effect of underlying hard substrate becomes appreciable and gradually dominates the measured mechanical stiffness. This fact is consistent with the results shown in Figure 4.5.
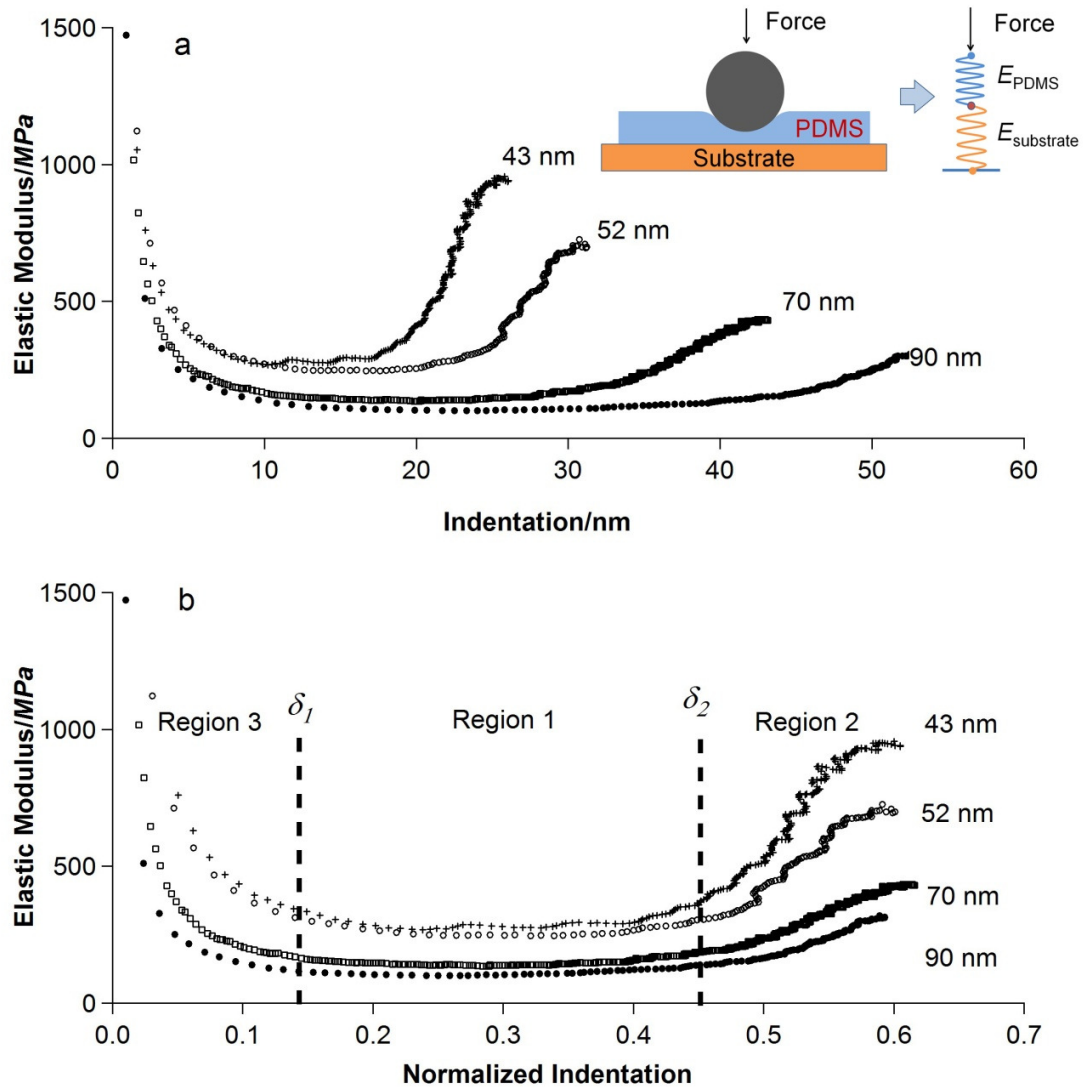
Figure 4.6: Pointwise Young's modulus versus a) indentation, the inset shows the effect of the substrate on the mechanical measurements; and b) normalized indentation for 45 nm, 52 nm, 70 nm and 90 nm thick PDMS samples.

We define δ_2 as a transition point from linearity to nonlinearity based upon a change of slope of the modulus-indentation plot. We find the value of δ_2 to be dependent on sample thickness. As shown in Figure 4.7, the transition points are plotted versus thicknesses. The slope of the line obtained from linear regression fitting is 0.4533 (R^2 value is

0.9999), meaning that the linear elasticity region occurs until the indentation approaches 45% of the thickness.
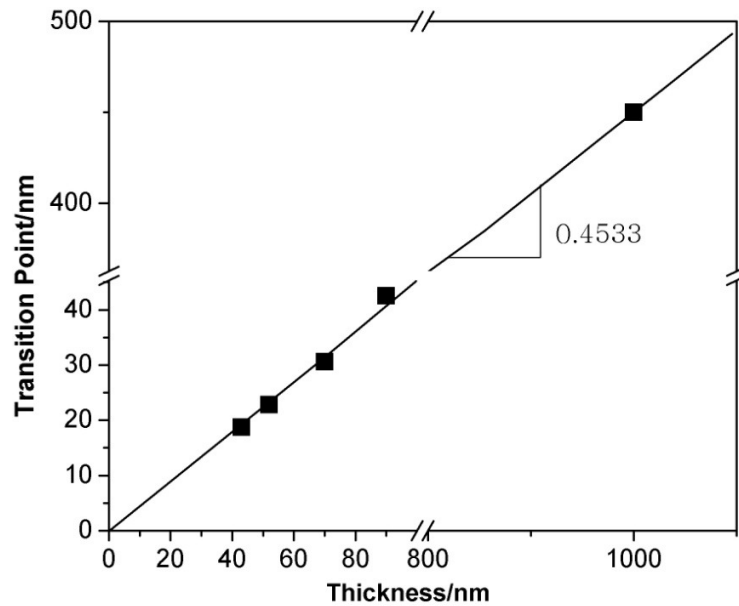
Figure 4.7: A plot showing the indentation of transition from Region 1 to Region 2 (δ_2) versus PDMS thickness.

To explain the onset of an increased modulus in region 2 at a consistent strain, we carefully scrutinize the stress evolution in the FEA simulation. Figure 4.8 shows the stress evolution for 90 nm-PDMS thin film. As the indenter compresses the PDMS film, increased stress contours develop at both the indenter-sample interface and also at the PDMS-substrate interface. For moderate indentations ($\delta<\delta_2$), these two zones of increased stress were not in physical contact, leading to a constant pointwise Young's modulus as the region of low stress remained. However, as the indentation increased to 33% of film thickness, these two zones of increased stress gradually converge. As the

114

indentation reaches 45% of the film thickness, high stress values fully develop throughout the region between the indenter and substrate, coinciding with an increase in the pointwise modulus. We carried out FEM simulations for other sample thicknesses and observed a similar evolution of stress contours with increasing indentation, culminating in a uniform high stress at 45% indentation for all sample thicknesses, consistent with the experimental results.
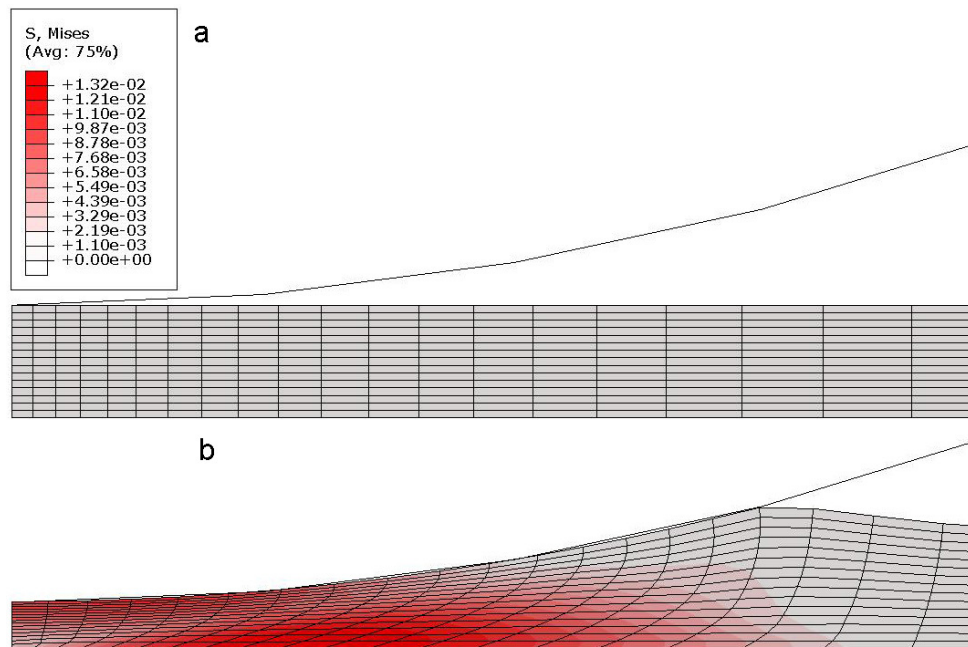
Figure 4.8: The evolution of stress in the 90 nm thick PDMS sample in the FEA simulation, a) before and b) after deformation

As we show in Figure 4.6, the compressive elastic modulus in region 1 increases with decreasing PDMS thickness. To quantify the dependence of the elastic modulus to sample thickness, we implemented the same nanoindentation experiment on a 1-μm-thick sample and a bulk PDMS sample. The pointwise Young's modulus versus indentation

plots for these two thicknesses are shown in Figure 4.9. The elastic modulus of the 1-μm-thick PDMS sample in the linear elasticity region 1 is identical to that of the bulk sample. We also note that the 1-μm-thick PDMS layer also shows a significant increase in the pointwise elastic modulus at 45% strain, consistent with what we have observed from the ultrathin PDMS samples. Comparing the moduli in region 1, denoted by E_1, for the range of sample thicknesses, we see a quantitative dependence of elastic modulus in region 1 on sample thickness. To investigate the dependence of E_1 on sample thickness, we plot E_1 versus sample thickness. As shown in Figure 4.10, E_1 is found to be inversely proportional to (thickness)$^{-1.35}$ (R^2 value is 0.9852), with the elastic modulus converging to that of bulk at a PDMS thicknesses greater than 900 nm.
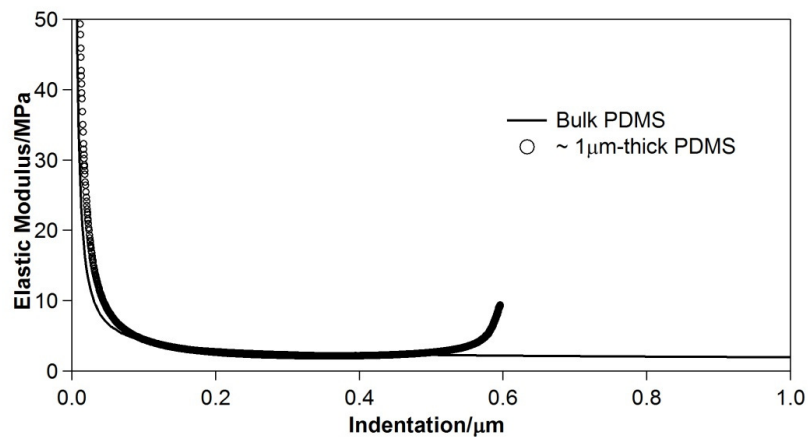
Figure 4.9: Plot showing pointwise Young's modulus versus indentation for 1 μm thick and bulk PDMS. Note that the modulus of bulk PDMS is dramatically lower compared to thin film PDMS shown in Figure 4.6.
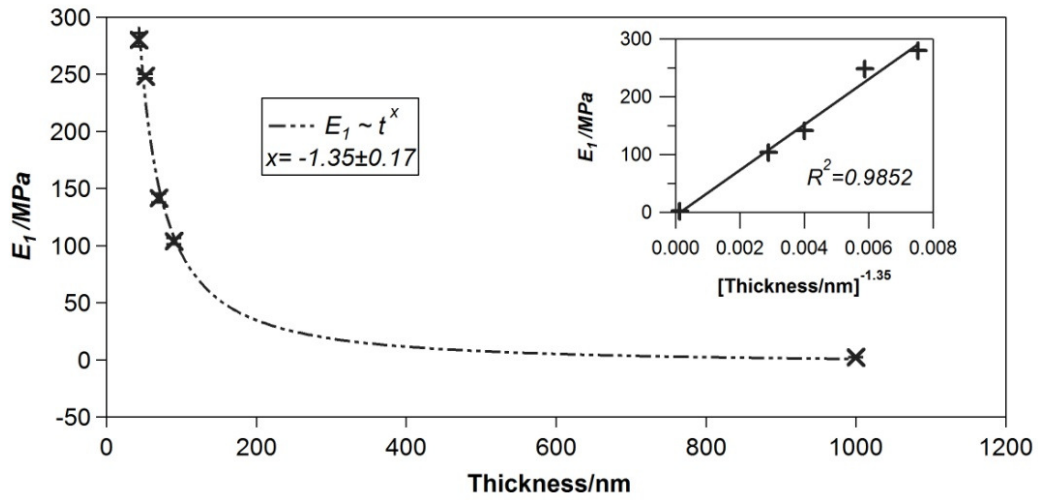
Figure 4.10: Average Young's modulus in region 1 (E_1) for different sample thicknesses. The standard deviation for the data is below the size of the markers in this figure. The inset plots E_1 as a function of (thickness)$^{-1.35}$.

From Figure 4.9 and 4.10, the modulus of bulk PDMS is dramatically lower than the PDMS thin films shown in Figure 4.6, but is almost identical to the modulus of 1 μm PDMS in the before the onset of nonlinearity, indicating the effect of geometrical confinement on mechanics vanished when film thickness reaches 1 μm.

The dependence of stiffness on size has also been reported for tensile electrospun nanofibers [30], in which the elastic modulus increases abruptly when the diameter of the nanofiber decreases to a certain threshold [30] . Previous literature [31, 32] also reported the power relationship between the Young's modulus and thickness for polymeric films, although these studies studied films several orders of magnitude higher in thickness and found a dependence on thickness$^{-0.5}$. O'Connell and Mckenna found a dramatic stiffening of polyvinyl acetate film in rubbery region, the stiffness scales with approximately (thickness)$^{-2}$ [33]; Xu and Mckenna also showed that the Young's modulus of ultrathin

117

PBMA films scales with (thickness)$^{-1}$ [34]; Rowland and co-workers also found the stiffening of layers compared to bulk polystyrene [35]. Although we did not investigate this discrepancy in the index, we do expect that surface tension, also known as residual stress, will play a significant role in the mechanics as the ratio of surface area to volume becomes large and may be a factor contributing to the increasing of Young's modulus with decreasing thickness [36, 37]. As the thickness of the sample decreases, the ratio of the surface molecules to the interior volume molecules increases, increasing the contribution from the surface tension to mechanical stiffness. If this interpretation is correct, our data suggests negligible contribution from surface tension to occur at 900 nm and thus the Young's modulus of the thin film approaches the value for bulk material.

4.4.3   Point wise Young's modulus in small indentation region (Region 3)

A remarkable observation seen in the pointwise Young's modulus plots is the extremely high values for elastic modulus for initial indentation, denoted as region 3. This observation has been reported in previous studies [20-22, 37] and the result is puzzling as the elastic modulus is calculated to be orders of magnitude higher than the value for the elastic modulus in region 1. We have investigated this phenomenon by adjusting several experimental parameters and excluded these factors as an entire explanation. Even by accounting for probe adhesion and misidentification of the contact point, we continue to measure a contact-dependent change in modulus.

Probe-sample adhesion can lead to significant deviation of the expected contact area determined from the Hertz model, resulting in an artificially high pointwise Young's modulus. As surface energy plays an important role in nanoscale contact mechanics [14]**Error! Reference source not found.**, it can conceivably lead to extremely high measured

118

modulus in the small indentation region. We developed a pointwise JKR (Johnson, Kendall, Roberts) model [14] to account for the effect of probe-sample surface energy on the pointwise Young's modulus. The probe-sample surface energy was determined from a subsequent adhesion measurement to the compressive modulus measurement [38]. As expected, the measured modulus is drastically reduced at small indentations, but significant contact stiffening remains (Figure 4.11). To confirm that probe adhesion is not leading to an artificially high modulus, we repeated the experiment in deionized water to eliminate capillary forces, which can apply several nanoNewtons of adhesive force leading to significant deviation from Hertzian assumptions. Using the pointwise JKR model and a liquid measurement environment, the measured pointwise elastic modulus in region 3 still exceeds the elastic modulus in region 1 by several orders of magnitude. Accounting for and reducing the adhesive forces between the sample and indenter cannot explain the extremely high modulus in region 3.
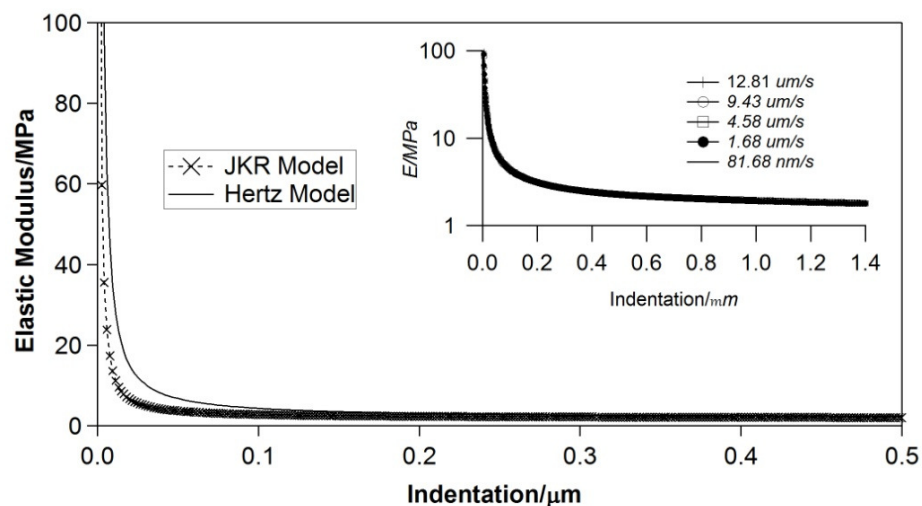
Figure 4.11: Pointwise Young's modulus plots determined using the Hertz and JKR model. The inset shows the effect of loading speed.

119

To rule out viscoelastic effects that may account for the contact stiffening, we also varied the loading speed of the indentation process, which had no effect on the modulus. The indenting loading speed was tested at: 12.8 μm/s, 9.4 μm/s, 4.6 μm/s, 1.7 μm/s and 0.87 μm/s, and the results show no effect of loading speed on the elastic modulus as indicated in the inset of Figure 4.11. The measurements were performed at the same location on the bulk PDMS and the pointwise JKR model was used to eliminate the influence of surface energy on the result. Surface viscoelasticity has been investigated for other materials and the results show a close agreement with the published data for bulk materials [39], Due to the lack of dependence of modulus on loading rate, we reason that viscoelasticity is not a significant factor causing the high modulus at small indentations.

There is some debate concerning the physical properties of the interfacial region near surface of ultrathin polymer films. Some researchers have suggested the existence of a liquid-like region near the surface of polystyrene films [40, 41] resulting from a lower glass transition temperature than the bulk material, whereas others have shown there to be little or no change in glass transition temperature or existence of the liquid layer [42]. Also, buckling-based methods can be used to determine the elastic moduli of ultrathin polymer films [43-47]. Stafford and co-workers [48]**Error! Reference source not found.** measured the elastic moduli for a series of ultrathin polymer films deposited on thick, PDMS substrates. By examining the wrinkling instability of these films and fitting the data with a bilayer model, they found that as the thicknesses of these thin films became smaller, the surface regions of the thin films became softer. In our study, we do not find evidence of the presence of a softer liquid layer in PDMS.

120
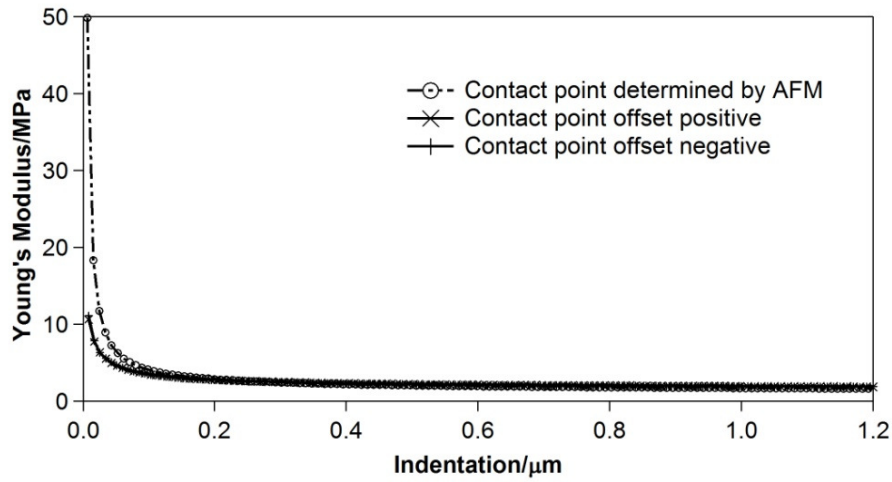
Figure 4.12: Pointwise Young's modulus determined after shifting the contact point to higher and lower values.

Previous explanations of contact stiffening include the misidentifying of the contact point while determining the pointwise Young's modulus [12]. To investigate the effect of misidentifying the contact point, we purposely shifted the contact point to greater and lesser values while repeated the fitting procedure. As seen in Figure 4.12, offsetting the contact point both to both higher and lower values decreases the Young's modulus in the small indentation region 3, but does not completely eliminate the effect in our measurements. In addition, the offset produces a slightly worse fit of the data for the remaining portion of the force curve. While we have not ruled out the role of accurate identification of the contact point, one alternative explanation of high stiffness includes the role of a unique interfacial region between the indenter and the polymer upon contact and the elevated glass transition temperature T_g with respect to the uncontacted surface [21]. An elevated T_g would shift the interfacial region to a glassy regime, leading to significant stiffening in comparison to rubbery regime. In addition, the reduction of molecular mobility at the interface, which is induced by the attraction between the

indenter and surface, could also contribute to the stiffening of the surface [21]**Error! Reference source not found.**. Hydrostatic pressure at the contact interface leading to an elevation of T_g in several other polymers, including polystyrene, poly(methyl methacrylate [49, 50], and polycarbonate [51]**Error! Reference source not found.**, have been reported. For small indentations, the interfacial region dictates the mechanical behavior of the nanoindentation force response, however, as the indentation increases, the volumetric proportion of the interfacial region decreases as the total volume of strained polymer increases, and thus the contribution of the interfacial region to the overall mechanical response becomes negligible for sufficient indentation.

4.5   Summary and conclusion

The mechanical properties of ultrathin PDMS films bonded to a hard glass substrate were studied using AFM. A pointwise Hertz method and JKR method were used to determine the indentation dependent Young's modulus. The mechanical properties of PDMS thin films were strongly influenced by high strain from compression between the indenter and the underlying substrate and showed an increase in the indentation dependent Young's modulus at consistent strain values of 45% for all samples studied. In addition, the mechanical properties of PDMS thin films were strongly affected by the thickness of the polymer at all strains. The average Young's modulus in region 1 (E_1) increased as the sample thickness decreased and gradually approached the modulus value for bulk sample for a thickness value greater than 900 nanometers. The experimental mechanical profile was accurately described by FEA simulation over the entire indentation range. The high elastic modulus in region 3 at the indenter-sample interface plays a dominant role in the contact mechanics and quickly becomes negligible as the indentation advances. Contact-

dependent stiffness does not seem to be exclusively caused by measurement artifacts, analysis methods, or by interfacial adhesion.

The results described here will enable predictive understanding of the mechanical properties of elastomeric materials under large deformations as can occur within microdevices [52-54]. These important properties of PDMS should be considered in device design where nanoscale elastomers undergo large deformations. In addition, the methods described here to reliably characterize nonlinear mechanical materials may also impact the study of other nonlinear materials such as cells. PDMS has some similar mechanical characteristics similar to single cells, including hyperelasticity and nonlinear elasticity [55]. Cell mechanics studies with AFM of adherent cells often report a stiffening due to the underlying substrate. In these experiments, adherent cells are typically immobilized onto a hard substrate and probed under large strain [56, 57]. It is often assumed that the underlying substrate strongly affects the measured mechanical properties, but the effect of material thickness has not been determined quantitatively. The methods described here can likewise be applied to understand heterogeneous and nonlinear materials such as cells, as long as an accurate measurement of cell thickness can be obtained. This research contributes a new perspective on quantifying and interpreting mechanical properties of cells and other nonlinear and thin materials.

4.6   References

1.   Costa, K.D. and F.C. Yin, *Analysis of indentation: implications for measuring mechanical properties with atomic force microscopy.* Journal of Biomechanical Engineering, 1999. **121**(5): p. 462-471.

2.   Shih, T.-K., et al., *Fabrication of PDMS (polydimethylsiloxane) microlens and diffuser using replica molding.* Microelectronic Engineering, 2006. **83**(11–12): p. 2499-2503.

3.   Nam, Y., K. Musick, and B.C. Wheeler, *Application of a PDMS microstencil as a replaceable insulator toward a single-use planar microelectrode array.* Biomedical Microdevices, 2006. **8**(4): p. 375-381.

4.   Yoonkey, N., et al., *Gold-coated microelectrode array with thiol linked self-assembled monolayers for engineering neuronal cultures.* Biomedical Engineering, IEEE Transactions on, 2004. **51**(1): p. 158-165.

5.   Jo, B.H., et al., *Three-dimensional micro-channel fabrication in polydimethylsiloxane (PDMS) elastomer.* Microelectromechanical Systems, Journal of, 2000. **9**(1): p. 76-81.

6.   Jeong, O.C. and S. Konishi, *Fabrication and drive test of pneumatic PDMS micro pump.* Sensors and Actuators A: Physical, 2007. **135**(2): p. 849-856.

7.   Zhang, W., et al., *PMMA/PDMS valves and pumps for disposable microfluidics.* Lab on a Chip, 2009. **9**(21): p. 3088-3094.

8.   Mata, A., A.J. Fleischman, and S. Roy, *Characterization of Polydimethylsiloxane (PDMS) Properties for Biomedical Micro/Nanosystems.* Biomedical Microdevices, 2005. **7**(4): p. 281-293.

9.   Tambe, N.S. and B. Bhushan, *Micro/nanotribological characterization of PDMS and PMMA used for BioMEMS/NEMS applications.* Ultramicroscopy, 2005. **105**(1–4): p. 238-247.

10.   Oliver, W.C. and G.M. Pharr, *An improved technique for determining hardness and elastic modulus using load and displacement sensing indentation experiments.* Journal of Materials Research, 1992. **7**(6): p. 1564-1583.

11.   AR, K., H. HR, and Y. FC., *Experimental and numerical analyses of indentation in finite-sized isotropic and anisotropic rubber-like materials.* Annals of Biomedical Engineering, 1997. **25**(6): p. 1009-1016.

12.   Crick, S.L. and F.C.P. Yin, *Assessing Micromechanical Properties of Cells with Atomic Force Microscopy: Importance of the Contact Point.* Biomechanics and Modeling in Mechanobiology, 2007. **6**(3): p. 199-210.

13. Grierson, D.S., E.E. Flater, and R.W. Carpick, *Accounting for the JKR-DMT transition in adhesion and friction measurements with AFM.* Journal of Adhesion Science and Technology, 2005. **19**(3-5): p. 291-311.

14. Johnson, K.L., K. Kendall, and A.D. Roberts, *Surface Energy and the Contact of Elastic Solids.* Proceedings of the Royal Society of London. A. Mathematical and Physical Sciences, 1971. **324**(1558): p. 301-313.

15. Dimitriadis, E.K., et al., *Determination of Elastic Moduli of Thin Layers of Soft Material Using the Atomic Force Microscope.* Biophysical Journal, 2002. **82**(5): p. 2798-2810.

16. Domke, J. and M. Radmacher, *Measuring the Elastic Properties of Thin Polymer Films with the Atomic Force Microscope.* Langmuir, 1998. **14**(12): p. 3320-3325.

17. Lin, D.C., E.K. Dimitriadis, and F. Horkay, *Elasticity of rubber-like materials measured by AFM nanoindentation.* Express Polymer Letters, 2007. **1**(9): p. 576-584.

18. Jee, A.-Y. and M. Lee, *Comparative analysis on the nanoindentation of polymers using atomic force microscopy.* Polymer Testing, 2010. **29**(1): p. 95-99.

19. Tranchida, D., S. Piccarolo, and M. Soliman, *Nanoscale Mechanical Characterization of Polymers by AFM Nanoindentations: Critical Approach to the Elastic Characterization.* Macromolecules, 2006. **39**(13): p. 4547-4556.

20. Mahaffy, R.E., et al., *Quantitative Analysis of the Viscoelastic Properties of Thin Regions of Fibroblasts Using Atomic Force Microscopy.* Biophysical Journal, 2004. **86**(3): p. 1777-1793.

21. Tweedie, C.A., et al., *Enhanced Stiffness of Amorphous Polymer Surfaces under Confinement of Localized Contact Loads.* Advanced Materials, 2007. **19**(18): p. 2540-2546.

22. Rico, F., et al., *Probing mechanical properties of living cells by atomic force microscopy with blunted pyramidal cantilever tips.* Physical Review E, 2005. **72**(2): p. 021914.

23. Hutter, J.L. and J. Bechhoefer, *Calibration of atomic-force microscope tips.* Review of Scientific Instruments, 1993. **64**(7): p. 1868-1873.

24. Johnson, K.L., *Contact mechanics.* 1985, Cambridge, UK: Cambridge university press.

25. Dintwa, E., E. Tijskens, and H. Ramon, *On the accuracy of the Hertz model to describe the normal contact of soft elastic spheres.* Granular Matter, 2008. **10**(3): p. 209-221.

26. Costa, K.D., A.J. Sim, and F.C.-P. Yin, *Non-Hertzian Approach to Analyzing Mechanical Properties of Endothelial Cells Probed by Atomic Force Microscopy.* Journal of Biomechanical Engineering, 2006. **128**(2): p. 176-184.

27. Treloar, L.R.G. *The Physics of Rubber Elasticity.* 1958. Oxford: Clarendon Press.

28. Zhang, M., Y.P. Zheng, and A.F.T. Mak, *Estimating the effective Young's modulus of soft tissues from indentation tests—nonlinear finite element analysis of effects of friction and large deformation.* Medical Engineering & Physics, 1997. **19**(6): p. 512-517.

29. Saha, R. and W.D. Nix, *Effects of the substrate on the determination of thin film mechanical properties by nanoindentation.* Acta Materialia, 2002. **50**(1): p. 23-38.

30. Arinstein, A. and E. Zussman, *Electrospun polymer nanofibers: Mechanical and thermodynamic perspectives.* Journal of Polymer Science Part B: Polymer Physics, 2011. **49**(10): p. 691-707.

31. Liu, M., et al., *Thickness-dependent mechanical properties of polydimethylsiloxane membranes* Journal of Micromechanics and Microengineering, 2009. **19**(3): p. 035028.

32. Oommen, B. and K.J. Van Vliet, *Effects of nanoscale thickness and elastic nonlinearity on measured mechanical properties of polymeric films.* Thin Solid Films, 2006. **513**(1–2): p. 235-242.

33. O'Connell, P.A. and G.B. McKenna, *Dramatic stiffening of ultrathin polymer films in the rubbery regime.* Eur Phys J E Soft Matter, 2006. **20**(2): p. 143-150.

34.   Xu, S., P.A. O'Connell, and G.B. McKenna, *Unusual elastic behavior of ultrathin polymer films: Confinement-induced/molecular stiffening and surface tension effects.* The Journal of Chemical Physics, 2010. **132**(18): p. 184902-9.

35.   Rowland, H.D., et al., *Molecular Confinement Accelerates Deformation of Entangled Polymers During Squeeze Flow.* Science, 2008. **322**(5902): p. 720-724.

36.   Dingreville, R., J. Qu, and C. Mohammed, *Surface free energy and its effect on the elastic behavior of nano-sized particles, wires and films.* Journal of the Mechanics and Physics of Solids, 2005. **53**(8): p. 1827-1854.

37.   Cuenot, S., et al., *Surface tension effect on the mechanical properties of nanomaterials measured by atomic force microscopy.* Physical Review B, 2004. **69**(16): p. 165410.

38.   Greenwood, J.A. and K.L. Johnson, *An alternative to the Maugis model of adhesion between elastic spheres.* Journal of Physics D: Applied Physics, 1998. **31**(22): p. 3279-3290.

39.   Houston, J.E., *A local-probe analysis of the rheology of a "solid liquid".* Journal of Polymer Science Part B: Polymer Physics, 2005. **43**(21): p. 2993-2999.

40.   Fakhraai, Z. and J.A. Forrest, *Measuring the Surface Dynamics of Glassy Polymers.* Science, 2008. **319**(5863): p. 600-604.

41.   Teichroeb, J.H. and J.A. Forrest, *Direct Imaging of Nanoparticle Embedding to Probe Viscoelasticity of Polymer Surfaces.* Physical Review Letters, 2003. **91**(1): p. 016104.

42.   Hutcheson, S.A. and G.B. McKenna, *Nanosphere Embedding into Polymer Surfaces: A Viscoelastic Contact Mechanics Analysis.* Physical Review Letters, 2005. **94**(7): p. 076103.

43.   Stafford, C.M., et al., *A buckling-based metrology for measuring the elastic moduli of polymeric thin films.* Nat Mater, 2004. **3**(8): p. 545-550.

44.   Nolte, A.J., M.F. Rubner, and R.E. Cohen, *Determining the Young's Modulus of Polyelectrolyte Multilayer Films via Stress-Induced Mechanical Buckling Instabilities.* Macromolecules, 2005. **38**(13): p. 5367-5370.

45.   Nolte, A.J., R.E. Cohen, and M.F. Rubner, *A Two-Plate Buckling Technique for Thin Film Modulus Measurements: Applications to Polyelectrolyte Multilayers.* Macromolecules, 2006. **39**(14): p. 4841-4847.

46.   Stafford, C.M., et al., *Combinatorial and high-throughput measurements of the modulus of thin polymer films.* Review of Scientific Instruments, 2005. **76**(6): p. 062207-5.

47.   Wilder, E.A., et al., *Measuring the Modulus of Soft Polymer Networks via a Buckling-Based Metrology.* Macromolecules, 2006. **39**(12): p. 4138-4143.

48.   Torres, J.M., C.M. Stafford, and B.D. Vogt, *Elastic Modulus of Amorphous Polymer Thin Films: Relationship to the Glass Transition Temperature.* ACS Nano, 2009. **3**(9): p. 2677-2685.

49.   Alcoutlabi, M. and G.B. McKenna, *Effects of confinement on material behaviour at the nanometre size scale.* Journal of Physics: Condensed Matter, 2005. **17**(15): p. R461-R524.

50.   Gacoin, E., et al., *Measurement of the mechanical properties of thin films mechanically confined within contacts.* Tribology Letters, 2006. **21**(3): p. 245-252.

51.   Jones Parry, E. and D. Tabor, *Pressure dependence of the shear modulus of various polymers.* Journal of Materials Science, 1974. **9**(2): p. 289-292.

52.   Alexeev, A., R. Verberg, and A.C. Balazs, *Patterned Surfaces Segregate Compliant Microcapsules.* Langmuir, 2007. **23**(3): p. 983-987.

53.   Lim, K., S. Kim, and J.H. Hahn, *Roller-type squeezing pump with picoliter handling capability.* Sensors and Actuators B: Chemical, 2003. **92**(1–2): p. 208-214.

54.   Schneider, F., et al., *Process and material properties of polydimethylsiloxane (PDMS) for Optical MEMS.* Sensors and Actuators A: Physical, 2009. **151**(2): p. 95-99.

55. Kang, I., et al., *Changes in the Hyperelastic Properties of Endothelial Cells Induced by Tumor Necrosis Factor-±* Biophysical Journal, 2008. **94**(8): p. 3273-3285.

56. Alonso, J.L. and W.H. Goldmann, *Feeling the forces: atomic force microscopy in cell biology.* Life Sciences, 2003. **72**(23): p. 2553-2560.

57. Lulevich, V., et al., *Cell Mechanics Using Atomic Force Microscopy-Based Single-Cell Compression.* Langmuir, 2006. **22**(19): p. 8151-8155.

CHAPTER 5

APPLCIATION OF THE POINTWISE HERTZIAN MODEL TO CELL MECHANICS

5.1 Abstract

The research investigating the nonlinear mechanics of PDMS ultrathin films in chapter 4 showed that the pointwise Hertzian method can be used to quantify the stiffness of materials as a function of indentation. In this chapter, we apply this method to study the nonlinear stiffness of single cells with AFM. The majority of eukaryotic cells consist of nuclear and cytoplasmic regions, and both contribute to the mechanical properties of single cells. The complexity of cellular structure makes the mechanical properties of single cells highly heterogeneous and nonlinear. In this chapter, we will apply pointwise Hertzian analysis to AFM force mapping to investigate the heterogeneity and nonlinearity of stiffness of ovarian cancer cells (HEY A8). With these methods we found that the nucleus is softer than the surrounding cytoplasm in HEY A8 cells. We also found a strong dependence of stiffness on the local cell thickness in the cortical region, indicating the importance of geometry in stiffness measurements of single cells.

5.2 Introduction

Cell mechanics is studied through the interaction of the cell with mechanical stimuli. The response/deformation of the cell to mechanical forces can affect its functionality during biological processes, as well as induce remodeling of the cellular internal structure through mechanically responsive biophysical pathways [1]. In our studies, we treat cells as a passive material and apply mechanical force to the cell and monitor the cellular deformation. Various continuum mechanics models have been proposed to describe the

mechanics of single cells [2-13]. The most common continuum mechanics model used with atomic force microscopy (AFM) to determine cell stiffness are Hertzian contact mechanics models [4, 14, 15]. Hertzian models simplify cells as linear elastic bodies [16, 17] and quantify the cell stiffness using linear elasticity or Young's modulus. However, cells undergo large deformations and are likely nonlinear in mechanics, violating the assumptions and leading to the failure of Hertzian model. In addition, cells are complex and highly heterogeneous materials [18, 19] and local mechanical heterogeneities were demonstrated using microrheology [18-21]; at the whole cell level, force mapping or scanning techniques revealed the spatial variation or heterogeneity in mechanical stiffness [16, 22-24]. The effects of nonlinearity on measurement were not evaluated to understand the impact of geometry. For example, the bending of the cantilever or the penetration of the indentor is typically a prescribed value during force mapping, the mechanical response might stay linear through the course of indentation at locations where the cell is thick; at locations where local thickness is small, however, the nonlinearity or the substrate effect could be significant for large strains and has to be considered to determine accurate mechanical insights. The nonlinearity in mechanical response from AFM indentation was previously determined by using an indentation-dependent Young's modulus, obtained using pointwise Hertzian method developed by *Costa* [25, 26]. Despite that nonlinearity and heterogeneity are studied in cell mechanics as discussed above, a systematic approach measuring spatial mechanics excluding nonlinearity or thickness dependence is required to evaluate the spatial inherent elasticity (hereafter referred to as elasticity) of single cells. While the cytoskeleton is the major component determining cell mechanics, the nucleus has also been shown to contribute to

cellular elasticity [21, 27, 28]. The coupling of the nucleus and cytoskeleton through the Linker of Nucleoskeleton and Cytoskeleton (LINC) complex across the perinuclear space also contributes to overall stiffness of the cell by stress transmission from the cytoskeleton to nuclear lamina [29-35].

Many studies have revealed that certain diseases alter nuclear structure, modify the associated nuclear structure proteins, and affect the nucleus mechanics [36-40]. For example, changes of nuclear lamin expression cause abnormalities in nucleus which are frequently observed in various types of cancer [41-50]. Morphological changes of nucleus are often used to identify the presence of cancer [45, 51-53]. Evidence also suggests the role of nucleus in migration and invasion process [54-57]. In spite of these qualitative studies on cancer nucleus, quantitative measurements of spatial mechanics of intact nuclei in invasive cancer cells under realistic physiological and biological conditions are desired to elucidate their mechanical complexities and their significance in metastasis.

To map the spatial elasticity without interference from the thickness dependence for single cells, we combined force mapping technique and pointwise Hertzian method capable of investigating nonlinear mechanical properties by calculating indentation-dependent stiffness. The pointwise Hertzian method analysis was used on each force curve collected during force mapping, and the linear elasticity was mapped across the scanned region. The results showed that the mechanical properties of the cell sample become nonlinear when indentation exceeds a specified strain, and that the linear elasticity of the sample displayed spatial variations and is highly heterogeneous. In cancerous HEY A8 cells, we found that the nucleus is softer than the surrounding

cytoplasm. We also observed a strong dependence of linear elasticity on the local cell thickness. The elasticity maps revealed the heterogeneity of cell stiffness and the strong stiffening of the cell edge due to geometry confinement, similar to that observed for PDMS polymers discussed in Chapter 4. The results demonstrated the necessity of considering the local region of the cell, the geometry of the local region, and the amount of strain in determining cell stiffness.

5.3   Materials and methods

5.3.1   Cell preparation

HEY A8 cell were grown in RPMI-1640 supplemented with 10% FBS and 1% antibiotic-antimycotic solution (R10 medium) as described previously. Before AFM experiments, cells were plated into a Fluorodish (World Precision Instruments, Sarasota, FL) with an initial density of 10,000-20,000 cells/cm^2 and then incubated at 37 ˚C overnight.

Atomic force microscopy and phase contrast microscopy

Atomic force microscopy (AFM) used here to conduct force mapping of single cells was MFP-3D from AsylumResearch (Santa Barbara, CA), the AFM probe used was MLCT-O10 (Bruker, Camarillo, CA) with a nominal spring constant of 30 pN/nm, a plain silica bead of 4.74 µm in diameter was glued to the end of the cantilever to minimize the lateral strain on the compressed cell. During the force mapping with AFM, cells were immobilized on the glass bottom of the Fluorodish. To visualize the intracellular structure and therefore structural heterogeneity of single cells during the measurements, a phase contrast microscopy integrated into the inverted optical microscope (Nikon, Melville, NY) was simultaneously used with AFM. Figure 5.1 shows an example of cell mechanics measurement on HEY A8 single cells using AFM and phase contrast microscopy, in

which the most cellular organelles are roughly visible under the microscope, with the glued bead and cell nucleus are clearly visible.
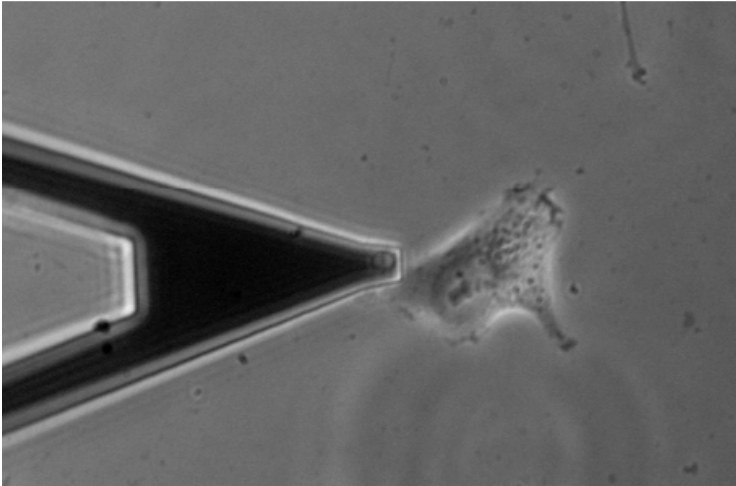
**Figure 5.1:** Simultaneous AFM and phase contrast microscopy on HEY A8 single cells

Prior to the force mapping, the AFM cantilever was calibrated on the glass bottom of the Fluorodish using thermal vibration method [58] and the thermal spectrum was fitted with Lorentizan function to determine the spring constant.

5.3.2   *Force mapping and pointwise Hertzian model*

Force mapping was conducted over single cells which are not in contact with others. In short, individual force curves are collected at equally distributed points across a two dimensional region of interest, the information of topographical and mechanical properties of the sample at each point is extracted from the corresponding force curve. During this process, the spatial correspondence between these points/pixels and force curves is attained. In our experiment, the scan area was carefully chosen to include cell

nucleus and lamellipodium, typically ranged from 40 to 80 µm, the scan resolution is either 16×16 or 32×32 to ensure good resolution and continuity in topographical and mechanical property measurements across the scan region.

Pointwise Hertzian model [25, 26] is based on Hertzian contact mechanics model but doesn't assume small indentation and linear elasticity, making it a good tool to analyze nonlinearity as we discussed in chapter 4. In this study, pointwise Hertzian model was utilized to evaluate any possible nonlinear mechanical behavior during indentation, excluding nonlinearity from evaluation of stiffness and obtaining the map of linear elasticity (Young's modulus) of the cell across the scan region. In our experiment, the original MFP-3D software came with the AFM was modified using customized MATLAB codes to integrate the function of pointwise Hertzian model and generate 2-D maps of linear elasticity or Young's modulus. The process of calculating 2-D modulus map from the force map is simply exemplified by a 4×4 force mapping in Figure 5.2, with F is the force, δ is the indentation, E is the pointwise Young's modulus, and $E_{i,j}$ is the average pointwise Young's modulus in the linear region obtained at location (i,j)
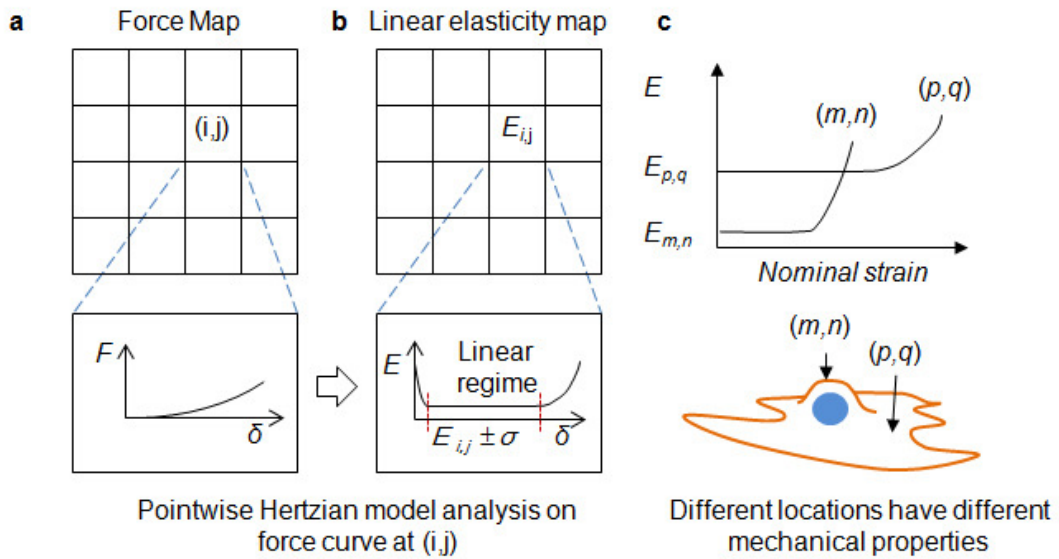
Figure 5.2: A 2-D linear elasticity map generated from a 4×4 force map, a) force mapping collects force curves on equally distributed locations within the region of interest, b) pointwise Hertzian model analysis on each force curve determines the elasticity in the linear regime, and assembly the elasticity in the linear region at each location into a 2-D matrix, which is the elasticity map, and c) the mechanical heterogeneity of single cells is reflected by the pointwise Young's modulus and corresponding value in the elasticity map

5.3.3 Cellular structure imaging with confocal microscopy

To analyze the shape and structure of nucleus, actin cytoskeleton and plasma membrane in HEY A8 cells, single cells were fixed, stained and imaged with confocal microscopy. Cells were grown on a glass coverslip to a density of 5,000 cells/cm^2 in a well of a 6-well plated with 2 mL cell culture media. The cell culture was put in an incubator of 37 ˚C overnight and then stained with fluorochrome-conjugated phalloidin. The cells were first fixed with 1 mL 4% formaldehyde in PBS (pH 7.4) for 10 min, permeabilized with 1 mL 0.2% TX-100, blocked with 1% BSA for 20 min and incubated for one hour with 1:20 Alexa Fluor 546 phalloidin (Life Technologies, Grand Island, NY) in 1% BSA. The nuclei were stained with Hoechst (Life Technologies, Grand Island, NY). To evaluate the

size of nucleus and the surrounding cytoplasm, and therefore to determine the fraction of the cellular space occupied by the nucleus and cytoplasm for each region of the cell, the plasma membrane and nucleus were also stained and imaged confocally. The plasma membrane was stained using CellMask deep red plasma membrane stain (Life Technologies, Grand Island, NY) at the concentration of 5 µg/mL, and nucleus was stained the same way as stated above, after the staining cells were fixed for future analysis. All steps during the staining process were conducted at room temperature in a dark room. After staining, the cells were sandwiched between the glass coverslip and a glass slide, mounted with ProLong Gold and sealed with nail polish.

After the staining, multiple fluorescence images of nucleus and actin cytoskeleton were acquired using a Zeiss LSM 510 NLO confocal microscope (Zeiss, Thornwood, NY). The z-stack function was also used to obtain the 3-D structural information of the nucleus, actin cytoskeleton and plasma membrane, the analysis was limited to single cells which were not in contact with other cells. The z steps was chosen to be small enough to ensure good resolution and no layer of fluorescent actin or nucleus missed during the imaging.

5.3.4   Inhibition of Rho kinase by Y-27632

To evaluate the contribution of contractility *via* the ROCK pathway to single cell stiffness, single cells treated with ROCK inhibitor Y-27632 (BD Biosciences, San Jose, CA) were compared with HEY A8 cells without treatment. During the treatment, HEY A8 cells were incubated in 50 µM and 100 µM Y-27632 in cell culture media for 1 hour at 37 ˚C prior to AFM stiffness measurements. After the treatment, elasticity map was analyzed for these samples and compared with sample without treatment.

5.4 Results and discussion

5.4.1 *Cells shows nonlinear mechanical response under AFM indentation*

Individual force curves were analyzed using pointwise Hertzian model to calculate the Young's modulus as a function of indentation. The resultant force curves and pointwise Young's moduli showed mechanical behavior and were exemplified in Figure 5.3.
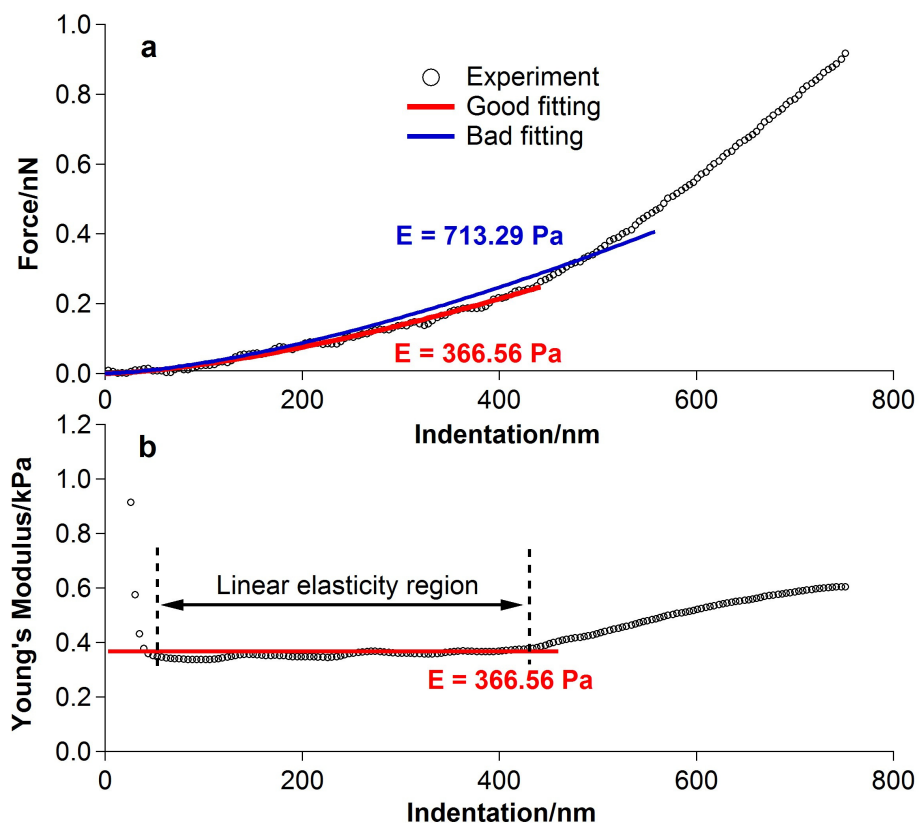
**Figure 5.3:** Hertz model (resulting in a single modulus) and pointwise Hertzian model in stiffness determination, a) force curve showed the nonlinear behavior as the experimental curves deviates from Hertz model, and b) pointwise Young's modulus as a function of indentation showed increase in stiffness, the average Young's modulus in the linear region is taken as the entry of the 2-D matrix representing elasticity map

138

As shown in Figure 5.3, the traditional way of stiffness determination by fitting the experimental force curve with Hertz model can give erroneous results, particularly over large indentations. When the upper bound of the fitting region is small, the fitting is of good quality as indicated by the overlap of fitting curve with experimental curve and relatively constant pointwise Young's modulus as shown in Figure 5.3. When the upper bound of the fitting region exceeds a certain point, around 450 nm in this case, the fitting is of bad quality and nonlinearity emerges, as indicated by the disagreement of the fitting curve with the experimental data in Figure 5.3a and increase in pointwise Young's modulus in Figure 5.3b. The pointwise Young's modulus curve consists of linear and nonlinear regimes, with the transition marks the onset of nonlinearity in mechanical properties and assumes a indentation value around 450 nm in this example shown in Figure 5.3. The results demonstrate a nonlinearity in cell biomechanics, which has been reported for other biomaterials [59], as well as for homogeneous polymers [26].

### 5.4.2   *Cells are mechanically heterogeneous and show spatial variation in elasticity*

Following the methods described above, the result of force mapping on a HEY A8 single cell was obtained by AFM and shown below in Figure 5.4.

139
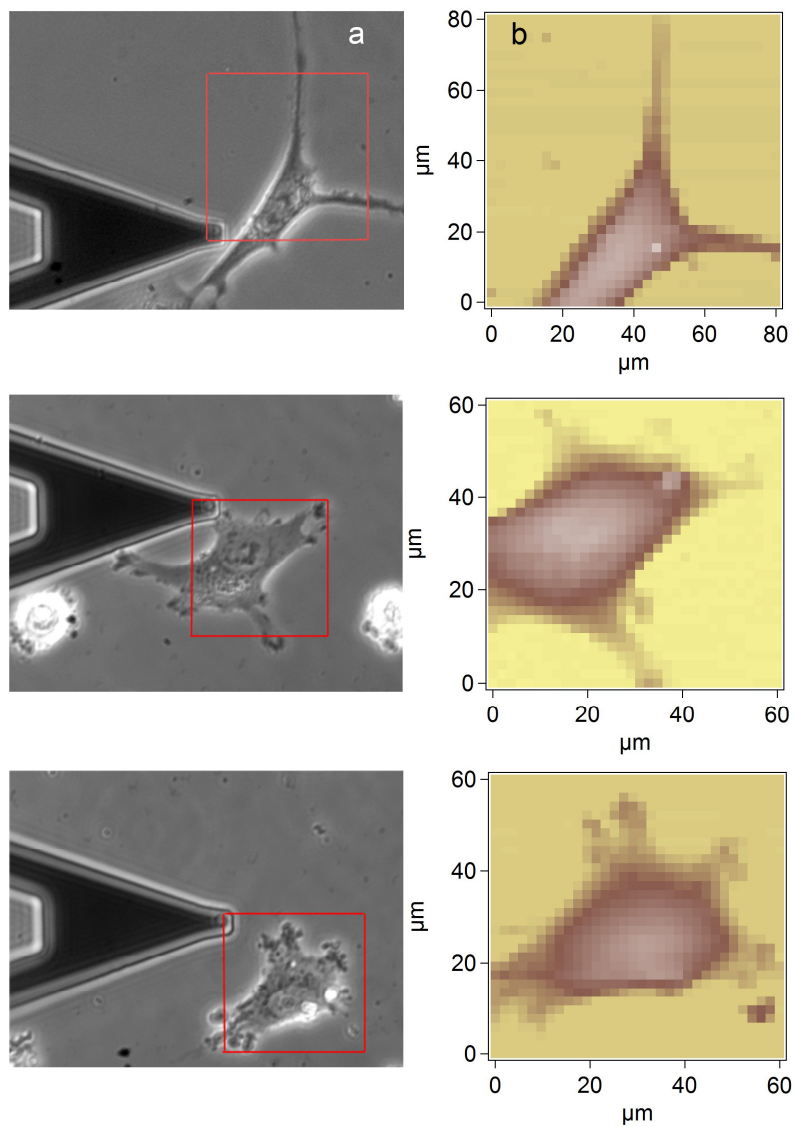
Figure 5.4: Force map of HEY A8 single cells, a) phase contrast microscopy shows the nucleus, the red box is the scanned region, and b) 2-D representation of the scanned topography

Individual force curve at each pixel was analyzed using the pointwise Hertzian method and the corresponding pointwise Young's modulus was calculated as a function of indentation. The average Young's modulus in the linear elasticity region was taken as the corresponding entry of the matrix representing the elasticity map. The elasticity map and

topography were feed into customized MATLAB routines for interpolation excluding the

edge of the cell, the 2-D map of the linear elasticity is shown below in Figure 5.5.
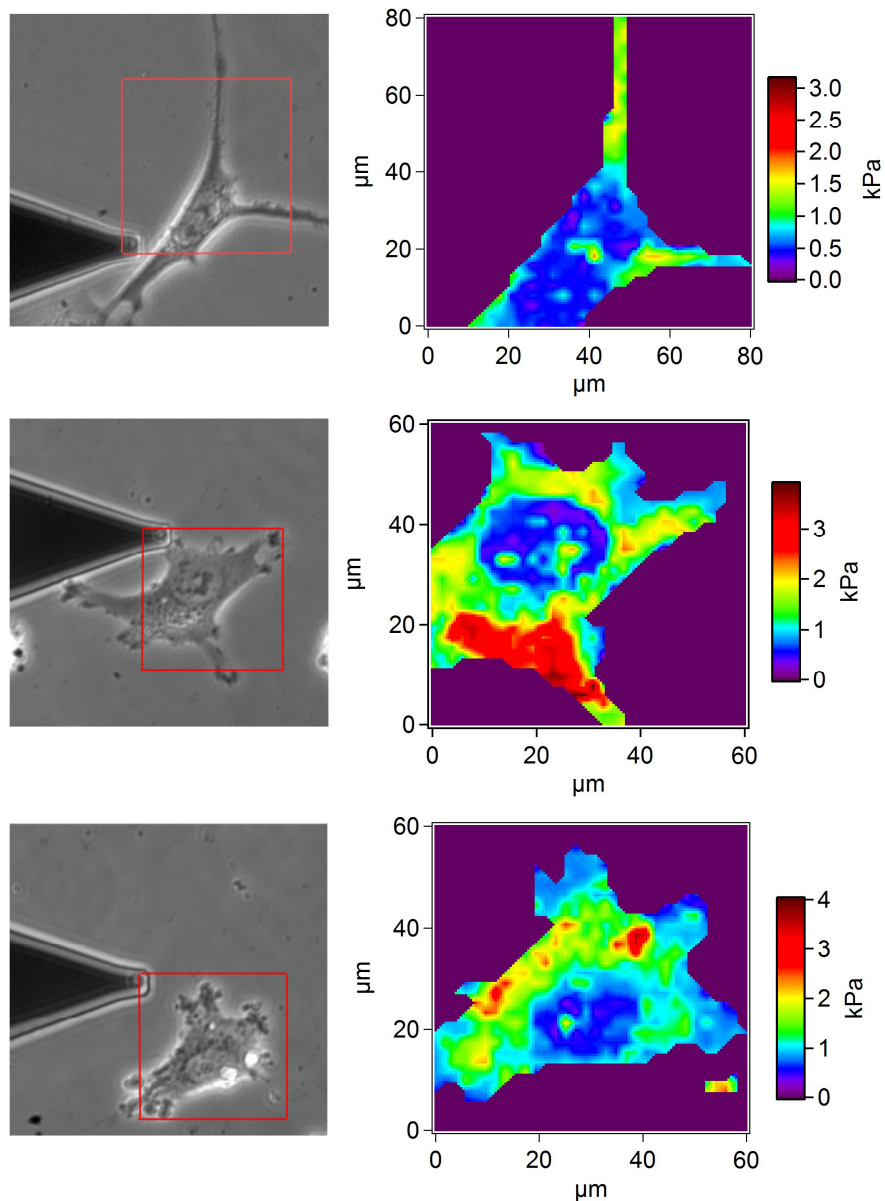
Figure 5.5: The map of linear elasticity of a HEY A8 single cell, columns from left to right: topography and moduli map. The nuclear region is softer than the surrounding cytoplasm by 60-90%.

5.4.3 Correction of elasticity map by integrating sample surface curvature

In the cell mechanics measurements, the surface of cell sample is usually assumed flat and the effective radius of curvature is simply replaced by the radius of indentor. This assumption is reasonable in the case of the whole cell mechanics because the surface curvature at the contact point at the center of the cell is much lower than the indentor. In the case of cell elasticity mapping, this assumption, however, is questionable because the surface curvature is no longer negligible at some locations, especially at the edges of a single cell. Therefore, it's necessary to incorporate the surface curvature of cell sample into the determination of elasticity map.

We utilize the surface topography obtained during force mapping to determine the surface curvature of the sample for each pixel. First, the radius of curvature at each indentation location was calculated in x and y directions, at the i_{th} indentation location, the radius of curvature R_x was the radius of circle uniquely determined by three consecutive data points (x_{i-1}, z_{i-1}), (x_i, z_i), and (x_{i+1}, z_{i+1}) in x direction in the topography matrix, and R_y by (y_{j-1}, z_{j-1}), (y_j, z_j), and (y_{j+1}, z_{j+1}) in y direction in the same manner. Where x and y denote the location and z is the height of the cell surface at this location in the topography matrix. The sample surface curvature was then determined by $1/R_s= (1/R_x+1/R_y)/2$ at each location and then assembled into a matrix according to the spatial arrangement of these locations. The effective radius was then calculated using $1/R=1/R_s+1/R_{indentor}$ with $R_{intentor}$ as the radius of indentor, then the corresponding elasticity map was determined. The corrected elasticity maps of the samples in Figure 5.5 after interpolation were shown below in Figure 5.6, cross section profiles of the elasticity maps were also plotted and compared against each other.
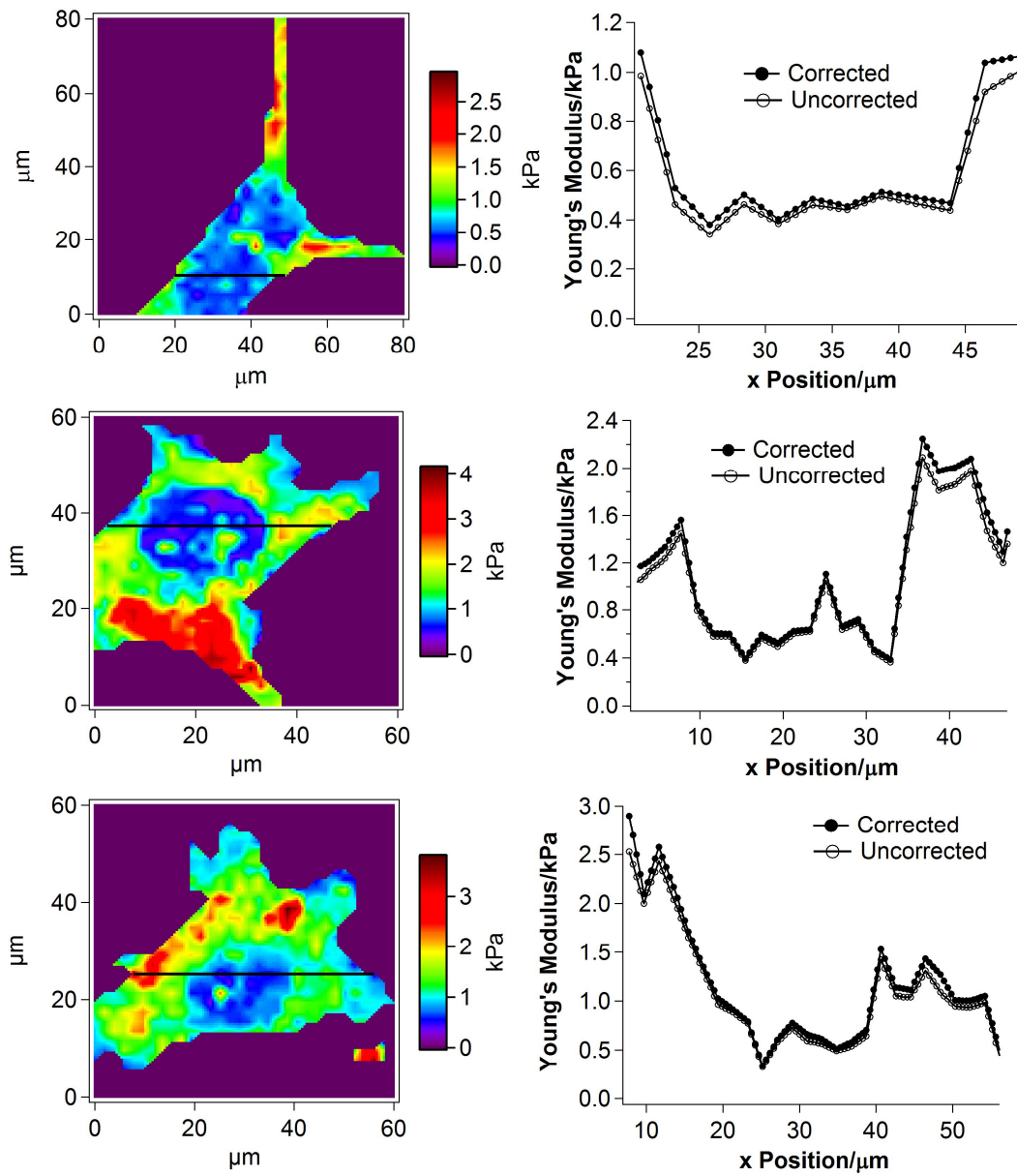
Figure 5.6: Corrected elasticity maps and comparison to uncorrected maps as in Figure 5.5, left column: elasticity map after factoring in surface curvature; right column: examples of cross section profiles (along the black line in the corresponding elasticity map) of corrected and uncorrected elasticity maps.

From Figure 5.5 and 5.6, we can conclude that the sample surface curvature in our

experiments plays a role in the determination of stiffness, especially at the edges of cells.

At the center of the sample, the sample surface curvature is negligible compared to the

143

indentor, therefore replacing the effective radius of curvature with the radius of indentor doesn't impact the result significantly. At the edges, however, the radius of curvature of the cell surface is comparable to the indentor and therefore has to be taken into account to correctly predict the Young's modulus at these locations. For example, the minimum radius of curvature of the surface along the cross section line in the middle graph of Figure 5.6 is 6.78 µm. All elasticity maps shown hereafter were calculated after including the effect of sample surface curvature.

The elasticity maps in Figure 5.5 and 5.6 display strong spatial variations and indicates that mechanical stiffness of the HEY A8 single cell is highly heterogeneous. The central region corresponding to the nucleus, as shown in the phase contrast microscopy in Figure 5.4, shows lower Young's moduli than other parts. It's worth noting that within the nuclear region in the elasticity map, the stiffness distribution is also heterogeneous with a variation of Young's moduli of 1.6 kPa, 1.7kPa and 1.9 kPa for the top, middle and bottom graph in Figure 5.6, respectively. These stiffer locations likely correspond to the tightly packed chromatins or heterochromatin inside the nucleus, as has been shown in previous studies that heterochromatin is less deformable than the loosely packed euchromatin in stem cell and model system [29, 60].

The cytoplasmic region surrounding the nucleus has higher moduli than the nuclear region in the HEY A8 cells. The Young's modulus of the cell exhibits less variation in the thick parts of the cells (differs by less than 2 kPa), but does increase dramatically at the cell edge. The cortical regions show very high Young's moduli up to around 4.2 kPa at locations where cells stretch over the surface of the glass substrate.

5.4.4 Confocal microscopy reveals the structural contribution of nucleus and cytoplasm

From results shown above, the Young's modulus across the nucleus is lower than moduli above the cytoplasm, for example, the difference reaches up to 3.44 kPa for the bottom graph in Figure 5.6. While the difference in stiffness is consistent with the cellular structure shown in phase contrast microscopy, it remains unclear the degree which the nucleus contributes to the local stiffness. As we conduct force mapping across the nuclear region, the mechanical properties will be contributed to by both the nucleus and the cytoplasm. To this end, the cellular structure of HEY A8 cells was analyzed, through staining and confocal microscopy of the actin cytoskeleton and nucleus of individual cells. From these images, the 3-D structure was obtained and representative images are displayed in Figure 5.7. The nucleus is blue and actin cytoskeleton is red under the fluorescence.
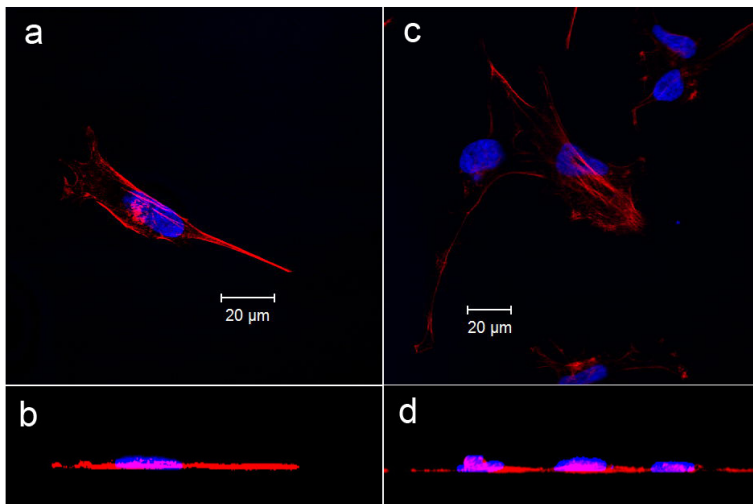
Figure 5.7: Confocal microscopy display nucleus and F-actin of HEY A8 cells, a) top view of a single cell, b) side view of the single cell, c) tope view of a cell cluster, and d) side view of the cell cluster. It is seen that the nucleus contributes to most of the volume in the perinuclear region of adherent HEY A8 cells.

145

From the 3-D cellular structure of the HEY A8 cells, the nucleus and actin cytoskeleton was observed to be flattened in our experiment, with the actin cytoskeleton stress fibers clearly visible spread over the extended cytoplasm and the nucleus as a flattened ellipse. From the side view, the thickness of the nucleus is higher than the thickness of the actin cytoskeleton layer, and there is little F-actin present above the nucleus. The cellular structures observed in confocal images are consistent with that observed in AFM topography. The elasticity maps show the softened region of the cell are consistent with the dimensions of the nuclear region.

The AFM stiffness measured above the nuclear region results from a convolution of the material properties of the nucleus and the cytoplasm. To extract the stiffness values of the nucleus and cytoplasm separately, we must determine the thickness of each from the confocal images. The stained cells were visualized by confocal microscopy and shown in Figure 5.8.
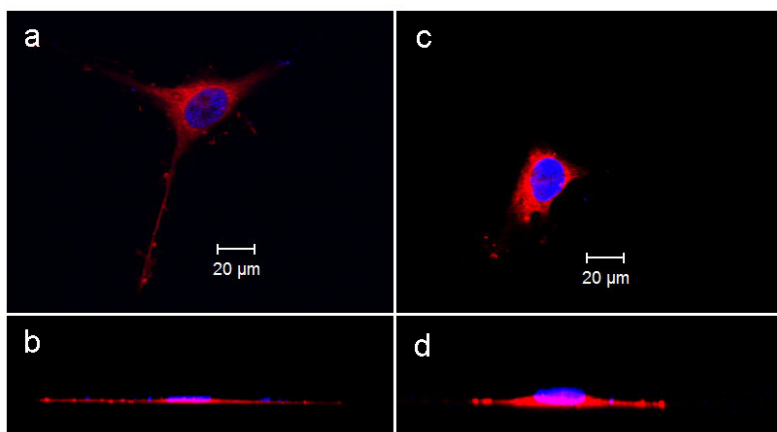
Figure 5.8: Confocal microscopy of nucleus and cell membrane of HEY A8 single cells, top: top view; bottom: side view

From Figure 5.8, the cell body over the nuclear region is primarily occupied by the nucleus in HEY A8 single cells, therefore indentations over the nuclear region of HEY A8 cells are almost equal to penetrations into the nucleus and we can treat the cellular material to be nuclear. From the analysis of mechanics at specified indentations, the softer region in the elasticity map primarily reflects the softness of the nucleus for the indentation depths much larger than the thickness of the cytoplasm region. The elasticity map, together with the confocal microscopy and phase contrast images showed that nucleus is softer than the surrounding cytoplasm in HEY A8 cells.

The values of the modulus obtained for the nucleus using the indentation-dependent elasticity maps are comparable to nuclear stiffness measurements by several groups using a variety of techniques. Depending on cell type, measurement techniques and conditions, nucleus has displayed a wide range of stiffness. Deguchi found that isolated endothelial nucleus is 0.62 kPa in stiffness using micropipette aspiration [61], the same method used by Nathalie determined that endothelial nucleus is 5 kPa when intact and is 8 kPa when isolated [27]. Guilak demonstrated that chondrocyte nucleus is approximately 1 kPa in Young's modulus [62]. de Vries observed that elasticity of intact HeLa nucleus is 0.25 kPa using magnetic tweezers [63]. While various techniques have been developed to elucidate the role of nuclear mechanics in the cancer cell migration [28, 45, 52, 53], our direct observation of spatial mechanical properties of intact nuclei of invasive ovarian cancer HEY A8 cells provides insightful mechanical and structural information under realistic physiological and biological conditions.

For the HEY A8 cells in our experiments, the fact that nucleus is in general softer than the cytoplasm is consistent with the role of nucleus in cancer and metastasis. Nucleus in

cancer cells displays a ruptured and less organized structure [45] and therefore results in a modified mechanical stiffness upon malignancy. In addition, the deformation of the nucleus is also a critical step, and possibly the rate-limiting factor [53, 64, 65] of cancer cell migration [55, 66]. Cells with softer nuclei are therefore easier to migrate through small confines and our results are consistent with this fact. To further elucidate the role of nuclear stiffness in metastasis, the methodology has to be applied to other types of ovarian cancer such as IOSE and HEY cells, since these cell types have demonstrated distinct metastatic potentials [67].

5.4.5 *Young's modulus in the lamellipodia region show a power law thickness-dependence*

The Young's modulus in Figure 5.5 revealed extremely high values at locations where cells crawl and spread over the glass substrate. If we examine points along a radial axis line and plot the measured stiffness versus cell thickness at these points, it's clear that there exists a negative correlation between Young's modulus and local thickness at the cell edge.
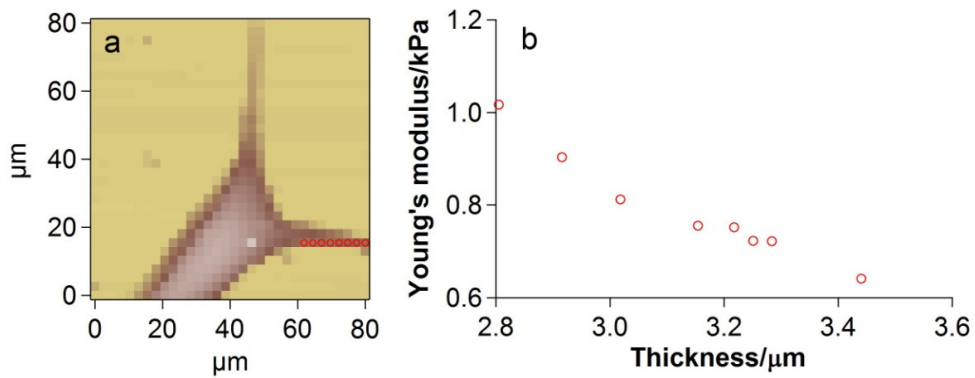
Figure 5.9: The cell displays a negative correlation between Young's modulus and thickness at some locations (denoted by markers). a) 2-D representation of scanned topography, and b) Young's modulus versus thickness

The correlation of the pointwise modulus in the linear mechanical regime and thickness in the cortical region of HEY A8 cells is similar to that observed in PDMS ultrathin films in chapter 4. In our studies of PDMS, geometry plays a significant role in mechanics. To examine whether a similar relationship is observed in lamellipodia, the topography and elasticity maps of additional cells are shown in Figure 5.10.
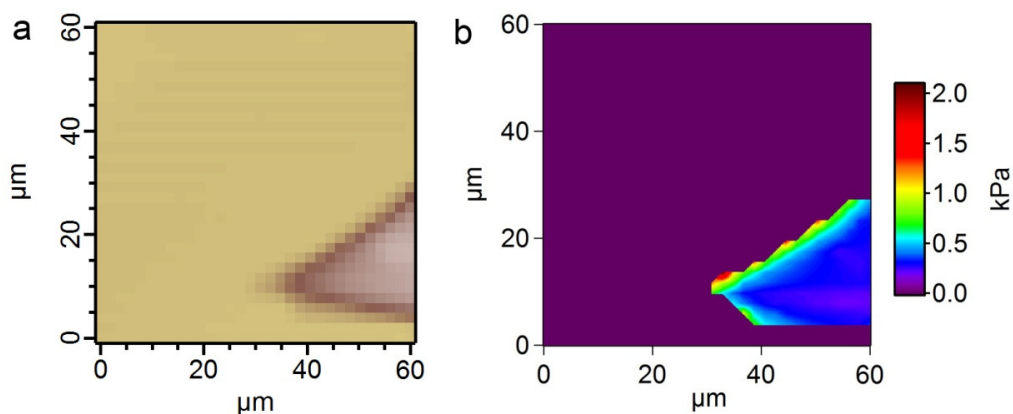
Figure 5.10: Elasticity map of the cortical region of a HEY A8 cell, a) 2-D representation of the scanned topography, and b) elasticity map of the scanned region

The sample shown in Figure 5.10 demonstrates that the Young's modulus is higher at the cell edge than at locations near the center of the cell. To quantitatively explore the relationship, we plot the Young's modulus versus thickness at different locations as shown in Figure 5.11. As the indentor diameter (4.74 µm) is larger than the pixel size (1.875 µm), pixels at the cell boundary were not included in the analysis.
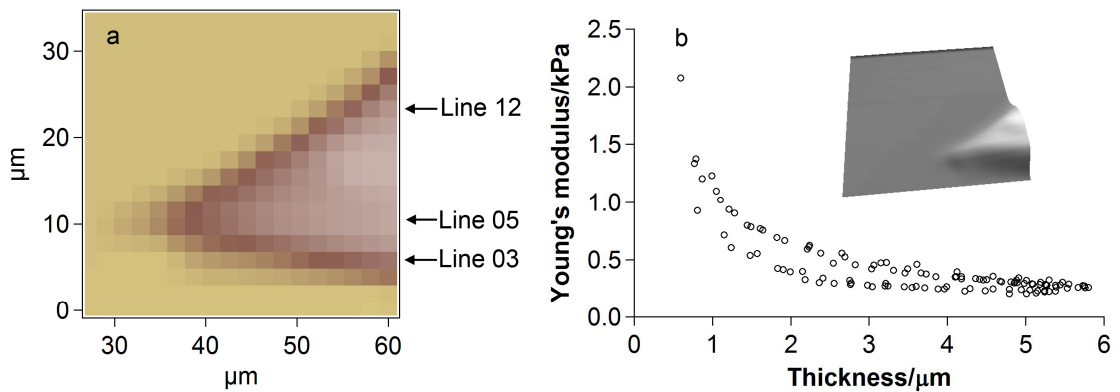
Figure 5.11: Young's modulus versus thickness for cortical region of a HEY A8 cell, a) scanned topography with critical line numbers, and b) Young's modulus versus thickness for data points on line 03 to line 12, the inset of b shows the topography of the region

The Young's modulus of the cortical region, as shown in Figure 5.11, is inversely correlated with thickness—thinner regions are stiffer. Fitting the data with power law relationship gives a dependence of the form (thickness/µm)$^{-1}$, however, it's clear that the data points split into two groups with each following different relationships. Data points along line 03-05 and along line 06-12 were plotted and analyzed separately; the results with the fitting power relationships are shown in Figure 5.12.

The strong correlation between stiffness and thickness in our experiments, together with our previous study on PDMS in chapter 4, suggest the significant role of geometry in thin film polymer mechanics in general, and cell mechanics in particular. Many factors may impact the measurement and interpretation of the results. In these HEY A8 cells, the power law correlation assumes different forms for different regions as shown in Figure 5.12. The first region is bounded by line 3 and line 5, while the second one bounded by line 6 and line 12, these two regions show different topographical or geometrical characteristics as shown in the inset of Figure 5.11. Specific contributions to the power law relationship are likely determined by differences in cytoplasmic components and the state of the components.
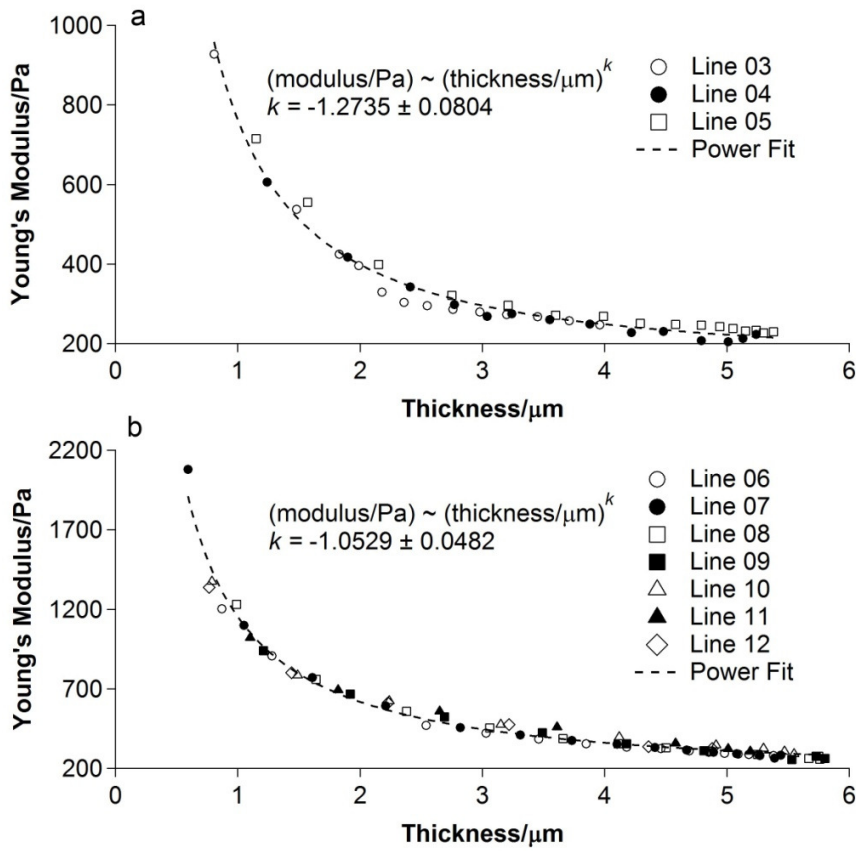
Figure 5.12: The data points follow two power relationships, a) data points on line 03-05, and b) data points on line 06-12. The positions of these lines are shown in Figure 5.11

5.4.6 Contractility contributes to stiffness but not the determinant of stiffening of the edge

Having established the correlation between stiffness and cell thickness in HEY A8 cells, and demonstrated strong spatial variations in elasticity in the cytoplasm region, which can change by more than 2 kPa, the reason for this dependence remains unclear. While there are many factors might cause the variation, such as material and geometric effects [26], contractility has known to contribute to stiffening in single cells [68-70] and therefore might affect the dependence. Increased contractility at the edges of cells [69-71] may contribute to the stiffening observed in our measurements. To evaluate the relative

contribution of contractility on our results, we used chemical treatments to reduce cytoskeletal tension, and observed the effects on thickness-dependent cell stiffness. ROCK inhibitor Y-27632 was added to inhibit the actomyosin contractility *via* Rho pathway, and subsequent AFM stiffness measurements were conducted. The elasticity maps after treatment with Y-27632 of different concentration were shown in Figure 5.13 and Figure 5.14.
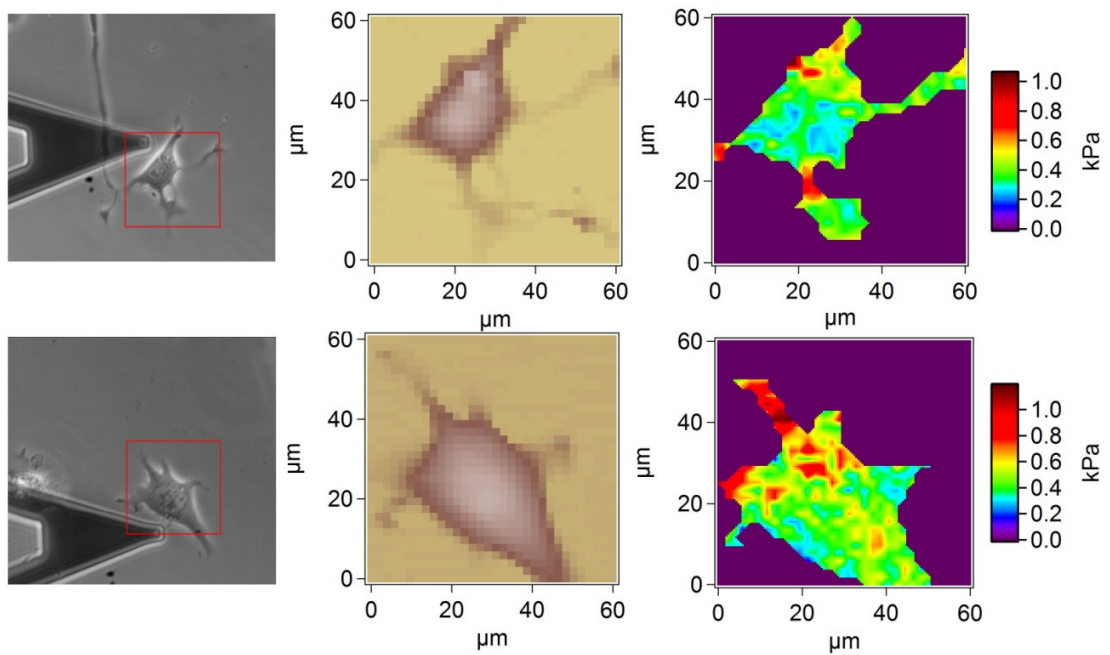
Figure 5.13: Elasticity map of HEY A8 single cells treated with 50 µM Y-27632, from left to right in each row: phase contrast images, topography, and elasticity map
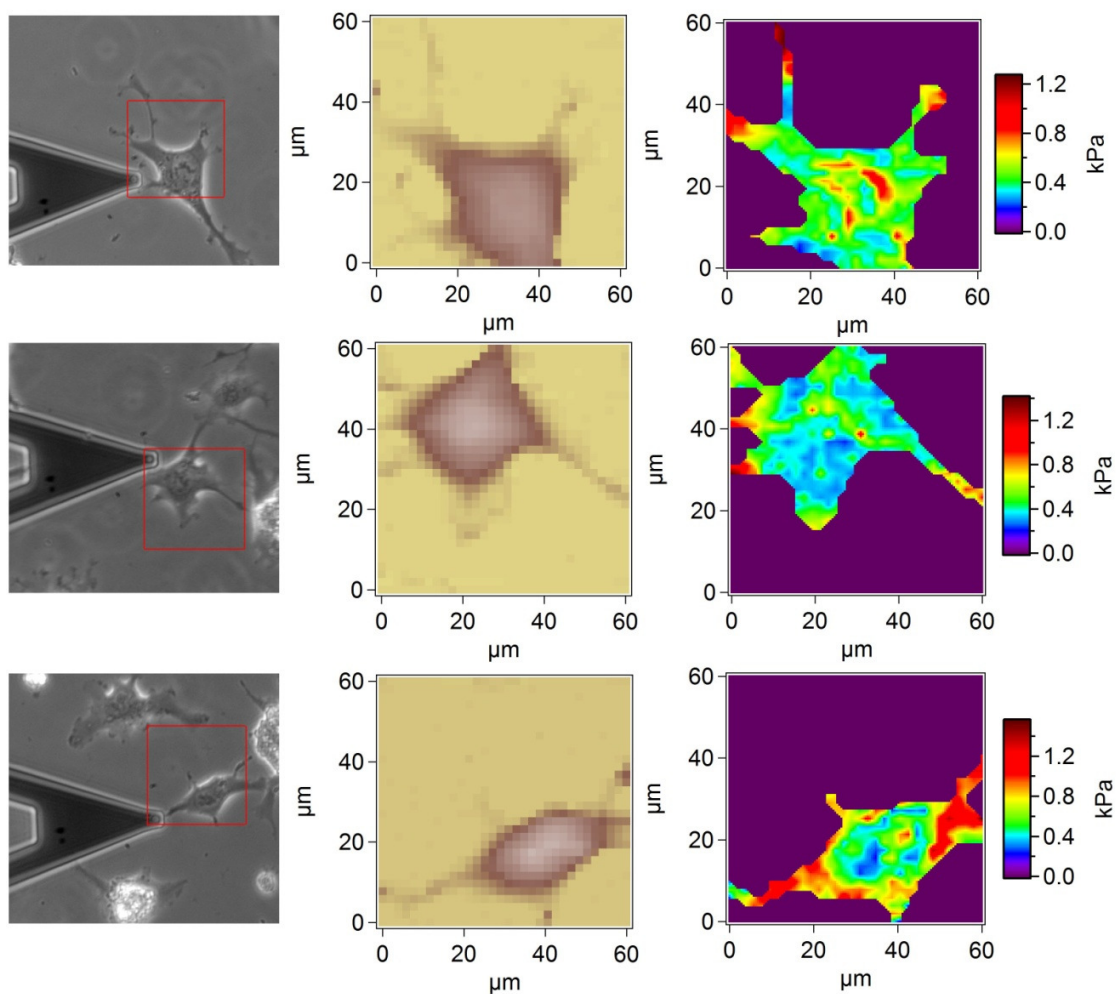
Figure 5.14: Elasticity map of single cells treated with 100 µM Y-27632, from left to right in each row: phase contrast images, topography, and elasticity map

Inhibition of actomyosin contractility subsequently reduced the stiffness of HEY A8 cells, as shown in Figure 5.13 and Figure 5.14, and increasing concentration of Y-27632 from 50 µM to 100 µM doesn't reduce the stiffness of HEY A8 cells further. Therefore 50 µM was deemed sufficient to inhibit actomyosin contractility *via* Rho pathway in our experiments. Upon the inhibition, stiffness of HEY A8 cells in the cortical region decreased by 1 kPa on average to 1.3 kPa. The stiffness of the nuclear region, in contrast, did not undergo appreciable changes, indirectly supporting our previous conclusion that

cytoplasmic F-actin contributes little to the measured cell stiffness above the nucleus. As a result, the nuclei are not distinguishable in the elasticity maps of HEY A8 cells treated with Y-27632 (there is a vestigial nuclear stiffness effect observed in one cell displayed in Figure 5.14c, though the effect is vastly reduced), implying the strong contribution of actomyosin contractility to cellular stiffness in the lamellipodia and cytoplasm. It's known that this contraction force, sometimes called prestress, increases the stiffness of single cells [68, 70]. The distribution pattern of Young's modulus in the cortical region in our experiment is similar to that of contraction force field exerted by single cells [71].

After inhibition of actomyosin contractility, force mapping of 16×16 was conducted over an area of 30×30 µm in the cortical region free of mechanical interference from nucleus, the same method was used to analyze the correlation between stiffness and sample thickness, with the results plotted in Figure 5.15 along with the scanned topography.
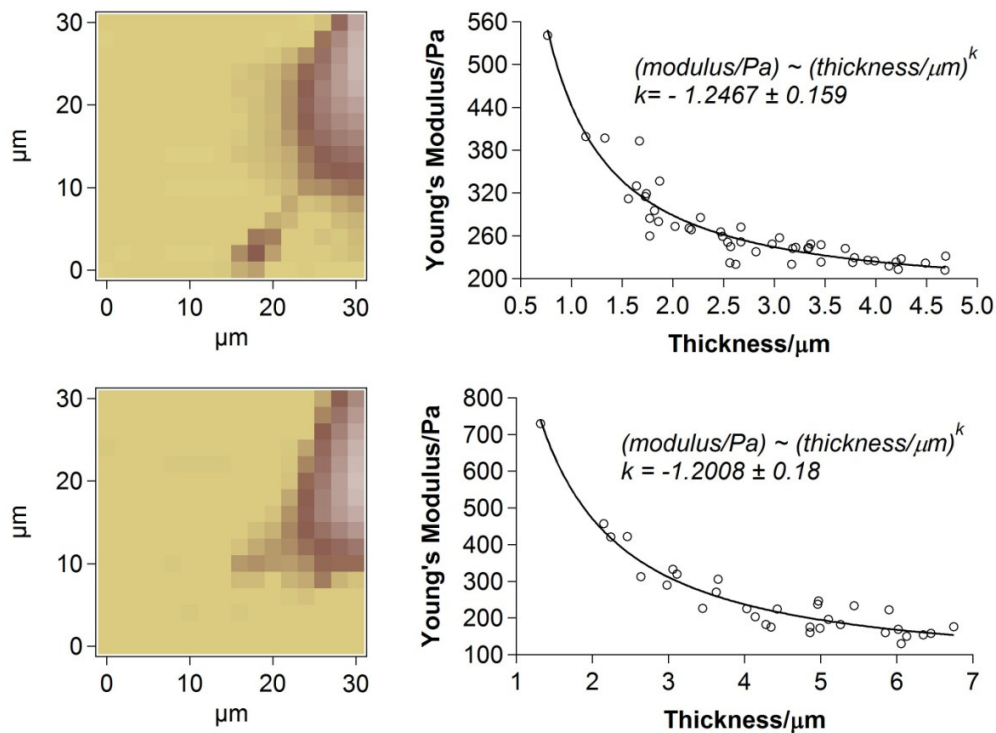
Figure 5.15: Young's modulus versus thickness for lamellipodia region of HEY A8 single cells after treatment with Y-27632

From the analysis of stiffness over the cortical region in Figure 5.15, stiffness still strongly depends on sample thickness after inhibition of actomyosin contractility *via* Rho Pathway. The stiffness decreased on average as compared to that without inhibition shown in Figure 5.12, though the data points scatter to a larger extent compared to untreated sample in Figure 5.10, they can still be fitted with power law relationships $E \sim t^k$ of good quality, where E is the modulus in Pascal and t is the thickness in µm. Therefore, actomyosin prestress provides an important contribution to the modulus of the cell, but it does not account to the observed power law dependence on cell thickness. We hypothesize that, similar to PDMS polymers, the geometry is an important (if not the

only) factor contributing to the thickness-dependent stiffening of HEY A8 single cells in the cortical region.

The stiffening phenomena we observed here in cortical regions of HEY A8 cells, together with the PDMS system discussed in chapter 4, implies the significant role of geometry in stiffness measurement on the micro and nanoscale. The impact of finite thickness and geometry confinement has been studied in other material systems [72-76] and tackled by different theoretical models [77-81], from which it's easy to conclude that the Young's modulus calculated by Hertz model in this confined system is negatively correlated with sample thickness.

The data presented above demonstrate an interesting phenomenon similar to what we observed in ultrathin film PDMS system [26], the linear elasticity, as obtained by pointwise Hertzian model, shows a strong dependence on sample thickness. The sample mechanically resembles simple hyperelastic polymers in the sense that it displays strong stiffening phenomenon as sample thickness decreases. This resemblance might also reveal the structural information of single cells, link cell mechanics to materials science, and improve our understanding of single cell mechanics from the materials science perspective.

5.5   Summary and conclusion

In this chapter, we described the combination of pointwise Hertzian model and standard force mapping with AFM. Using this systematic approach, we explored the spatial elasticity distribution of single cells from HEY A8, and demonstrated that the stiffness of these cells is highly heterogeneous. The nucleus is much softer than the surrounding cytoplasm parts, and there exists a strong stiffening phenomenon in the cortical region

with stiffness displays a strong dependence on sample thickness. The correlation between elasticity and sample thickness still exists after treatment with ROCK inhibitor, suggesting that stiffening is at least in part ascribable to geometry confinement, which might also play a significant role in the mechanics of other material systems.

The results shown here demonstrated the efficacy of pointwise Hertzian model in cell mechanics study with AFM, the heterogeneity of mechanical properties could be difficult to detect and ignored otherwise. The application of this systematic approach to HEY A8 cells revealed the softness of the nucleus, in addition, the mechanical stiffening revealed the resemblance between the cortical region and the simple hyperelastic material PDMS, which suggests the possibility of modeling the cortical region of single cells as a simple polymeric material. The long range heterogeneity at the cellular level and the strong geometry confinement effect in the cortical region together provide a new insight into the structural and mechanical properties of single cells from the material science perspective.

5.6   References

1.   Hoffman, B.D. and J.C. Crocker, *Cell Mechanics: Dissecting the Physical Responses of Cells to Force.* Annual Review of Biomedical Engineering, 2009. **11**(1): p. 259-288.

2.   Lim, C.T., E.H. Zhou, and S.T. Quek, *Mechanical models for living cells—a review.* Journal of biomechanics, 2006. **39**(2): p. 195-216.

3.   Humphrey, J.D., *Review Paper: Continuum biomechanics of soft biological tissues.* Proceedings of the Royal Society of London. Series A: Mathematical, Physical and Engineering Sciences, 2003. **459**(2029): p. 3-46.

4.   Johnson, K.L., *Contact mechanics.* 1985, Cambridge, UK: Cambridge university press.

5.   Unnikrishnan, G.U., V.U. Unnikrishnan, and J.N. Reddy, *Constitutive Material Modeling of Cell: A Micromechanics Approach.* Journal of Biomechanical Engineering, 2007. **129**(3): p. 315-323.

6.   Wang, N., et al., *Mechanical behavior in living cells consistent with the tensegrity model.* Proceedings of the National Academy of Sciences, 2001. **98**(14): p. 7765-7770.

7.   Ingber, D.E., *Tensegrity I. Cell structure and hierarchical systems biology.* Journal of Cell Science, 2003. **116**(7): p. 1157-1173.

8.   Ingber, D.E., *Cellular tensegrity: defining new rules of biological design that govern the cytoskeleton.* Journal of Cell Science, 1993. **104**(3): p. 613-627.

9.   Yeung, A. and E. Evans, *Cortical shell-liquid core model for passive flow of liquid-like spherical cells into micropipets.* Biophysical Journal, 1989. **56**(1): p. 139-149.

10.   Dong, C., R. Skalak, and K.L. Sung, *Cytoplasmic rheology of passive neutrophils.* Biorheology, 1991. **28**(6): p. 557-567.

11.   Tsai, M.A., R.S. Frank, and R.E. Waugh, *Passive mechanical behavior of human neutrophils: power-law fluid.* Biophysical Journal, 1993. **65**(5): p. 2078-2088.

12.   Mow, V.C., et al., *Biphasic Creep and Stress Relaxation of Articular Cartilage in Compression: Theory and Experiments.* Journal of Biomechanical Engineering, 1980. **102**(1): p. 73-84.

13.   Shin, D. and K. Athanasiou, *Cytoindentation for obtaining cell biomechanical properties.* Journal of Orthopaedic Research, 1999. **17**(6): p. 880-890.

14.   Johnson, K.L., K. Kendall, and A.D. Roberts, *Surface Energy and the Contact of Elastic Solids.* Proceedings of the Royal Society of London. A. Mathematical and Physical Sciences, 1971. **324**(1558): p. 301-313.

15.   Grierson, D.S., E.E. Flater, and R.W. Carpick, *Accounting for the JKR-DMT transition in adhesion and friction measurements with AFM.* Journal of Adhesion Science and Technology, 2005. **19**(3-5): p. 291-311.

16.   Radmacher, M., et al., *Measuring the viscoelastic properties of human platelets with the atomic force microscope.* Biophysical Journal, 1996. **70**(1): p. 556-567.

17.   Suresh, S., *Biomechanics and biophysics of cancer cells.* Acta Materialia, 2007. **55**(12): p. 3989-4014.

18.   Bausch, A.R. and K. Kroy, *A bottom-up approach to cell mechanics.* Nat Phys, 2006. **2**(4): p. 231-238.

19.   Heidemann, S.R. and D. Wirtz, *Towards a regional approach to cell mechanics.* Trends in cell biology, 2004. **14**(4): p. 160-166.

20.   Tseng, Y., T.P. Kole, and D. Wirtz, *Micromechanical mapping of live cells by multiple-particle-tracking microrheology.* Biophysical Journal, 2002. **83**(6): p. 15.

21.   Lammerding, J., et al., *Nuclear Mechanics and Methods*, in *Methods in Cell Biology*, W. Yu‑Li and E.D. Dennis, Editors. 2007, Academic Press. p. 269-294.

22.   Darling, E.M., *Force scanning: a rapid, high-resolution approach for spatial mechanical property mapping.* Nanotechnology, 2011. **22**(17): p. 175707.

23.   RamanA, et al., *Mapping nanomechanical properties of live cells using multi-harmonic atomic force microscopy.* Nat Nano, 2011. **6**(12): p. 809-814.

24.   Fuhrmann, A., et al., *AFM stiffness nanotomography of normal, metaplastic and dysplastic human esophageal cells.* Physical Biology, 2011. **8**(1): p. 015007.

25.   Costa, K.D., A.J. Sim, and F.C.-P. Yin, *Non-Hertzian Approach to Analyzing Mechanical Properties of Endothelial Cells Probed by Atomic Force Microscopy.* Journal of Biomechanical Engineering, 2006. **128**(2): p. 176-184.

26.   Xu, W., N. Chahine, and T. Sulchek, *Extreme Hardening of PDMS Thin Films Due to High Compressive Strain and Confined Thickness.* Langmuir, 2011. **27**(13): p. 8470-8477.

27.   Caille, N., et al., *Contribution of the nucleus to the mechanical properties of endothelial cells.* Journal of biomechanics, 2002. **35**(2): p. 177-187.

28.	Lombardi, M.L. and J. Lammerding, *Chapter 6 - Altered Mechanical Properties of the Nucleus in Disease*, in *Methods in Cell Biology*, G.V. Shivashankar, Editor. 2010, Academic Press. p. 121-141.

29.	Dahl, K.N., A.J.S. Ribeiro, and J. Lammerding, *Nuclear Shape, Mechanics, and Mechanotransduction.* Circulation Research, 2008. **102**(11): p. 1307-1318.

30.	Crisp, M., et al., *Coupling of the nucleus and cytoplasm: role of LINC complex.* The Journal of Cell Biology, 2006. **172**(1): p. 41-53.

31.	Maniotis, A.J., C.S. Chen, and D.E. Ingber, *Demonstration of mechanical connections between integrins, cytoskeletal filaments, and nucleoplasm that stabilize nuclear structure.* Proceedings of the National Academy of Sciences, 1997. **94**(3): p. 849-854.

32.	Lombardi, M.L., et al., *The Interaction between Nesprins and Sun Proteins at the Nuclear Envelope Is Critical for Force Transmission between the Nucleus and Cytoskeleton.* Journal of Biological Chemistry, 2011. **286**(30): p. 26743-26753.

33.	Crisp, M. and B. Burke, *The nuclear envelope as an integrator of nuclear and cytoplasmic architecture.* FEBS Letters, 2008. **582**(14): p. 2023-2032.

34.	Chen, C.S. and D.E. Ingber, *Tensegrity and mechanoregulation: from skeleton to cytoskeleton.* Osteoarthritis and Cartilage, 1999. **7**(1): p. 81-94.

35.	Martins, R.P., et al., *Mechanical Regulation of Nuclear Structure and Function.* Annual Review of Biomedical Engineering, 2012. **14**(1): p. 431-455.

36.	Burke, B. and C.L. Stewart, *The Laminopathies: The Functional Architecture of the Nucleus and Its Contribution to Disease*.* Annual Review of Genomics and Human Genetics, 2006. **7**(1): p. 369-405.

37.	Lammerding, J., et al., *Abnormal nuclear shape and impaired mechanotransduction in emerin-deficient cells.* The Journal of Cell Biology, 2005. **170**(5): p. 781-791.

38.	Gotzmann, J. and R. Foisner, *A-type lamin complexes and regenerative potential: a step towards understanding laminopathic diseases?* Histochemistry and Cell Biology, 2006. **125**(1): p. 33-41.

39.   Capell, B.C. and F.S. Collins, *Human laminopathies: nuclei gone genetically awry.* Nat Rev Genet, 2006. **7**(12): p. 940-952.

40.   Burke, B. and C.L. Stewart, *Life at the edge: the nuclear envelope and human disease.* Nat Rev Mol Cell Biol, 2002. **3**(8): p. 575-585.

41.   Iwaya, K., et al., *Cytoplasmic and/or nuclear staining of beta-catenin is associated with lung metastasis.* Clinical and Experimental Metastasis, 2003. **20**(6): p. 525-529.

42.   Manelli-Oliveira, R. and G. Machado-Santelli, *Cytoskeletal and nuclear alterations in human lung tumor cells: a confocal microscope study.* Histochemistry and Cell Biology, 2001. **115**(5): p. 403-411.

43.   Caspersson, T., et al., *Cytochemical changes in the nucleus during tumour development.* The Histochemical Journal, 1983. **15**(4): p. 337-362.

44.   Dey, P., *Cancer nucleus: Morphology and beyond.* Diagnostic Cytopathology, 2010. **38**(5): p. 382-390.

45.   Zink, D., A.H. Fischer, and J.A. Nickerson, *Nuclear structure in cancer cells.* Nat Rev Cancer, 2004. **4**(9): p. 677-687.

46.   Moss, S.F., et al., *Decreased and aberrant nuclear lamin expression in gastrointestinal tract neoplasms.* Gut, 1999. **45**(5): p. 723-729.

47.   Coradeghini, R., et al., *Differential expression of nuclear lamins in normal and cancerous prostate tissues.* Oncology Reports, 2006. **15**(3): p. 5.

48.   Broers, J.L., et al., *Nuclear A-type lamins are differentially expressed in human lung cancer subtypes.* The American Journal of Pathology, 1993. **143**(1): p. 10.

49.   Willis, N.D., et al., *Lamin A/C Is a Risk Biomarker in Colorectal Cancer.* PLoS ONE, 2008. **3**(8): p. e2988.

50.   Hudson, M.E., et al., *Identification of differentially expressed proteins in ovarian cancer using high-density protein microarrays.* Proceedings of the National Academy of Sciences, 2007. **104**(44): p. 17494-17499.

51.   Bissell, M.J., et al., *Tissue Structure, Nuclear Organization, and Gene Expression in Normal and Malignant Breast.* Cancer Research, 1999. **59**(7 Supplement): p. 1757s-1764s.

52.   Wolf, K. and P. Friedl, *Molecular mechanisms of cancer cell invasion and plasticity.* British Journal of Dermatology, 2006. **154**: p. 11-15.

53.   Wolf, K., et al., *Multi-step pericellular proteolysis controls the transition from individual to collective cancer cell invasion.* Nat Cell Biol, 2007. **9**(8): p. 893-904.

54.   Friedl, P., K. Wolf, and J. Lammerding, *Nuclear mechanics during cell migration.* Current Opinion in Cell Biology, 2011. **23**(1): p. 55-64.

55.   Yamauchi, K., et al., *Real-time In vivo Dual-color Imaging of Intracapillary Cancer Cell and Nucleus Deformation and Migration.* Cancer Research, 2005. **65**(10): p. 4246-4252.

56.   Vaziri, A. and M.R.K. Mofrad, *Mechanics and deformation of the nucleus in micropipette aspiration experiment.* Journal of biomechanics, 2007. **40**(9): p. 2053-2062.

57.   Rowat, A.C., et al., *Towards an integrated understanding of the structure and mechanics of the cell nucleus.* BioEssays, 2008. **30**(3): p. 226-236.

58.   Hutter, J.L. and J. Bechhoefer, *Calibration of atomic-force microscope tips.* Review of Scientific Instruments, 1993. **64**(7): p. 1868-1873.

59.   Mahaffy, R.E., et al., *Quantitative Analysis of the Viscoelastic Properties of Thin Regions of Fibroblasts Using Atomic Force Microscopy.* Biophysical Journal, 2004. **86**(3): p. 1777-1793.

60.   Pajerowski, J.D., et al., *Physical plasticity of the nucleus in stem cell differentiation.* Proceedings of the National Academy of Sciences, 2007. **104**(40): p. 15619-15624.

61.   Deguchi, S., et al., *Flow-induced hardening of endothelial nucleus as an intracellular stress-bearing organelle.* Journal of biomechanics, 2005. **38**(9): p. 1751-1759.

62.   Guilak, F., J.R. Tedrow, and R. Burgkart, *Viscoelastic Properties of the Cell Nucleus.* Biochemical and Biophysical Research Communications, 2000. **269**(3): p. 781-786.

63.   de Vries, A.H.B., et al., *Direct Observation of Nanomechanical Properties of Chromatin in Living Cells.* Nano Letters, 2007. **7**(5): p. 1424-1427.

64.   Beadle, C., et al., *The Role of Myosin II in Glioma Invasion of the Brain.* Molecular Biology of the Cell, 2008. **19**(8): p. 3357-3368.

65.   Schoumacher, M., et al., *Actin, microtubules, and vimentin intermediate filaments cooperate for elongation of invadopodia.* The Journal of Cell Biology, 2010. **189**(3): p. 541-556.

66.   Fu, Y., et al., *Nuclear deformation during breast cancer cell transmigration.* Lab on a Chip, 2012. **12**(19): p. 3774-3778.

67.   Xu, W., et al., *Cell Stiffness Is a Biomarker of the Metastatic Potential of Ovarian Cancer Cells.* PLoS ONE, 2012. **7**(10): p. e46609.

68.   Vichare, S., M.M. Inamdar, and S. Sen, *Influence of cell spreading and contractility on stiffness measurements using AFM.* Soft Matter, 2012. **8**(40): p. 10464-10471.

69.   Nagayama, M., et al., *Contribution of cellular contractility to spatial and temporal variations in cellular stiffness.* Experimental Cell Research, 2004. **300**(2): p. 396-405.

70.   Wang, N., et al., *Cell prestress. I. Stiffness and prestress are closely associated in adherent contractile cells.* American Journal of Physiology - Cell Physiology, 2002. **282**(3): p. C606-C616.

71.   Butler, J.P., et al., *Traction fields, moments, and strain energy that cells exert on their surroundings.* American Journal of Physiology - Cell Physiology, 2002. **282**(3): p. C595-C605.

72.   Dimitriadis, E.K., et al., *Determination of Elastic Moduli of Thin Layers of Soft Material Using the Atomic Force Microscope.* Biophysical Journal, 2002. **82**(5): p. 2798-2810.

73. Santos, J.A.C., et al., *Thickness-corrected model for nanoindentation of thin films with conical indenters.* Soft Matter, 2012. **8**(16): p. 4441-4448.

74. Liu, M., et al., *Thickness-dependent mechanical properties of polydimethylsiloxane membranes* Journal of Micromechanics and Microengineering, 2009. **19**(3): p. 035028.

75. Kovalev, A., et al., *Nanomechanical Probing of Layered Nanoscale Polymer Films With Atomic Force Microscopy.* Journal of Materials Research, 2004. **19**(03): p. 716-728.

76. Akhremitchev, B.B. and G.C. Walker, *Finite Sample Thickness Effects on Elasticity Determination Using Atomic Force Microscopy.* Langmuir, 1999. **15**(17): p. 5630-5634.

77. Hayes, W.C., et al., *A mathematical analysis for indentation tests of articular cartilage.* Journal of biomechanics, 1972. **5**(5): p. 541-551.

78. Dhaliwal, R.S., *Punch problem for an elastic layer overlying an elastic foundation.* International Journal of Engineering Science, 1970. **8**(4): p. 273-288.

79. Chadwick, R.S., *Axisymmetric Indentation of a Thin Incompressible Elastic Layer.* SIAM Journal on Applied Mathematics, 2002. **62**(5): p. 1520-1530.

80. Sneddon, I.N., *The relation between load and penetration in the axisymmetric boussinesq problem for a punch of arbitrary profile.* International Journal of Engineering Science, 1965. **3**(1): p. 47-57.

81. Sneddon, I.N., *Fourier Transforms*. 1951, New York: McGraw-Hill Book Company, Inc.

CHAPTER 6

CONCLUSION AND FUTURE DIRECTIONS

6.1   Conclusions

In this thesis, we have demonstrated that cell stiffness is a biomarker of metastatic potential of *in vitro* ovarian cancer cells. By combining single cell stiffness measurements with atomic force microscopy and *in vitro* migration/invasion assay on healthy and cancerous ovarian cells, we demonstrated the reduction of cell stiffness upon malignancy and increased metastatic potential in ovarian cancer. The alteration of single cell stiffness was attributed to actin-mediated cytoskeletal remodeling as revealed by comparative gene expression profile analysis of two isogenic cell lines. Cytoskeletal structures of different cell lines were visualized using fluorescence imaging, innovatively quantified and correlated with single cell stiffness distributions, further implicating actin-mediated cytoskeletal remodeling in stiffness alteration from the perspective of structure-property relationship. The correlation between stiffness and metastatic potential is also verified in pancreatic cancer cell line AsPC-1. We further show that if we treat the invasive cells with N-acetyl-L-cysteine (NAC) to make them less invasive, the stiffness increased. The results with ovarian and pancreatic cancer cells revealed a correlation between stiffness and metastasis in cancer, and indicated that mechanical stiffness may be a useful biomarker in the development of clinical methods to evaluate the relative metastatic potential of ovarian and perhaps other types of cancer cells.

We have also investigated the nature of the intracellular heterogeneity and mechanical nonlinearity in single cell stiffness. To this end, we developed a methodology to analyze

the mechanical nonlinearity with deformation using a pointwise Hertzian model. We tested the model on ultrathin polydimethylsiloxane (PDMS) films where extremely large strains (greater than 50%) could be achieved. Significant mechanical stiffening due to large strain was observed. An additional stiffening was observed simply due to the geometrical confinement, even at low applied strains. The onset of nonlinearity in mechanical response of the PDMS film occurs at 45% of the film thickness, at which point the effect of stiffening due to a substrate effect emerges. Even at low strains, the Young's modulus also increases with decreasing film thickness, due to geometrical confinement. By applying the pointwise Hertzian method on stiffness measurements with AFM that were collected on living cells, we also investigated the nonlinear and heterogeneous mechanics of single cells. Since single cells are typically attached to stiff substrates during mechanical measurements, these conditions may impact the mechanical response of the single cells during the indentations. Even in natural environments, cells which are confined to narrow spaces may experience heightened mechanical stiffness. Through indentation-dependent force mapping, analysis of the local cell stiffness demonstrated variation in local cell stiffness. The results indicated that the mechanical properties of single cells are highly nonlinear and are dependent upon the subcellular features under the applied force as well as the dimensions of the cellular material.

The research presented in thesis made contributions to the field of cell mechanics from several aspects. Single cell stiffness was identified as a potential biomarker of the metastatic potential in ovarian cancer. This knowledge may be one day useful clinically with the development of rapid biomechanical assaying techniques [1-3]. In addition, new techniques were developed to accurately study the mechanical nonlinearity in a location-

167

specific manner. Finally, a quantitative understanding of the effect of geometry on cell mechanics was found, such that the mechanics was found to increase with a power law relationship with cell thickness.

6.2   Future directions

6.2.1   Overview of future plans

On the basis of the results summarized above, the future research aims at an exact understanding of how pathophysiology modulates cellular mechanics for a variety of processes including cancer metastasis, epithelial to mesenchymal transition (EMT), stem cell differentiation, immune activation, and wound healing. We have determined the genes and gene networks that are modified during ovarian metastatic cellular development and highlighted a list that are likely relevant to mechanics. Further understanding of how gene expression regulates cellular mechanics within the context of genes, proteins, and networks will improve our knowledge of cancer biology. Towards this end, RNAi can be used to knockdown mechanics-relevant genes through modified mRNA levels and microRNA can be used to induce mesenchymal to epithelial transition (MET) in ovarian cell lines to evaluate the effect of gene expression and morphology on cell mechanics and metastasis.

Our studies on pancreatic cancer cell line AsPC-1 have demonstrated MET upon treatment with N-acetyl-L-cysteine (NAC), as described in chapter 2. EMT is a promoting factor in cancer metastasis during which tumor cells change their morphology, undergo cytoskeletal reorganization, and acquire a motile phenotype to be able to migrate and invade within the surrounding microenvironment [4-9]. Previous studies have shown the accompanying reduction of *in vitro* migratory and invasive activities when cells

168

change from mesenchymal to epithelial-like morphology upon alterations in gene expression [10, 11] in cancer cells. Cytoskeletal structure, as modulated by in gene expression at the molecular level, is implicated in cellular morphology, single cell stiffness and cancer metastasis. Having demonstrated the correlation between cell stiffness and metastatic potential in ovarian cancer, and revealed the role of actin cytoskeleton remodeling in change of stiffness and metastasis, it is desirable to investigate the potential correlation between morphology and stiffness in single cells in greater detail, and to understand how these properties and cytoskeletal structure are regulated by the gene expression profile. To this end, cell morphology can be altered using microRNA transfection and cell stiffness will be subsequently measured.

Future experiments can be conducted to modify the expression of relevant genes as described in chapter 1 to observe their effects on cell mechanics and *in vitro* migration/invasion properties. In addition, miRNA transfection will also be utilized to alter gene expression profiles and morphologies of healthy and cancerous ovarian cells, subsequent stiffness measurements will be conducted using AFM.

6.2.2 *Single gene knockdown of cytoskeletal proteins in HEY A8 cells to determine their impact on cellular mechanics, migration, and invasion.*

The contributions of individual proteins to cell mechanics will be measured by knocking down their expression in HEY A8 cells using siRNA and subsequent measurement of stiffness with AFM and *in vitro* migration/invasion assays. Particular genes implicated in previous studies include cofilin-2 (CFL2), twinfilin (TWF1), myosin light chain kinase, as well as regulatory and catalytic subunit genes of cAMP-dependent protein kinase. The

gene expression of these proteins at mRNA level as analyzed by microarray and qPCR in chapter 2 were summarized in Table 6.1.

Table 6.1: Overexpression of relevant genes in HEY A8 relative to HEY

Gene name	Overexpression level in HEY A8 relative to HEY	
	Microarray	*qPCR*
CFL2	1.8876	--
TWF1	1.7949	2.63
PFN1	1.53698	--
PRKAA2	2.1914	3.98

6.2.3 microRNA transfection to induce mesenchymal to epithelial transition in IOSE, HEY and HEY A8 cells to determine their impact on cellular mechanics, migration, and invasion.

MiRNAs are powerful regulators of cellular process and we will determine whether miRNA regulation of mesenchymal to epithelial transition in metastatic ovarian cancer cells will be utilized to modify cellular mechanics more efficiently than individual gene knockdown. miRNA will be used to induce mesenchymal to epithelial transition (MET) in IOSE, HEY and HEY A8 cells; gene expression profiles will be monitored by microarray; migration/invasion assay *in vitro* and single cell stiffness measurement with AFM will be conducted, the efficacy of miRNA transfection will be evaluated by comparing the results of cells from control and transfected groups from each cell type.

6.3   Expected research outcomes

6.3.1   *Single gene knockdown*

Following the methodology of atomic force microscopy (AFM) mechanical measurements on single ovarian epithelial cells as described in chapter 2, stiffness and *in*

vitro migration/invasion activities will be measured for negative control and knockdown group. The experimental setup and expected outcome is shown in Figure 6.1, knockdown of these mechanical relevant genes are expected to elevate stiffness and reduce metastatic potential.
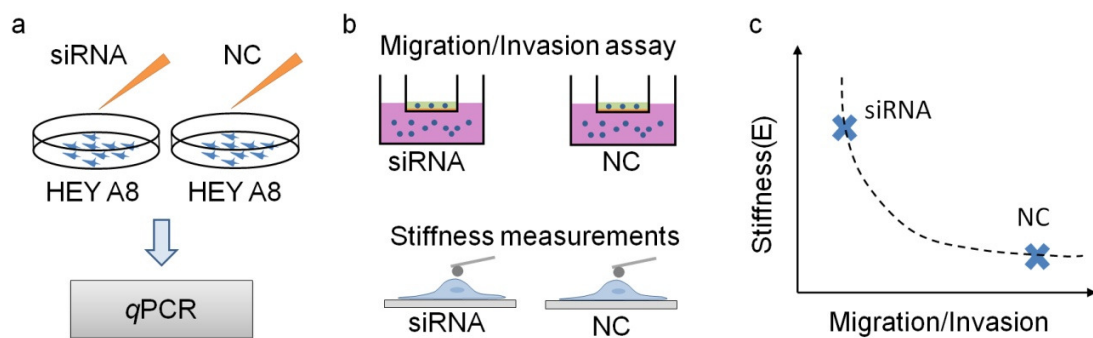
Figure 6.1: Experimental sketch of single gene knockdown, migration/invasion assay, and stiffness measurements. a) gene knockdown followed by *q*PCR, NC-negative control; b) migration/invasion assay and stiffness measurements with AFM, and c) expected result: gene knockdown increases stiffness and reduces *in vitro* migration/invasion activities.

6.3.2 *Mesenchymal to epithelial transition in IOSE, HEY and HEY A8 cells and their impact on cellular mechanics, migration, and invasion*

AFM and migration/invasion assays can also be conducted on single cells after microRNA transfection, in which cells are expected to undergo MET, alter gene expression profiles, increase stiffness and reduce invasiveness. The experimental method with expected outcomes are sketched in Figure 6.2.
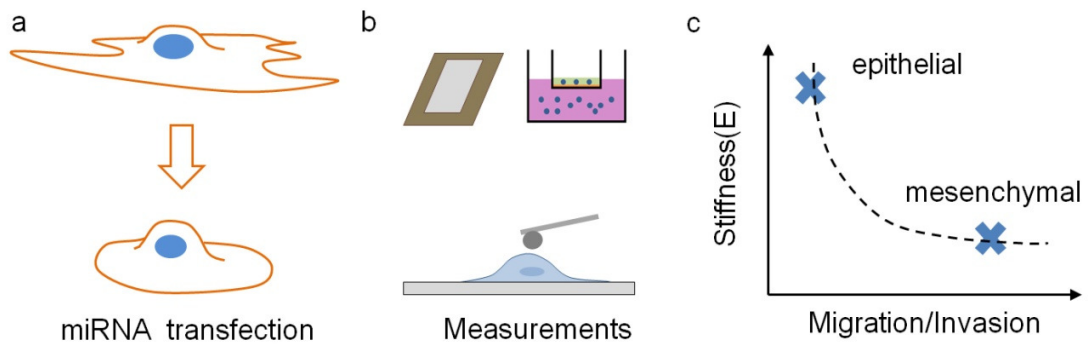
Figure 6.2: Experimental sketch of miRNA transfection on IOSE, HEY and HEY A8 cells, a) miRNA transfection induces MET, b) subsequent gene expression profile analysis with microarray, migration/invasion assay, and stiffness measurement, and c) expected results: MET induce increase in stiffness and reduction in migration/invasion activities.

6.4   Significance of the future research

Successful completion of the future research projects will lead to a better understanding of the impacts of genes and networks on biomechanical properties of ovarian cancer, further motivating the testing of cancer cells derived from patients, and identifying potential new biomarkers for diseased cells and targets for therapeutics which can impede the spread of cancer cells.

6.5   References

1.   Dudani, J.S., et al., *Pinched-flow hydrodynamic stretching of single-cells.* Lab on a Chip, 2013. **13**(18): p. 3728-3734.

2.   Sollier, E., et al., *Size-Selective Collection of Circulating Tumor Cells using Vortex Technology.* Lab on a Chip, 2013.

3.   Gossett, D.R., et al., *Hydrodynamic stretching of single cells for large population mechanical phenotyping.* Proceedings of the National Academy of Sciences, 2012.

4.   Vergara, D., et al., *Epithelial–mesenchymal transition in ovarian cancer.* Cancer Letters, 2010. **291**(1): p. 59-66.

5.   Yilmaz, M. and G. Christofori, *EMT, the cytoskeleton, and cancer cell invasion.* Cancer and Metastasis Reviews, 2009. **28**(1-2): p. 15-33.

6.   Zavadil, J., et al., *Epithelial-Mesenchymal Transition.* Cancer Research, 2008. **68**(23): p. 9574-9577.

7.   Guarino, M., *Epithelial–mesenchymal transition and tumour invasion.* The International Journal of Biochemistry & Cell Biology, 2007. **39**(12): p. 2153-2160.

8.   Iwatsuki, M., et al., *Epithelial–mesenchymal transition in cancer development and its clinical significance.* Cancer Science, 2010. **101**(2): p. 293-299.

9.   Thiery, J.P., et al., *Epithelial-Mesenchymal Transitions in Development and Disease.* Cell, 2009. **139**(5): p. 871-890.

10.   Chen, J., et al., *Overexpression of miR-429 induces mesenchymal-to-epithelial transition (MET) in metastatic ovarian cancer cells.* Gynecologic Oncology, 2011. **121**(1): p. 200-205.

11.   Bao, X.-l., et al., *Wnt3a promotes epithelial-mesenchymal transition, migration, and proliferation of lens epithelial cells.* Molecular Vision, 2012. **18**: p. 1983-1990.